THE UNIVERSITY
of ADELAIDE

Cloudy Ammonia: A multi-wavelength molecular line survey of the molecular clouds surrounding the W28 supernova remnant.

Brent Nicholas
B.Sc (Hons), Physics

Submitted in total fulfilment of the requirements
of the degree of Doctor of Philosophy

July 7, 2011

School of Chemistry & Physics
The University of Adelaide

Contents

List of Figures

List of Tables

Abstract

This thesis is a multi-wavelength study of high energy objects interacting with the interstellar medium (ISM). One such object is the W28 supernova remnant (SNR) with several sites of TeV (10^{12} eV) γ-ray emission detected from its boundary by the H.E.S.S. telescopes. The γ-ray emission is spatially well matched to giant molecular clouds which surround the remnant. In order to understand the distribution of dense ($n > 10^3\,\mathrm{cm}^{-3}$) molecular gas in the region, multi-wavelength ($\lambda \sim$12 mm and 7 mm) molecular line surveys are presented. Utilising the NH_3, CS and SiO molecules, the broad-scale distribution of the dense and disrupted gas in the W28 region is revealed. Additional multi-wavelength data towards W28, including radio ($\lambda \sim$ cm), molecular line ($\lambda \sim$ mm), infra-red ($\lambda \sim 10^{-6}$ m), X-ray ($\lambda \sim 10^{-10}$ m) and γ-ray ($\lambda \sim 10^{-12}$ m) data, are compared and discussed in context with the results of this work. Other high energy ISM interacting objects, microquasars, are also studied. TeV γ-ray observations towards three candidate microquasars with jets and/or jet/ISM interactions are presented. In all three cases, no significant point-like or extended TeV γ-ray emission is seen and upper-limits are set.

Declaration of Originality

I, Brent Nicholas certify that this work contains no material which has been accepted for the award of any other degree or diploma in any university or other tertiary institution and, to the best of my knowledge and belief, contains no material previously published or written by another person, except where due reference has been made in the text. I give consent to this copy of my thesis when deposited in the University Library, being made available for loan and photocopying, subject to the provisions of the Copyright Act 1968. The author acknowledges that copyright of published works contained within this thesis (as listed below*) resides with the copyright holder(s) of those works. I also give permission for the digital version of my thesis to be made available on the web, via the University's digital research repository, the Library catalogue and also through web search engines, unless permission has been granted by the University to restrict access for a period of time.

*Published works contained within this thesis:

Nicholas B., & Rowell G., 2008, American Institute of Physics (AIP) Conf. Proc., 1085, 245.

Nicholas B., Rowell G., Burton M.G., Walsh A., Fukui Y., Kawamura A., Longmore S. & Keto E., 2011, Monthly Notices of the Royal Astronomical Society (MNRAS), 411, 1367 (+ online appendices).

Nicholas B.P., Rowell G., Burton M.G., Walsh A.J., Fukui Y., Kawamura A. & Maxted N.I., 2011, Monthly Notices of the Royal Astronomical Society (MNRAS), *Accepted for publication. (24/08/2011).*

Nicholas B.P., Rowell G., Burton M.G., Walsh A.J., Fukui Y., Kawamura A. & Maxted N.I., *Manuscript in preparation.*

BRENT NICHOLAS July 7, 2011

Acknowlegdements

I would like to thank my principle supervisor, Gavin Rowell, for all his help and guidance over the past three and a half years. His advice and support at all stages of my PhD has been greatly appreciated. I am very appreciative of the funding Gavin secured, which enabled me to travel to conferences and workshops, both interstate and internationally, on multiple occasions. I thank my co-supervisor, Roger Clay, who provided a keen eye when proof reading this work. His ability to find time in his busy schedule and to provide extremely prompt feedback and advice when requested was a real asset, especially in the late stages of my thesis write-up. I extend my gratitude to my two un-official co-supervisors, Michael Burton (University of New South Wales) and Andrew Walsh (James Cook University), for providing help and support with the millimetre side of this project. Their vast knowledge and experience helped provide a smooth transition from γ-ray astronomy to radio and millimetre wave astronomy. Without their continued support, my research and progress would have definitely been slow-moving. I am indebted to Clive Moore and Chris Jordan who offered to proof read this work. Your fresh sets of eyes picked up corrections I overlooked and helped to improve this thesis.

I would also like to thank the post graduate students from the Adelaide University Astrophysics Group, both past and present, who helped keep my PhD experience positive and provided many interesting lunch-time conversations. I further extend my thanks to my office mate, Nigel Maxted, who provided many relevant discussions which kept my research moving forward. I acknowledge the support of the University of Adelaide and the School of Chemistry and Physics for the financial assistance of a Divisional Scholarship, and for extending its length beyond the initial three years.

Finally, my gratitude goes to my families and friends. I especially thank Charles and Nera Cox for looking after me and providing me with many lunch-packs, which fuelled my daily research. I thank my parents, Jayne and Lynton Nicholas, for all their support during my extended stay in the student lifestyle and Granny Dawn, who made ***sure*** this thesis was completed. Last, but certainly not least, I extend my love and gratitude to Ann-Marie Cox, who continually loves, supports, and makes me happy.

Preface

Motivation

Two of the biggest unsolved questions facing modern high energy astronomers are, "What is the origin of cosmic rays?" and "How are they accelerated to such high energies?" These questions have remained unanswered for over a century, and finding the solutions to these age-old cosmic-ray (CR) problems were major driving forces behind the field of gamma-ray (γ-ray) astronomy. Very high energy (VHE) γ-rays ($E_\gamma > 100\,\mathrm{GeV}$, $1\,\mathrm{GeV}{=}10^9\,\mathrm{eV}$, $1\,\mathrm{eV} = 1.6{\times}10^{-19}\,\mathrm{J}$) are only produced in the most violent and extreme processes within the universe. With the exception of radioactive decay, VHE γ-rays are produced via interactions of accelerated charged particles, either hadrons (protons, α-particles, nuclei) or leptons (electrons, positrons). In the hadronic framework, γ-rays are the by-products of interactions between high energy hadrons, the so called cosmic-rays, while the leptonic framework is centred on the interactions of high energy electrons in photon and magnetic fields. Unfortunately, this also means that, until astronomers can determine the origin of the γ-rays, the origin of the multi-TeV ($1\,\mathrm{TeV} = 10^{12}\,\mathrm{eV}$) CRs will remain a mystery.

Along the Galactic plane, towards the Galactic centre, lies the W28 supernova remnant (SNR). The H.E.S.S. telescopes have detected several TeV γ-ray sources surrounding the remnant. These γ-ray sources spatially overlap with giant molecular clouds. W28 provides a unique laboratory to study both dense molecular gas and γ-ray emission. Studies of the gas and material toward sites of γ-ray emission are helpful in determining the origin of the γ-ray emission and can also provide information on the high energy particles which spawned them. Dense molecular gas provides a large target for CRs to interact with, which in turn, produce γ-rays in a hadronic manner. Not only does dense molecular gas provide evidence supporting a hadronic origin, it can also provide evidence against a leptonic origin. This makes studies of dense gas towards sites of γ-ray emission a powerful probe into the origin of the γ-rays and also provides information on the CRs in the region.

Within our Galaxy, the microquasar class of objects are candidate sources of TeV γ-ray emission. Relativistic 'jets', which manifest from the accretion powered system, are capable of accelerating particles to very high energies. Therefore, these VHE particle flows interacting with the interstellar medium (ISM) could provide another source of Galactic γ-ray emission, and another site of multi-TeV CR acceleration.

With these ideas in mind, this thesis is structured around a core theme of high energy objects, the W28 supernova remnant and several microquasars, which are interacting with the ISM.

Structure of this Thesis

This thesis is a multi-wavelength study of high energy objects interacting with the ISM. It tackles these issues from both the low energy end of the spectrum, by studying the dense molecular gas towards the W28 SNR, and the high energy end of the spectrum, with TeV γ-ray observations towards multiple ISM interacting microquasars.

Chapter 1 introduces the ISM, cosmic rays and the ideas of γ-ray astronomy in broad terms. Chapter 2 discusses the underlying physics of radiative transfer and discusses how molecular line observations are used to study dense gas. The ammonia molecule, which has been proven to be an exceptionally useful probe into the dense ISM, is discussed in detail. Chapter 3 introduces the Mopra millimetre wave telescope and presents the results of a 12 mm molecular line survey of the molecular clouds towards the W28 supernova remnant. Chapter 4 presents the results of a 7 mm molecular line survey of the molecular clouds towards the W28 supernova remnant. Chapter 5 presents the results of deep NH_3 observations of the disrupted molecular clouds towards W28. Chapter 6 discusses the underlying physics of ground based γ-ray astronomy, including the imaging atmospheric Cherenkov technique and the H.E.S.S. telescopes. The microquasar class of objects is also introduced and the results of γ-ray observations towards three microquasars interacting with the ISM are presented. Chapter 7 is a final summary of the work presented throughout this thesis and a brief outlook for future developments.

Public Displays of Results

The results of this thesis are submitted by publication. The work presented for this thesis, in various stages, has been presented at conferences and workshops around the world. Here I summarise the contributions of conference posters, conference proceed-

ings and published works of which I have been a part.

- **Poster Submission:**
  H.E.S.S. Observations of the Microquasars Cir X−1, Cyg X−1 and 4U 1755−33, 2008, 4th Heidelberg International Symposium on High Energy Gamma-Ray Astronomy, Heidelberg, Germany.
  `http://www.mpi-hd.mpg.de/hd2008/pages/news.php`

- **Conference Proc:**
  H.E.S.S observations of the Microquasars Cir X−1, Cyg X−1 and 4U 1755−33, Nicholas B., & Rowell G., 2008, American Institute of Physics (AIP) Conf. Proc., 1085, 245.

- **Poster Submission:**
  Mopra NH_3 observations towards the TeV Supernova Remnant W28, 2009, International Winter School on the Interstellar Medium, Ise-Shima, Mie, Japan.
  `http://www.a.phys.nagoya-u.ac.jp/WS09/`

- **Poster Submission:**
  Mopra Studies of the dense gas towards W28 and RX J1713.7−3946, 2009, Astronomical Society of Australia - Annual Scientific Meeting, University of Melbourne, Melbourne, Australia.
  `http://asa2009.science.unimelb.edu.au/Site/Home_Page.html`

- **Poster Submission:**
  Mopra ammonia studies of the dense gas towards the supernova remnant W28, 2010, International Winter School on the Interstellar Medium, Ise-Shima, Mie, Japan.
  `http://www.a.phys.nagoya-u.ac.jp/WS10/`

- **Conference Presentation:**
  Deep Mopra studies of the dense and disrupted molecular gas associated with the TeV gamma-ray sources in the supernova remnant W28 field, 2010, Astronomical Society of Australia - Annual Scientific Meeting, University of Tasmania, Hobart, Australia.
  `http://www-ra.phys.utas.edu.au/ASA2010/`

- **Poster Submission:**
  Studies of the dense and disrupted gas towards the TeV gamma-ray supernova remnant W28, 2010, Great Barriers in High Mass Star Formation, Townsville, Australia.
  `http://www.jcu.edu.au/hmsf10/`

- **Refereed Journal Article:**
  12 mm line survey of the dense molecular gas towards the W28 field TeV gamma-ray sources, Nicholas B., Rowell G., Burton M.G., Walsh A., Fukui Y., Kawamura A., Longmore S. & Keto E., 2011, Monthly Notices of the Royal Astronomical Society (MNRAS), 411, 1367 (+ online appendices).

- **Refereed Journal Article:**
  A 7 mm line survey of the shocked and disrupted molecular gas towards the W28 field TeV gamma-ray sources, Nicholas B.P., Rowell G., Burton M.G., Walsh A.J., Fukui Y., Kawamura A. & Maxted N.I., 2011, Monthly Notices of the Royal Astronomical Society (MNRAS), *Accepted for publication. (24/08/2011).*

- **Poster Submission:**
  Deep NH_3 observations of the W28 supernova remnant TeV source HESS J1801−233, 2011, Astronomical Society of Australia - Annual Scientific Meeting, University of Adelaide, Adelaide, Australia.
  `http://www.physics.adelaide.edu.au/astrophysics/asa2011/`

- **Manuscript in Preparation.:**
  Deep NH_3 survey of the disrupted molecular cloud towards the W28 TeV gamma-ray source HESS J1801−233, Nicholas B.P., Rowell G., Burton M.G., Walsh A.J., Fukui Y., Kawamura A. & Maxted N.I., *Manuscript in preparation.*

CHAPTER I

Introduction

1.1 Introduction

Our understanding of the universe comes largely from our observations of electromagnetic (EM) radiation. The most obvious form of EM radiation offered by the universe is, of course, visible starlight which can be seen without fancy equipment. A simple telescope or even a pair of binoculars will allow you to admire the brightest stars in our night sky. Alone, this visible radiation provides information on the thousands of stars visible on a clear night. However, starlight is a mere fraction of the total EM radiation that the universe offers, from low frequency/energy radio waves to very high frequency/energy γ-rays.

It is vital to observe the universe at many frequencies, as a different frequency can tell a different story. Therefore, modern-day astronomers are observing all frequencies at which the universe broadcasts to understand further the nature of the stars, galaxies and the universe itself. Due to the Earth's protective atmosphere only small 'bands' of EM radiation, radio waves and visible light, reach the surface. To observe the EM radiation outside these atmospherically 'allowed' bands, sophisticated detection methods and equipment are required. These range from satellites, such as, *Sptizer, XMM-Newton, Fermi*, to large-area ground telescope arrays, such as, *H.E.S.S., VERITAS* and *MAGIC*. Pictured in Figure 1.1 is a cartoon illustrating the different levels of atmospheric penetration for photons of different wavelengths.

Much of the detected EM radiation is generated thermally. The hotter the object, the more energetic the radiation it emits. Gamma-rays at the highest energies are interesting because they provide a tool for observing the most extreme and violent processes that take place within the universe. No physical object can be hot enough to produce γ-rays at the highest energies. Therefore, these very high energy (VHE) γ-rays are produced in 'non-thermal' conditions. Such conditions occur after a star explodes, so called supernova remnants (SNR), through fast flowing winds of particles creating intense shocks or in regions of intense magnetic fields, which can only be created by neutron stars or black holes. Thus, observing in VHE γ-rays provides a unique view

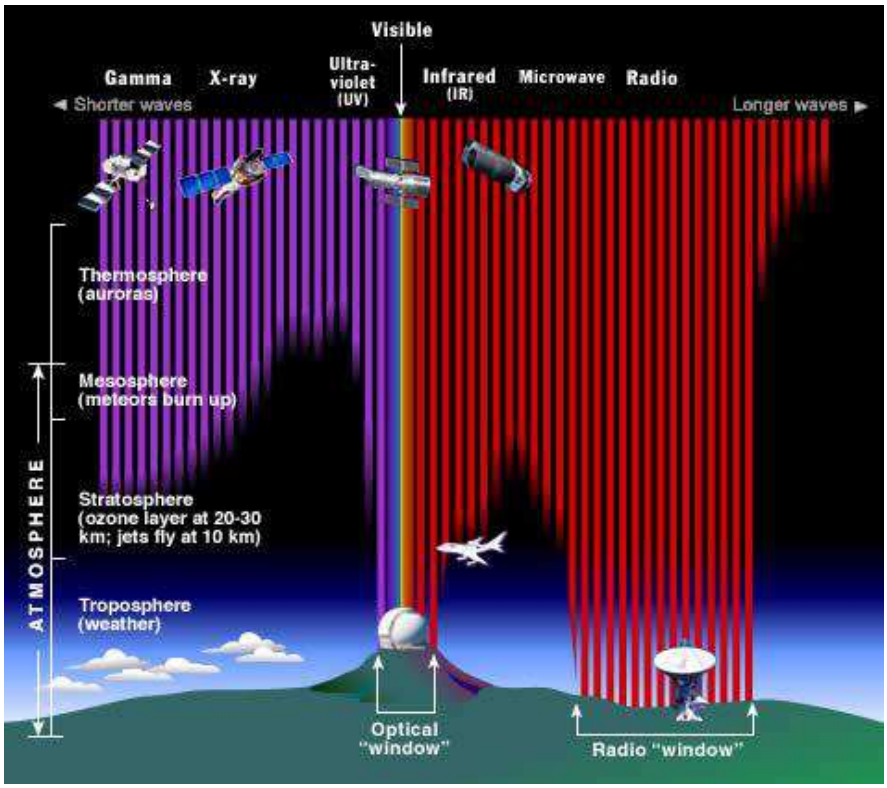

Figure 1.1: Cartoon depicting the transparency of the Earth's atmosphere as a function of energy/wavelength. The only two 'windows' where radiation is allowed to reach the surface are the optical window and the radio window. Image credit: Space Telescope and Science Institute, STCI/JHU/NASA.

of the non-thermal universe.

Only through multi-wavelength observations can a complete understanding of the universe be reached. For example, the Crab Nebula, which is a common standard source for many astrophysical observations, looks quite different depending on the observational frequency band. Illustrated in Figure 1.2 is a multi-panel view of the Crab Nebula in four different wave bands, radio, infrared, optical and X-ray. Alone, each band provides information about the object and its environment, but together they provide a far greater understanding of the complex environment of the source. This approach has also been applied to the Galactic plane. Displayed in Figure 1.3 is the Galactic plane in 10 different wavebands, ranging from the low energy radio continuum to the high energy γ-rays.

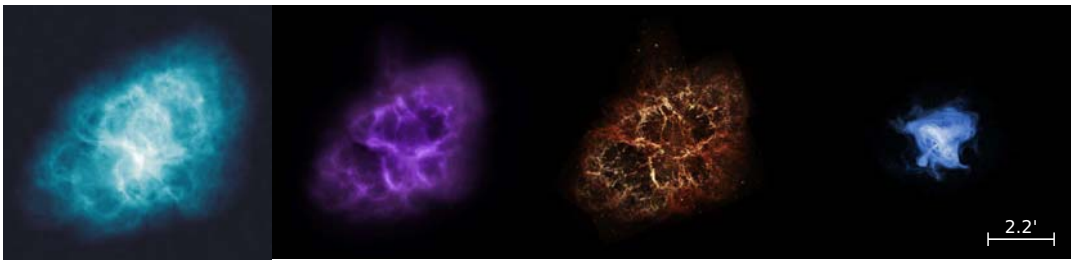

Figure 1.2: Images of the Crab Nebula in multiple wavelengths. From left to right: radio, infra red, optical and X-ray. (Image Credits: Radio: NRAO/AUI/M. Bietenholz; Infrared: NASA/JPL-Caltech/Univ. Minn./R. Gehrz; Optical: NASA/ESA/ASU/J. Hester & A. Loll; X-ray: NASA/CXC/SAO/F. Seward.)

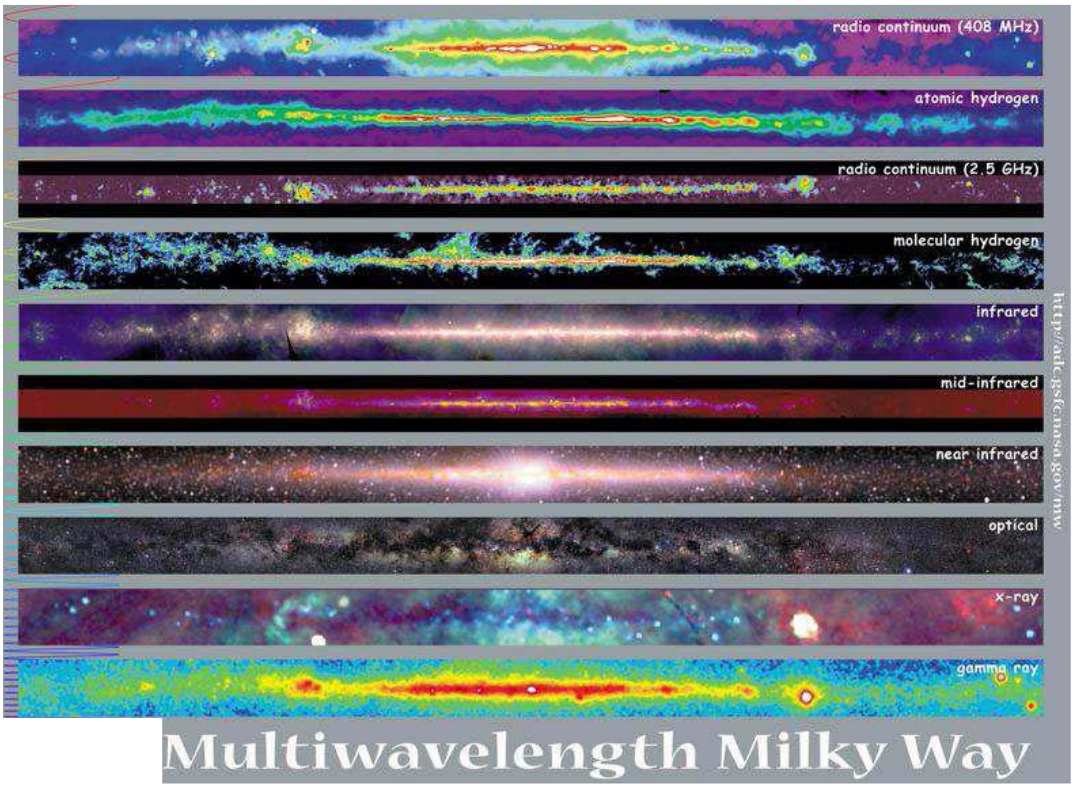

Figure 1.3: Images of the Galactic centre in many wavelengths. From top to bottom the images are: **Radio Continuum (408 MHz):** which traces electron populations moving through magnetic fields, **Atomic Hydrogen:** which traces the diffuse atomic gas, **Radio Continuum (2.4-2.7 GHz):** which traces hot ionised gas and/or electrons moving through magnetic fields, **Molecular Hydrogen:** which traces the distribution of molecular gas, **Composite Infrared (12, 60, 120 μm):** which traces dust heated by stars, **Mid-Infrared (6.8-10.8 μm):** which is believed to trace complex polycyclic aromatic hydrocarbons (PAH), **Composite Near-Infrared (1.25, 2.2, 3.5 μm):** which traces 'cool' stars, **Optical:** which traces the visible light and shows the molecular gas (black clouds) obscuring the light, **Composite X-Ray (0.25, 0.75, 1.5 keV):** which traces the hot shocked gas, **γ-rays (300 GeV):** which traces regions of cosmic-rays interacting with molecular clouds. Image credit NASA: Multi-wavelength Milky Way.

	Size (pc)	Temperature (K)	Mass ($M_\odot$)	Density (cm^{-3})
Complex	50	10-15	10^5	100-300
Cloud	3-20	15-40	10^3-10^4	10^3-10^4
Clump	0.5-3	30-90	10-10^3	10^4-10^6
Core	< 0.5	30-200	10^3-10^6	$> 10^6$
Hot Core	0.1-0.5	90-300	10^2	$> 10^7$
UC-HII Region	< 0.1	10^4	–	$> 10^4$

Table 1.1: Typical physical parameters associated with giant molecular clouds, GMCs, in the ISM. Table assembled from Cernicharo (1991); Garay & Lizano (1999); Ceccarelli *et al.* (2000); Kurtz *et al.* (2000) and Fuente *et al.* (2005).

1.2 The Interstellar Medium

The interstellar medium (ISM) is the diffuse material, with average density $n \sim 1\,\mathrm{cm}^{-3}$, which pervades the Galaxy between the star systems. It primarily consists of gas and dust, but also contains plasma, cosmic rays, magnetic fields and radiation fields. By mass it consists of 1% dust and 99% gas, of which 90% is hydrogen, 9% helium and 1% is heavier elements. The ISM is both the start and end points of the stellar evolutionary cycle. It provides the matter from which the stars are formed. It is replenished with the matter and energy from planetary nebulae, stellar winds and supernovae.

Molecular clouds (MC) are a subset of the ISM. These are the cold, dense regions of gas and dust, exclusively from which stars are born. Molecular clouds with mass $> 10^4\,\mathrm{M}_\odot$ ($1\,\mathrm{M}_\odot = 1.988\times10^{30}\,\mathrm{kg}$) are called giant molecular clouds (GMC) and can be several tens of parsecs ($1\,\mathrm{pc} = 3.09 \times 10^{16}\,\mathrm{m}$) across. These GMCs, and MCs in general, have complex substructures that contain filaments, bubbles, clumps and cores. Presented in Table 1.1 are some general physical scales associated with MCs in the ISM. It is from within these substructures that stars will form.

1.3 The Process of Forming Stars

Stars are the most recognisable astrophysical objects that exist throughout the universe, and are responsible for the syntheses of the heavy elements which our lives are built around. The age, distribution and composition of the stars contain information reflecting the history and evolution of their host galaxy. In fact, it is the stars themselves that drive the future structure and evolution of galaxies. Stars are constantly evolving and in each evolutionary phase, are contributing differently to their surrounding environments. Therefore, studying the birth, life and death of stars is vital to the

field of astronomy and astrophysics.

Stars can be initially split into two broad categories depending on their mass - low mass stars ($< 8\,M_\odot$) and high mass stars ($> 8\,M_\odot$). The theory of star formation and evolution is dependent on mass. While our understanding of low mass star formation processes is well established, the early stages of high mass star formation and evolution remain elusive. The reason for this is that the physical properties of high mass star forming regions impede progress.

Typically, high mass stars are distant and deeply embedded in their parent molecular cloud, obscuring them from view during their early evolutionary phases. Additionally, they are rare and evolve rapidly, which makes their early evolutionary phases short-lived. Finally, high mass stars are seldom formed in isolation, they preferentially form in clusters. The close proximity of other high mass stars and their associated interacting: gravitational fields, radiation fields, stellar winds and outflows on the surrounding environment greatly complicate the picture.

In order to produce a star, gravity must overcome the effects of, magnetic fields, thermal pressure, angular momentum, turbulence and radiation. These properties all act to support the molecular cloud. All stars, both high and low mass, are formed from the molecular gas and dust contained in the in-homogeneous and turbulent molecular clouds that populate the ISM. Turbulence within the cloud mixes the gas, producing knots of dense gas with sufficient mass that they collapse under their own weight.

To form a low mass star, a collapsing cloud increases in density causing the ionisation fraction[1] to decrease. The charged particles are too few in number to maintain the magnetic field, which is subsequently released from the core. This causes an inside out collapse, where the centre of the core collapses rapidly to form a protostar. Conservation of angular momentum requires the collapsing system to increase its rotational speed, which causes the in-falling material to be flattened out into a disk. Material accretes onto the protostar and bipolar outflows and/or collimated jets form perpendicular to the accretion disk. At high densities ($n > 10^{10}\,\mathrm{cm}^{-3}$) the system becomes optically thick and radiation is no longer able to escape. This causes the system to heat up to $\sim 4000\,\mathrm{K}$ which destroys the dust grains, and starts to dissociate molecular hydrogen. This dissociation process absorbs most of the energy and slows down the rapid temperature increase. Once a large fraction of the molecular hydrogen is dissociated, the temperature starts to increase rapidly again.

Eventually, the temperature and density are high enough to ignite fusion within the core. Very quickly the star obtains hydrostatic equilibrium, where the outward radiation pressure balances the inward gravitational pressure, preventing further col-

[1] The ionisation fraction is a measure of the number of electrons in the cloud.

lapse. At this stage, the star begins its life on the main sequence. From here, low mass stars have a relatively uneventful evolution. However, once the hydrogen in the core is exhausted, the core collapses and increases its temperature, causing the outer layers to expand. Hydrogen still exists in the outer layers of the star so fusion continues in the expanded shell surrounding the hot compact core. The expanded shell-burning star has evolved into a red giant. Eventually the outer layers will be unable to continue fusion and all that remains is the hot compact core, a white dwarf.

The process of high mass star formation is not as simple as scaling up the low mass case by starting with a larger cloud. Problems start to arise when the central protostellar core has mass $\geq$10 $M_\odot$. At this stage, the luminosity and radiation pressure of the protostar are substantial and can halt (or possibly even reverse) the in-fall motions, effectively creating an upper limit to the protostellar mass. Several theories have been suggested to explain the early stages of high mass star formation: the monolithic collapse (McKee & Tan, 2003), competitive accretion (Zinnecker, 1982) and stellar mergers (Bonnell *et al.*, 1998), yet it appears that no one scenario will apply to all cases.

Regardless of the process, high mass stars are able to gain mass effectively once fusion has initiated. The fusion process produces excess energy and causes the accretion disk to become ionised. Once the ionisation of the disk has occurred, the system has entered the HII phase as a hyper-compact HII region. Eventually, the star will terminate its mass gain and obtain its final mass. By this time, there is insufficient remaining material around the star to contain the ionising radiation. The stellar radiation freely expands into the surrounding environment to fill a sphere with Strömgren radius (Strömgren, 1939). The stellar radiation mixes with that of other nearby high mass stars. By this stage, the group of high mass stars has evolved into an ultra-compact HII region. The mixing stellar winds continue to expand and the group of high mass stars will eventually evolve into a compact HII radio region. Finally the region evolves into a diffuse optical HII region, like the Orion Nebula pictured in Figure 1.4.

Just like stellar formation, stellar evolution and death are tied to the mass of the star. High mass stars have more exotic and eventful evolutions and deaths. High mass stars have a much stronger gravitational pressure for fusion to support. This increased gravitational pressure continually collapses and heats the core of the star, allowing the fusion of much heavier elements. This process continues until the star contains an iron core which cannot fuse further. The sudden halt in fusion allows gravity to rapidly condense the iron core within few seconds. If the iron core has a mass $1.4 < M < 3\,M_\odot$, it will collapse into a neutron star. Otherwise, cores $> 3\,M_\odot$ will completely collapse

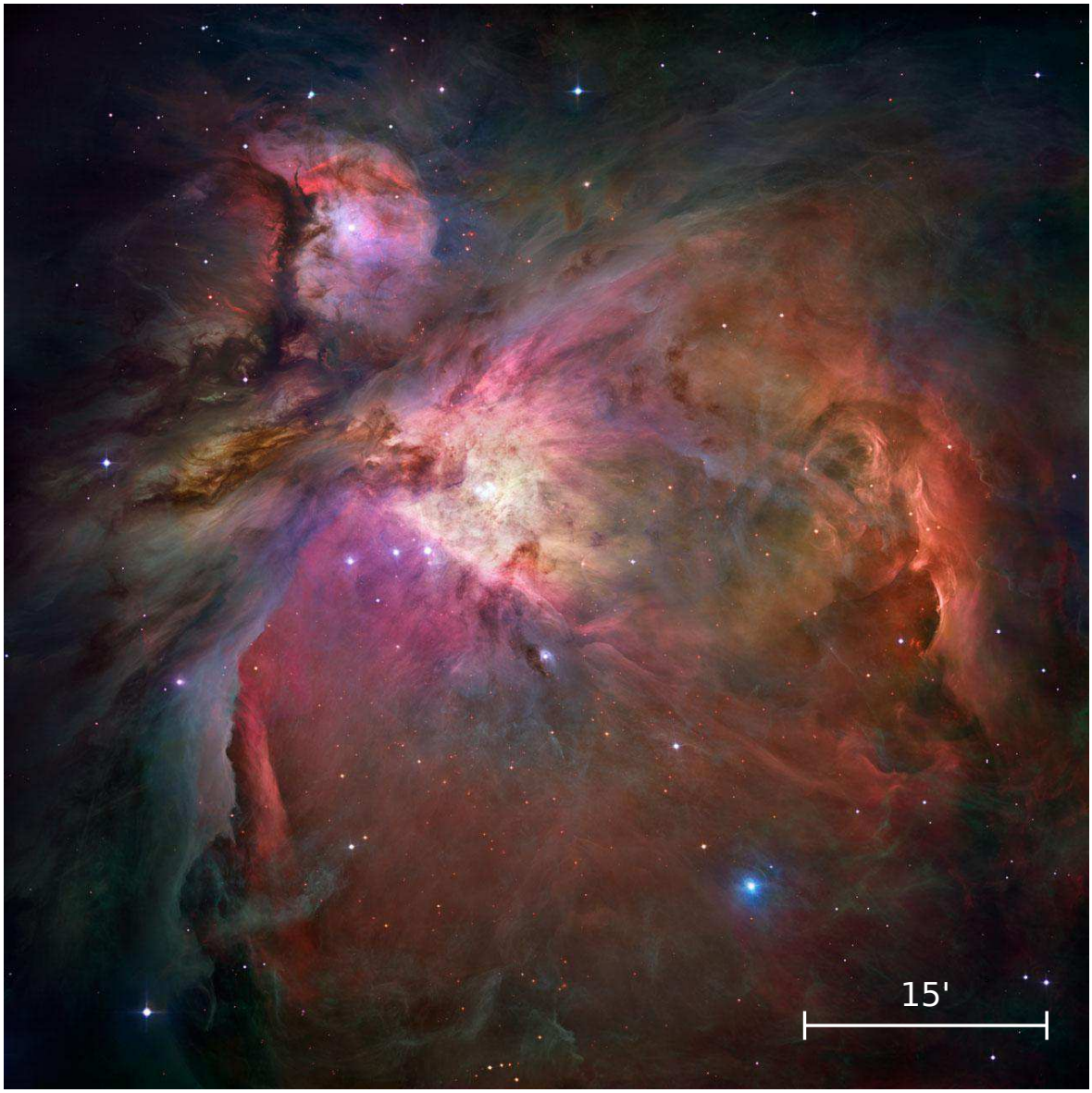

Figure 1.4: Hubble Space Telescope optical image of the Orion Nebula, the closest high mass star forming region. The nebula's glowing gas surrounds hot young stars at the edge of a GMC. The Orion Nebula provides a unique view of the stages of stellar evolution as the high mass stars have blown away portions of the paternal cloud. This image reveals about 3000 stars within the nebula which is approximately 4 pc across. As is later discussed in § 1.8, sites of high mass stellar evolution are sources of γ-rays and, indeed, soft γ-rays have been detected towards the Orion Nebula (Bloemen *et al.*, 1994). Image credit NASA, ESA, M. Robberto (STScI/ESA) and The Hubble Space Telescope Orion Treasury Project Team.

into a black hole. This catastrophic core collapse results in the outer layers of the star being violently expelled and releases vast amounts of energy. The material that is expelled in the supernova explosion is recycled back into the ISM and will eventually provide the basis for the next generation of stars and planetary systems. Figure 1.5 portrays a schematic of the evolution of a group of high mass stars, from birth in a GMC to death in a SNR.

1.4 Cosmic Rays

Ever since 1912 when Victor Hess took his electroscope up in a balloon (pictured in Figure 1.6) and found that the level of background radiation on Earth was increasing with altitude, astronomers have been puzzled by the concepts of cosmic rays (CR). Previously, scientists had assumed that the ambient background radiation was originating from the radioactive elements in the Earth, and that this radiation would dissipate with altitude. This effect was observed at low altitudes, however, at higher altitudes the radiation levels increased considerably. Victor Hess concluded that "a radiation of very high penetrating power enters our atmosphere from above" (Hess, 1912).

It is now known that cosmic ray particles hit the Earth's atmosphere at a rate of 1000 per square meter per second at low energies, up to 1 per square kilometre per century at the highest energies. They are ionised nuclei and are made up of approximately 90% protons, 9% alpha particles and 1% electrons and heavy nuclei, and they are distinguished by their high energies. Cosmic rays are relativistic, having energies at least comparable to or somewhat greater than their rest-masses. A very few of them have ultra-relativistic energies extending up to 10^{20} eV, eleven orders of magnitude greater than the equivalent rest mass energy of a proton.

The local CR spectrum observed at Earth is shown in Figure 1.7. This is a remarkable spectrum, as it is a near single power law, $E^{-2.7}$, over more than 10 orders of magnitude, up to energies of a few 10^{20} eV. There are two features, the CR 'knee' at 10^{15} eV, where the spectrum slightly steepens to an E^{-3} power law, and the CR 'ankle' at 10^{18} eV, where the spectrum slightly flattens off again. The generally accepted belief is that CRs up to the knee, energies of a few PeV (10^{15} eV), are of Galactic origin, and those with higher energy are from outside our Galaxy. The fundamental questions of cosmic ray physics are, "Where do they come from?" and in particular, "How are they accelerated to such high energies?"

A major problem of CR astrophysics, is that CR arrival directions are isotropic in the sky and contain little or no directionality. As CRs are charged particles, they are deflected by interstellar magnetic fields, so their arrival directions at Earth are

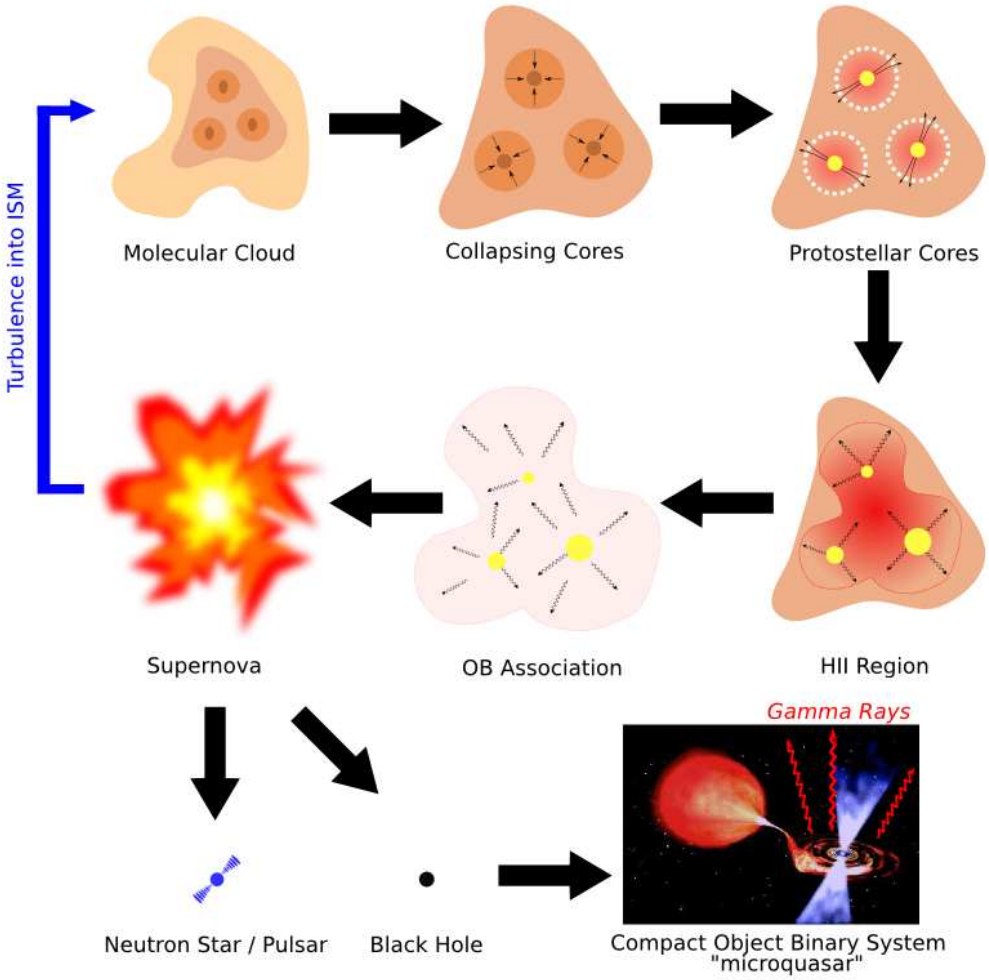

Figure 1.5: A schematic of the evolutionary sequence for high mass stars. In a turbulent and in-homogeneous giant molecular cloud, over-dense regions become gravitationally bound and collapse. These collapsing cores heat up and protostellar cores develop, resulting in disk and outflow formation. The UV radiation from the young stellar object will ionise the surrounding region and progress to a hyper-compact, then an ultra-compact, HII region. The stellar wind and radiation pressure will expel any remaining natal molecular gas to reveal the OB association and HII region. Eventually high mass stars will devour their fusion material and violently explode as a supernova, leaving behind either a black hole or a neutron star/pulsar. As later explained in § 1.8 the high mass stellar evolutionary cycle plays an important role in the Galactic γ-ray sources. Inset binary image credit: NASA/Dana Berry.

NOTE:
This figure is included on page 10 of the print copy of the thesis held in the University of Adelaide Library.

Figure 1.6: In a series of balloon flights in 1912, Victor Hess made a breakthrough discovering 'cosmic radiation.' He concluded that "a radiation of very high penetrating power enters our atmosphere from above" Hess (1912).

randomised. It is not until the highest CR energies ($E_{\rm CR} > 10^{19}\,{\rm eV}$) that some directionality is preserved, as the ultra-high energy CRs have gyro-radii which are large on Galactic scales. Detectors like the Pierre Auger Observatory[2] are used for ultra-high energy CR astrophysics.

1.4.1 Charged Particle Acceleration

The most likely mechanism responsible for the acceleration of high-energy particles is diffusive shock acceleration (DSA). Supernova remnants (SNR) have long-been believed to be one of the main sources of Galactic cosmic rays. The standard method for particle acceleration was proposed by Fermi (1949), and has been extended to SNR shocks since the late 1970's (e.g. Axford *et al.* 1977; Bell 1978; Blandford & Ostriker 1978). The basic principle, when viewed in the frame of the stationary shock, is that material flows from upstream of the shock with velocity u_1, meets the shock boundary and is compressed by

[2]See `http://www.auger.org` for more details on the Pierre Auger Observatory

NOTE:
This figure is included on page 11 of the print copy of the thesis held in the University of Adelaide Library.

Figure 1.7: The local cosmic ray (CR) spectrum. The near perfect single power law spectrum extending over 10 orders of magnitude has two spectral features, the 'knee' at 10^{15} eV, and the 'ankle' at 10^{18} eV. CRs with energy up to the 'knee' are believed to be of Galactic origin, and of extra galactic origin for energies above the 'knee'. Image adapted from `http://astroparticle.uchicago.edu/sciam1.jpg`

a compression factor, $r = u_1/u_2$ It then flows downstream from the shock with reduced velocity u_2. Magnetic irregularities in both the upstream and downstream flows scatter charged particles across the shock, from upstream to downstream and vice-versa. Due to the symmetry between the upstream and downstream regions, each crossing of the shock, regardless of the direction, results in an average energy gain, $\langle \Delta E/E \rangle$ of order:

$$\left\langle \frac{\Delta E}{E} \right\rangle = \frac{2}{3}\frac{u_\mathrm{s}}{c} \tag{1.1}$$

where u_s is the speed of the shock and c is the speed of light in a vacuum ($c = 3 \times 10^8\,\mathrm{m\,s^{-1}}$). There is a finite probability that a particle will escape downstream from the shock. This downstream particle escape process creates a natural power law spectrum of:

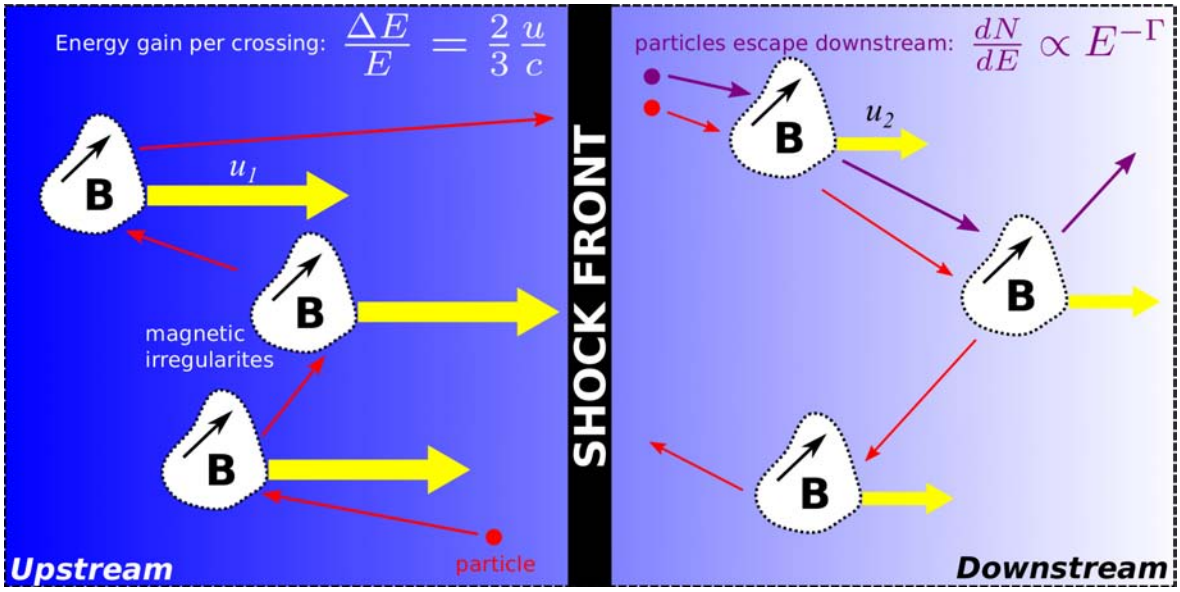

Figure 1.8: A schematic of particles crossing a shock and gaining energy. As seen in the rest frame of the shock, the upstream material flows into the shock with velocity u_1 and flows downstream with reduced velocity u_2. Particles will scatter off magnetic irregularities in both the upstream and downstream flows. They will then cross the shock boundary many times, each time gaining energy. Particles have a probability to escape downstream from the shock, which naturally produces a power law spectrum of escaped particles.

$$\frac{dN}{dE} \propto E^{-\Gamma} \tag{1.2}$$

where N is the number of particles escaping with energy E. For strong shocks $\Gamma \sim 2$. A detailed review of DSA can be found in Longair (1994). It should be noted that, although theory predicts that a SNR can accelerate particles and produce a particle spectrum with an E^{-2} power law, this is not conclusive proof that SNRs are the source of Galactic CRs. Observations are required to prove the theory.

1.5 γ-Ray Astronomy

As CRs lose directional information between the acceleration site and Earth, to locate the sites of CR acceleration, one must observe the uncharged by-products of CR acceleration. Neutrinos and γ-rays have directionality which are unaltered by interstellar magnetic fields. Neutrinos would be the best probe of CR acceleration sites as they will travel in a straight, unimpeded path from their origin to Earth. However, it is these same properties which make neutrino detection challenging. One experiment trying to

search for these extremely rare neutrino interactions is the IceCube[3] telescope at the South Pole. Since neutrino detection is difficult, this leaves the γ-rays resulting from CR interactions as the most accessible avenue for tracing sites of CR acceleration.

The relatively young field of γ-ray astronomy involves searching for high-energy photons (more than 10^9 times more energetic than visible light) emitted from celestial bodies. γ-ray energies are presumed to span approximately 14 decades of energy, from $10^6 - 10^{20}$ eV. However, this vast energy range is rather sparsely sampled, and with very different detection methods. The so called soft γ-rays ($E_\gamma \leq 15$ MeV; 1 MeV = 10^6 eV) are detected by space based satellites like *Swift*[4], *Fermi*[5] and *INTEGRAL*[6]. High-energy γ-rays ($E_\gamma \sim$30 MeV to 100 GeV; 1 GeV = 10^9 eV) are detected by satellites like *EGRET*[7], *Fermi* and *Agile*[8]. The low fluxes of very-high energy (VHE) γ-rays ($E_\gamma \geq 100$ GeV) are beyond the area limitations of space-based detectors and require a ground-based detection technique, the imaging atmospheric Cherenkov technique (IACT) which will be explained later in § 6.1. Current ground-based VHE γ-ray detectors include *H.E.S.S.*[9], *MAGIC* [10] and *VERITAS* [11]. For a review of TeV astronomy see Hinton & Hofmann (2009) and references therein.

1.6 VHE γ-Ray Production

Most electromagnetic radiation is generated thermally, the hotter the object, the more energetic the radiation it emits. This process is well understood and governed by Planck's Law. For the hottest regions in space (that are known), the accretion disks around young stellar objects (YSO), the thermal radiation predicted by Planck's Law only reaches X-ray energies, a few tens of keV (10^3 eV). This is still orders of magnitude lower than the soft γ-rays, let alone the VHE γ-rays. No physical object can be hot enough to produce appreciable γ-rays at the highest energies. Therefore, VHE γ-rays are produced by 'non-thermal' processes. The production of γ-rays can be classified

[3]See `http://www.icecube.wisc.edu/` for more information on the IceCube detector.

[4]See `http://heasarc.nasa.gov/docs/swift/swiftsc.html` for more information on the Swift mission.

[5]See `http://fermi.gsfc.nasa.gov/` for more information on the Fermi project.

[6]See `http://www.esa.int/esaMI/Integral/index.html` for more information on the INTEGRAL mission.

[7]See `http://heasarc.gsfc.nasa.gov/docs/cgro/egret/egret_tech.html` for technical information on the EGRET system.

[8]See `http://agile.rm.iasf.cnr.it/` for more information on the Agile mission.

[9]See § 6.2 and `http://www.mpi-hd.mpg.de/hfm/HESS/` for more information on the H.E.S.S. project.

[10]See `http://wwwmagic.mppmu.mpg.de/` for more information on the MAGIC project.

[11]See `http://veritas.sao.arizona.edu/` for more information on the VERITAS project.

into two categories, hadronic emission and leptonic emission. The hadronic emission process involves inelastic collisions between hadrons (protons, neutrons and nuclei) which produce neutral pions (π^0) that subsequently decay into γ-rays. Leptonic processes involve leptons (electrons and positrons) interacting with ambient photon fields to produce γ-rays through Inverse Compton (IC) scattering. An important parameter to consider for the production of γ-rays is the cooling time, τ, which is the time scale over which the process is effective for leptons in a particular source region. The cooling time is a useful parameter for determining the emission mechanism, as the process with the lowest cooling time is generally the dominant emission mechanism. The following sections briefly outline the γ-ray emission mechanisms and formulae for the cooling time are summarised in Table 1.2.

1.6.1 The Hadronic Emission Mechanism

Decay of Neutral Pions

Collisions between relativistic protons and nuclei create a number of secondary particles, which include pions, π. The neutral pion, π^0, has a primary decay mode, with 99% probability, whereby it decays into two γ-ray photons, that is:

$$\pi^0 \longrightarrow 2\,\gamma \tag{1.3}$$

This mode, with mean lifetime $8.4{\times}10^{-17}\,$s, is an effective channel for converting the kinetic energy of the incoming hadrons into γ-rays. It has been extensively studied (e.g. Stecker (1971); Dermer (1986); Mori (1997) etc..) and it has been shown that, for γ-rays with $E_\gamma > 1\,\mathrm{GeV}$, the γ-ray spectrum follows closely that of the parent protons (Aharonian, 2004). This property implies that the γ-ray spectrum from hadronic interactions carries direct information about the spectrum of the parent CRs at the site of acceleration. The cooling time for the decay of π^0s can be expressed as a function of: the density of target protons, n_0; the cross section for $p\,p$ interactions, σ_{pp}, and a coefficient of inelasticity, f. Taking typical values Aharonian & Atoyan (2000) find that:

$$\tau_{pp} \approx 5.3 \times 10^7 \left(\frac{n}{\mathrm{cm}^{-3}}\right)^{-1} \quad [\mathrm{yr}] \tag{1.4}$$

where n is the number density of target protons. For a more detailed review see Aharonian (2004).

1.6.2 Leptonic Emission Mechanisms

Inverse Compton Scattering

The interaction between relativistic electrons (in the following sections, 'electron' stands for 'electron and positron') with ambient photon fields is often the most important of the leptonic emission mechanisms for γ-ray production. The inverse Compton (IC) process involves scattering low energy photons up to γ-ray energies through collisions with high energy leptons (Blumenthal & Gould, 1970). The IC process is very common as photon fields such as infra red (IR), optical and X-ray, exist throughout the Galaxy, as well as the 2.7 K cosmic microwave background radiation (CMB) which permeates the universe. For the IC process, the cooling time is given by (Moderski *et al.*, 2005, and erratum):

$$\tau_{\rm ic} \approx 3.1 \times 10^5 \left(\frac{U_{\rm rad}}{\rm eV\,cm^{-3}}\right)^{-1} \left(\frac{E_e}{\rm TeV}\right)^{-1} f_{\rm KN}^{-1} \quad [\rm yr] \tag{1.5}$$

where $U_{\rm rad}$ is the energy density of the target photon field, E_e is the energy of the electrons and $f_{\rm KN}$ is a Klein-Nishina suppression factor:

$$f_{\rm KN} \approx (1+b)^{-1.5} \approx \left[1 + 40\left(\frac{E_e}{\rm TeV}\right)\left(\frac{kT}{\rm eV}\right)\right]^{-1.5} \quad (\text{for } b < 10^4) \tag{1.6}$$

where b is a measure of the electron energy, k is the Boltzmann constant ($k = 8.617 \times 10^{-5}\,\rm eV\,K^{-1}$) and T is the temperature. In the Klein-Nishina regime the scattering cross section decreases with electron energy. Hence, the IC process becomes less effective, creating a cut-off in the photon spectrum at energies $E_\gamma \sim 50\,\rm TeV$.

Synchrotron Emission

When energetic charged particles are accelerated in a simple magnetic field they spiral around the field lines. This motion causes the particles to emit continuous, polarised radiation. The intensity of the synchrotron radiation is dependent on both the magnetic field strength and the energy of the particles. Typically, synchrotron emission only reaches GeV energies. The cooling time associated with synchrotron emission is characterised by (Moderski *et al.*, 2005, and erratum):

$$\tau_{\rm s} \approx 1.3 \times 10^7 \left(\frac{B}{\mu\rm G}\right)^{-2} \left(\frac{E_e}{\rm TeV}\right)^{-1} \quad [\rm yr] \tag{1.7}$$

where B is the magnetic field strength and E_e is the electron energy.

Process	Cooling Time [yr]	Framework
Pion Decay	$\tau_{pp} = 5.3 \times 10^7 \left(\frac{n}{\mathrm{cm}^{-3}}\right)^{-1}$	Hadronic
Inverse Compton	$\tau_{\mathrm{ic}} \approx 3.1 \times 10^5 \left(\frac{U_{\mathrm{rad}}}{\mathrm{eV\,cm}^{-3}}\right)^{-1} \left(\frac{E_e}{\mathrm{TeV}}\right)^{-1} f_{\mathrm{KN}}^{-1}$	Leptonic
Synchrotron	$\tau_{\mathrm{s}} \approx 1.3 \times 10^7 \left(\frac{B}{\mu\mathrm{G}}\right)^{-2} \left(\frac{E_e}{\mathrm{TeV}}\right)^{-1}$	Leptonic
Bremsstrahlung	$\tau_{\mathrm{b}} \approx 3.9 \times 10^7 \left(\frac{n}{\mathrm{cm}^{-3}}\right)^{-1}$	Leptonic

Table 1.2: A summary of the cooling times associated with the VHE γ-ray production mechanisms.

Bremsstrahlung

Bremsstrahlung (braking radiation) describes the radiation released when an electron is deflected by the electric field of another charged particle. This produces continuum radiation, as the particles undergo multiple deflections by varying degrees. There is a possibility that the electron will be completely stopped in a single interaction, which gives a sharp cut off to the spectrum at the energy of the highest electron present. The cooling time associated with Bremsstrahlung emission is energy independent, with loss rates dependent on the medium. For neutral hydrogen atoms at density n, the cooling time is:

$$\tau_{\mathrm{b}} \approx 3.9 \times 10^7 \left(\frac{n}{\mathrm{cm}^{-3}}\right)^{-1} \quad [\mathrm{yr}] \tag{1.8}$$

1.7 The Connection between Hadronic γ-Ray Emission and Dense Molecular Gas

Under the hadronic emission scenario, the γ-rays are produced via CR collisions giving rise to π^0 which decay into the γ-rays (§ 1.6.1). This means that regions containing dense gas ($n > 10^3\,\mathrm{cm}^{-3}$) provide a target for high energy CRs to interact and produce hadronic γ-ray emission. Therefore, evolved high mass star forming regions provide an excellent environment for hadronic γ-ray emission. As indicated in § 1.3, high mass stars are deeply embedded in GMCs and end their lives in supernovae explosions, creating pulsars or black holes. This combination of (e.g. SNR) accelerated particles (§ 1.4.1) coupled with the presence of nearby dense molecular gas provides a favourable

environment for hadronic γ-ray emission.

For γ-ray emisison, $E_\gamma >> 100\,\mathrm{MeV}$, the flux of γ-ray photons, ph, under the hadronic interpretation is given by (Aharonian, 1991):

$$F(>E_\gamma) = 2.85 \times 10^{-13} \left(\frac{E_\gamma}{\mathrm{TeV}}\right)^{-1.6} \left(\frac{M}{10^5 \mathrm{M}_\odot}\right) \left(\frac{d}{\mathrm{kpc}}\right)^{-1} k_{\mathrm{CR}} \quad [\mathrm{ph\,cm^{-2}\,s^{-1}}] \quad (1.9)$$

where E_γ is the γ-ray energy, M is the mass of the cloud, d is the distance to the cloud and k_{CR} is the CR enhancement factor above the local solar-system value.

As previously discussed, determining the process which forms γ-ray emission is often challenging. For many sources, both the hadronic and leptonic emission mechanisms can explain the observed γ-ray emission. Typically, leptonic emission dominance requires low magnetic field strengths, to prevent synchrotron cooling losses (Table 1.2), and low and gas densities. In regions of dense gas, these requirements contradict with both the high gas density and the magnetic field enhancements seen towards dense gas (Crutcher, 1991). These ideas are discussed in § 4.

1.8 Sources of VHE γ-Rays

The following section outlines the varying types of sources which have been detected as TeV γ-ray emitters. The sources are divided into three categories: Galactic, extragalactic and unidentified. A summary of the known VHE γ-ray sources broken down by source type is presented in Table 1.3 and a skymap showing the locations of the current catalogue of TeV sources is presented in Figure 1.9.

1.8.1 Galactic Sources

The stellar evolutionary cycle for high mass stars is particularly relevant in the field of VHE γ-ray astronomy as all known Galactic TeV ($10^{12}\,\mathrm{eV}$) sources are associated, either directly or indirectly, with high mass stellar evolution. The end point of high mass stars, supernova remnants and pulsars, as well as binary systems of high mass stars with compact companions, are TeV emitters. In the following paragraphs I briefly summarise the categories of Galactic TeV γ-ray sources.

Supernova Remnants

Supernova explosions release the order of $10^{51}\,\mathrm{erg}$ ($1\,\mathrm{erg} = 10^{-7}\,\mathrm{J}$) of kinetic energy into the surrounding ISM. The resulting shock waves have initial speeds of several thousands

Source Type	Number Confirmed
Supernova Remnant	13
Pulsar/Pulsar Wind Nebulae	32
Binary Systems	7
Stellar Cluster	3
Extra galactic	42
Unidentified	37
Total	134

Table 1.3: The known VHE γ-ray sources broken down by source type, as of January 2011. A complete and up-to-date TeV catalogue TeVCAT created by S. Wakely and D. Horan can be seen at `http://tevcat.uchicago.edu/`.

of kilometres per second, which gradually decrease over time. Electrons (and positrons) are accelerated effectively at the shock front, leading to synchrotron radiation in the presence of magnetic fields, Bremsstrahlung radiation and IC scattering on CMB or other photon fields. Accelerated hadrons give rise to inelastic collisions with ambient matter producing π^0 mesons which subsequently decay into γ-rays. A prime example of a shell-like VHE SNR is RX J1713−3946 (Aharonian *et al.*, 2006a). The best example of a SNR interacting with the surrounding ISM is the W28 SNR (Aharonian *et al.*, 2008), discussed further in § 1.9.

Pulsars and Pulsar Wind Nebulae

Pulsars are highly magnetised, rapidly rotating neutron stars resulting from a supernova explosion. The pulsar-generated wind of charged particles accelerated by the strong magnetic fields interacts with the ambient medium, generating a shocked region where particles are accelerated. This results in both pulsed VHE emission from the pulsar itself and un-pulsed VHE emission from the pulsar wind nebulae (PWN) (Aliu *et al.*, 2008). The most studied and best example of a PWN is the Crab Nebula (e.g. Aharonian *et al.* 2006b).

Binary Systems

A binary system consists of two objects, usually a compact object and a high mass star, orbiting a common centre of mass. The compact object (black hole or neutron star) will accrete material from its companion, creating a disk and outflow jets. Galactic binary systems with relativistic jets, so called 'microquasars', reveal that non-thermal processes accelerate electrons to high energies which, under the right conditions, can produce VHE emission via IC scattering of photon fields or interactions between the

Figure 1.9: The current catalogue of TeV γ-ray sources plotted on the sky in Galactic coordinates, with a zoom for the Galactic plane. Image from Hinton & Hofmann (2009).

relativistic jet and stellar winds. An example of a microquasar producing VHE emission is Cygnus X−1 (Albert *et al.*, 2007). A study searching for TeV γ-ray emission from three microquasars interacting with the ISM, using the H.E.S.S. telescopes, is presented in § 6.

Stellar Clusters

The possibility of VHE emission from colliding stellar winds has been recently discussed in the literature (e.g. Benaglia & Romero 2003; Pittard & Dougherty 2006; Reimer *et al.* 2006), although concrete evidence has yet to be seen. The best observational evidence for stellar wind production of VHE γ-rays would be Westerlund 2 (Aharonian *et al.*, 2007), which is the second largest concentration of young high mass stars in our Galaxy. However, as all other known VHE sources are associated with high mass stellar evolution, the emission may be from a single object within the cluster (e.g., PWN, SNR) rather than the cluster as a whole.

Unidentified Sources

Approximately 30% of the detected VHE γ-ray sources remain unidentified. These sources have no known counterparts at other wavelengths. For this reason, they are commonly known as 'dark accelerators'. Several dark sources have led to the discovery of new SNRs and pulsars through follow-up observations. An example is HESS 1813−178, which has since been identified as a PWN (Helfand *et al.*, 2007). However, many sources remain mysterious, even after sensitive follow up measurements at other wavelengths. Unidentified sources often have more 'exotic' explanations, such as dark matter annihilation, for their origin (e.g. Ripken *et al.* (2008) investigated whether HESS J1303−63 is a dark matter clump). Additionally, γ-ray bursts, hypernovae and old SNRs are also possible dark accelerators.

1.8.2 Extra-galactic Sources

Extra-galactic sources of VHE emission are dominated by active galactic nuclei (AGN). With a few exceptions, the AGN sources are in the blazar class, where a jet points towards the Earth. Detected extra-galactic VHE γ-ray sources include high, intermediate and low frequency peaked BL Lac objects (HBL, IBL, LBL), flat spectrum radio quasars (FSRQ), Fanaroff-Riley Class I objects (FR-I) and starburst galaxies.

1.9 The W28 Supernova Remnant

Giant molecular clouds populate the Galactic plane towards the Galactic centre. Within this region lies the W28 SNR, with Galactic co-ordinates $(l, b = 6.4, -0.1)$. The SNR was given the W28 name as it was the 28^{th} object identified in the list of sources compiled by Westerhout (1958). The W28 SNR (G6.4−0.1) is an old-age $> 10^4$ yr. (Kaspi *et al.*, 1993), mixed morphology SNR estimated to be at a distance of 1.2 – 3.3 kpc (Goudis, 1976; Lozinskaya, 1981; Motogi *et al.*, 2011). The mixed morphology class of SNRs are categorised by shell-like radio emission and centre-filled thermal X-ray emission (Rho & Petre, 1998). It has been detected across the EM spectrum, from radio (Dubner *et al.*, 2000), X-ray (Rho & Borkowski, 2002; Ueno *et al.*, 2003) & γ-ray energies (e.g. MeV energies by Pollock 1985; Sturner & Dermer 1995; Esposito *et al.* 1996 and Zhang & Cheng 1998, GeV energies by Abdo *et al.* 2010; Giuliani *et al.* 2010 and TeV energies by Aharonian *et al.* 2008). The W28 SNR is pictured in Figure 1.10 as a three colour image with radio emission in red, X-ray emission in blue and optical emission in greyscale. The W28 region is rich with information covering all stages of stellar evolution. Obviously, the W28 SNR indicates the end of high

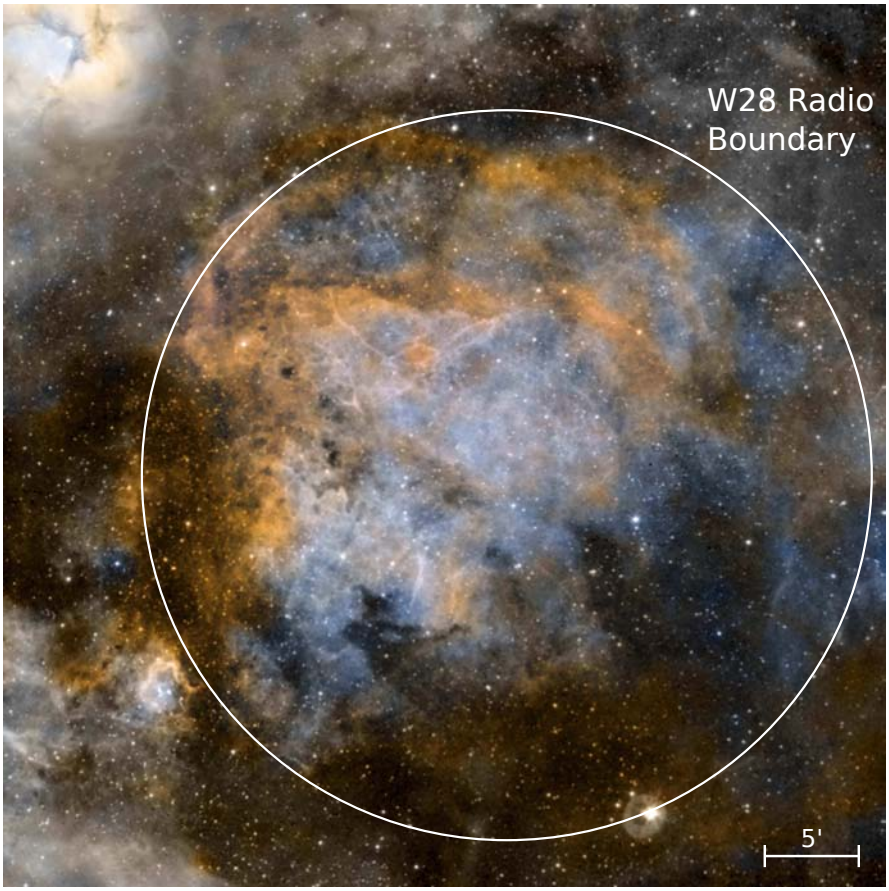

Figure 1.10: The mixed morphology supernova remnant W28. The red colour channel is VLA radio emission revealing the shell-like structure. The blue channel is ROSAT X-ray emission revealing the generally centre-filled morphology. The grey-scale is optical emission revealing the background stars and fine structure. The white circle represents the approximate radio boundary. Image credits: ROSAT X-ray: NASA/ROSAT; Optical: NOAO/CTIO/P.F. Winkler et al; Radio: NSF/NRAO/VLA/G. Dubner et al.

mass stellar evolution, however, along with the W28 SNR, two additional SNRs are identified within the field, each with an unknown distance, G6.67−0.42 (Yusef-Zadeh *et al.*, 2000) and G5.71−0.08 (Brogan *et al.*, 2006). To the north-east of W28 lies the giant ionised HII region M20 (e.g Lefloch *et al.* 2008), just visible in the top left corner of Figure 1.10, indicating an evolved site of high mass star formation. To the south of W28 multiple HII regions, in various stages of evolution, are present including the bright and energetic HII complex G5.89−0.39.

The TeV γ-ray sources detected by the H.E.S.S. telescopes are spatially well-matched to molecular clouds which surround the SNR. The NANTEN CO (1-0) emission (Mizuno & Fukui, 2004) traces molecular clouds with gas densities $n \sim 7 \times 10^2\,\mathrm{cm}^{-3}$. The spatial overlap between the TeV sources and the molecular gas becomes more apparent with the higher angular resolution CO (2-1) observations (Fukui *et al.*,

2008), tracing gas densities $n \sim 7 \times 10^3\,\mathrm{cm}^{-3}$, as indicated in Figure 1.11.

Figure 1.11: Image showing the spatial overlap between the molecular gas and the TeV γ-ray emission. The NANTEN CO (2-1) integrated intensity (-10 to 25 km s^{-1}) image is overlaid with yellow contours of H.E.S.S. TeV γ-ray significance (4, 5 & 6 σ levels). White stars represent HII regions within the southern clouds. The white circle represents the approximate W28 radio boundary as seen on Figure 1.10 to give an indication of scale between the images. Image adapted from Nakashima *et al.* (2008).

The W28 SNR field provides a unique laboratory to study both the dense molecular gas and TeV γ-ray emission. In the W28 region, the connection with dense molecular gas suggests a hadronic origin for the γ-ray emission. Studies of the dense molecular gas in the region will provide information on the mass and density distribution of the molecular gas. This information is essential in understanding the properties of the CRs in the region, such as, the CR density profile, CR diffusion and the origin of the high energy CRs in the region. The diffusion of CRs into molecular clouds is discussed in Gabici *et al.* (2007). For higher gas densities, the exclusion of low energy ($\leq$ GeV) CRs increases. This means that towards dense molecular cores a harder γ-ray spectrum, than that of the entire cloud, is expected as shown in Figure 1.12. Observations of dense molecular gas towards sites of γ-ray emission, like W28, are the

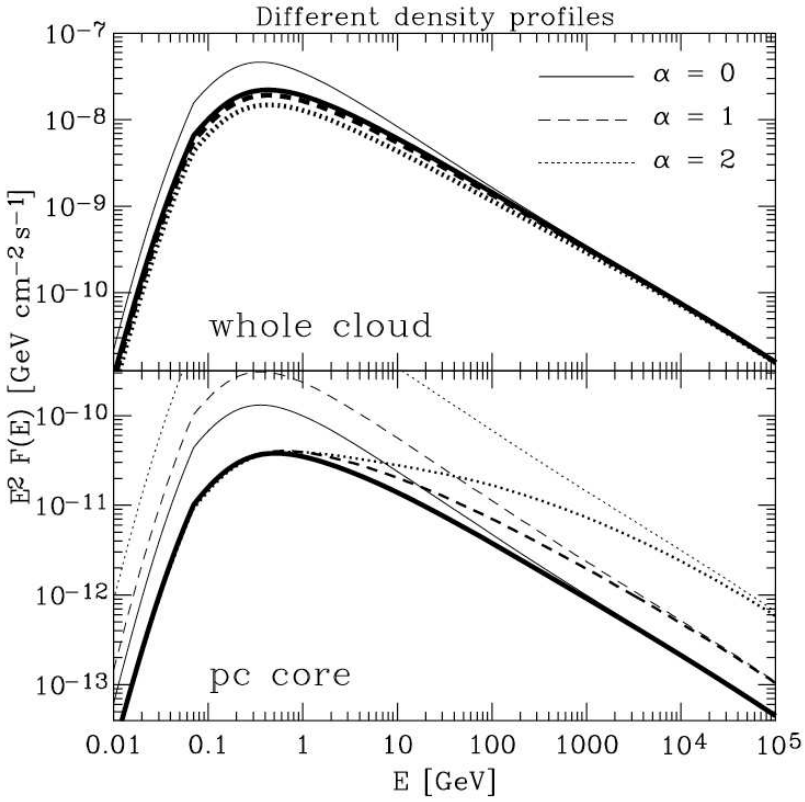

Figure 1.12: The γ-ray spectrum from the entire molecular cloud vs. that of the dense cloud core. The thick lines represent the γ-ray emission from π^0 decay, for three different density profiles (α). The thin lines indicate the γ-ray emission if all CRs can freely penetrate the cloud. Due to the exclusion of low energy ($\leq$ GeV) CRs, the γ-ray spectrum becomes harder towards the cloud core. Image adapted from Gabici *et al.* (2007).

first steps towards determining the effects of CR diffusion and provide motivation for higher angular resolution TeV γ-ray instrumentation and observations.

1.10 Multi-Wavelength Observations

A significant challenge over the past 20 years has been to identify the origin of CRs. The rapid developments in γ-ray astronomy since the first confirmed TeV γ-ray detection of the Crab Nebula (Weekes *et al.*, 1989), have resulted in many confirmed VHE γ-ray sources. These sources have provided information on the CR spectrum at the source, provided that the γ-rays are of hadronic origin. However, as outlined in § 1.6, γ-ray emission can also be produced by leptons. This leads to another challenging question, "What is the origin of the γ-ray emission?"

Alone, a γ-ray signal generally does not provide enough information to determine the emission mechanism, multi-wavelength information is essential. In the absence of

multi-wavelength data, a γ-ray detection simply implies that there is a source of γ-rays in a particular direction. It cannot conclusively tell you how far away or what is the source[12]. This additional information is only provided through observations at different wavelengths. The radio continuum and millimetre waves from different molecules, can be combined to determine the ambient gas density and its distribution throughout the Galaxy. Radio to X-ray observations can give limits on the magnetic field strength and provide information on the photon fields which can be IC scattered to γ-ray energies. The cooling times for the different γ-ray production mechanisms presented in § 1.6 reveal that the radiation field, magnetic field and gas density must be known in order to determine the cooling time, and hence provide an idea of which production mechanism is dominant. This additional information is only provided through observations at different wavelengths. It is by combining all the information from multiple wavebands that the 'bigger picture' is revealed (e.g. as seen in Figures 1.2 and 1.3). The 'bigger picture' may allow the source, and properties, of the γ-ray emission to be identified. In turn these can help to answer the fundamental questions of cosmic ray physics, "Where do VHE CRs come from?" and "How are they accelerated to such high energies?"

[12]although arguments based on physical size and energy (e.g. distance luminosity relations) can provide some general distance constraints

CHAPTER II

Radiative Transfer Fundamentals

In order to understand the universe, astronomers study electromagnetic radiation from space. Over time, their observations have progressed through different wavebands. For thousands of years astronomers were limited to the visible band. It wasn't until the 1930s, when Karl Jansky detected radiation with wavelength 14.6 m coming from space (Jansky, 1933), that the field of radio astronomy began. In order to exploit this new 'invisible window' to the universe, radio astronomers must understand the theory of electromagnetic radiation.

This chapter is separated into three parts. The first part of the chapter outlines the fundamentals of single dish radio astronomy. It begins with the general form of the equation of radiative transfer (ERT) and outlines some general solutions to it. It also presents the detection equation, which is an extension of the ERT for modern telescopes, and applies the theory of radiative transfer to molecular species in a two level system. The second part of this chapter outlines how we trace dense molecular gas in the interstellar medium. As indicated in § 1.7 dense gas plays an important role in hadronic γ-ray emission. It also presents how molecular line observations can be used to determine some physical gas parameters such as optical depth, column density and rotational temperature. The final part of the chapter focuses on the ammonia molecule, an exceptionally useful molecule for astrophysical applications. It outlines the ammonia spectrum and how ammonia observations can be used to determine dense gas parameters.

In the following sections, the information, equations and derivations are based on a host of radio astronomy textbooks: Townes & Schallow (1955); Pacholczyk (1970); Spitzer (1978); Rohlfs (1986) and Elitzur (1992). Additional work presented in this chapter is from the papers of Barrett *et al.* (1977); Ho & Townes (1983); Ungerechts *et al.* (1986); Goldsmith & Langer (1999) and Tafalla *et al.* (2004).

2.1 Equation of Radiative Transfer

The specific intensity of radiation, I_ν, at frequency, ν, ($\mathrm{Jy\,sr^{-1}}$, $\mathrm{Jy} = 10^{-26}\,\mathrm{W\,m^{-2}\,Hz^{-1}}$) from a source in free space remains unchanged. This means that the only way I_ν can change, in transit from the source to the observer, is through absorption and/or emission, as indicated in Figure 2.1. This change in intensity, dI_ν, is described by the Equation of Radiative Transfer.

For radiation travelling through some medium of thickness, ds, the change in intensity, dI_ν, is given by two terms, an emission term, dI_+, and an absorption term, dI_-, which are expressed as:

$$dI_+ = j_\nu(s) \tag{2.1}$$

$$dI_- = -\alpha_\nu(s)\, I_\nu(s) \tag{2.2}$$

where $j_\nu(s)$ is the emission coefficient ($\mathrm{W\,m^{-3}\,Hz^{-1}\,sr^{-1}}$) and $\alpha_\nu(s)$ is the absorption coefficient ($\mathrm{m^{-1}}$). Combining these terms gives the Equation of Radiative Transfer:

$$\frac{dI_\nu}{ds} = -\alpha_\nu(s)\, I_\nu + j_\nu(s) \tag{2.3}$$

There are some limiting cases which result in simple solutions to the transfer equation. These are briefly outlined below.

1. **Emission Only ($\alpha_\nu(s) = 0$):** There is no absorption by the medium in which case Equation 2.3 reduces to:

$$\frac{dI_\nu}{ds} = j_\nu(s) \tag{2.4}$$

which has solution:

$$I_\nu(s) = I_\nu(0) + \int_s j_\nu(s) ds \tag{2.5}$$

where $I_\nu(0)$ is a background radiation source.

2. **Absorption Only ($j_\nu(s) = 0$):** There is no emission by the medium in which case Equation 2.3 reduces to:

$$\frac{dI_\nu}{ds} = -\alpha_\nu(s)\, I_\nu(s) \tag{2.6}$$

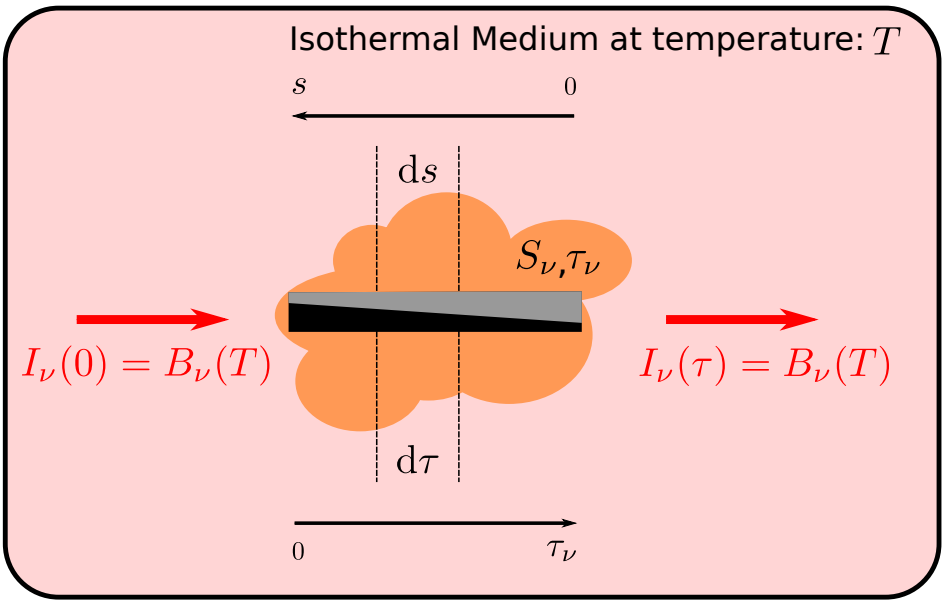

Figure 2.1: A schematic illustrating how radiation, I_ν, is affected by attenuation (solid black region) and the self regulated gain by the medium (grey region) in an isothermal medium. The change in radiation, dI_ν, over any finite length interval, ds, is governed by the Equation of Radiative Transfer (ERT), Equation 2.3. The ERT completely describes the properties of the medium in terms of its absorption, α_ν, and emission, j_ν. From the definition of the optical depth, Equation 2.10, τ_ν and s increase in opposite directions. This optical depth property implies that observations aimed to penetrate the medium require the medium to be optically thin.

which has solution of:

$$I_\nu(s) = I_\nu(0) \exp\left(\int_s -\alpha_\nu(s)\, ds\right) \tag{2.7}$$

3. **Thermal Equilibrium/Local Thermal Equilibrium (LTE):** The distribution of radiation from a black body in thermodynamic equilibrium with kinetic temperature T, is governed by Planck's black body function, $B_\nu(T)$, which is defined as:

$$B_\nu(T) = \frac{2h\nu^3}{c^2} \frac{1}{\exp\left(\frac{h\nu}{kT}\right) - 1} \tag{2.8}$$

Where h is Planck's constant ($h = 6.64 \times 10^{-34}\,\mathrm{kg\,m^2\,s^{-1}}$), k is the Boltzmann constant ($k = 1.38 \times 10^{-23}\,\mathrm{J\,K^{-1}}$) and c is the speed of light in a vacuum. In the case of LTE, Kirchhoff's Law states that the emission and absorption are balanced:

$$\frac{j_\nu}{\alpha_\nu} = B_\nu(T) \tag{2.9}$$

Generally the absorption of radiation through a medium is characterised by the optical depth, τ_ν, defined in the differential case as:

$$d\tau_\nu = \alpha_\nu \, ds \tag{2.10}$$

Dividing Equation 2.3 by α_ν:

$$\frac{dI_\nu}{\alpha_\nu ds} = -I_\nu + \frac{j_\nu}{\alpha_\nu} \tag{2.11}$$

and substituting in the optical depth from Equation 2.10 gives an alternate and more practical form of the transfer equation:

$$\frac{dI_\nu}{d\tau_\nu} = -I_\nu + S_\nu \tag{2.12}$$

where j_ν/α_ν is known as the source function S_ν which completely describes the properties of the medium. Solving Equation 2.12 gives:

$$I_\nu(\tau) = S_\nu + \mathrm{e}^{-\tau} \left(I_\nu(0) - S_\nu \right) \quad [\mathrm{J\,sr^{-1}}] \tag{2.13}$$

Equation 2.13 is the general solution to the Equation of Radiative Transfer for a homogeneous, isothermal medium. That is, that the observed intensity of radiation passing through a medium of thickness, s, is given by the sum of the attenuated radiation from the background radiation source, $I_\nu(0)\, e^{-\tau_\nu}$, and the self regulated gain of radiation emitted by the medium, $S_\nu \left(1 - e^{-\tau_\nu}\right)$. A schematic of radiation passing through an isothermal medium is illustrated in Figure 2.1.

2.1.1 Brightness Temperature from a Black Body

If the source of radiation is in local thermal equilibrium (LTE) with its surroundings, it may be treated as a black body, and will be governed by the Planck Law (Equation 2.8). At radio frequencies, the quantity $h\nu/kT$ is sufficiently small that a power series expansion:

$$\exp\left(\frac{h\nu}{kT}\right) = 1 + \frac{h\nu}{kT} + \frac{(h\nu/kT)^2}{2!} + \frac{(h\nu/kT)^3}{3!} + \dots \tag{2.14}$$

$$\approx 1 + \frac{h\nu}{kT} \tag{2.15}$$

can be applied to the Planck Law (Equation 2.8) to give the Rayleigh-Jeans law:

$$B_{\mathrm{RJ}} \approx \frac{2\nu^2}{c^2} kT \tag{2.16}$$

This can be rearranged for the brightness temperature giving:

$$T_b(\nu) = \frac{c^2}{2k}\frac{1}{\nu^2} I_\nu \quad [K] \tag{2.17}$$

Substituting the brightness temperature back into Equation 2.12 and describing the source function by the temperature of the medium at position s gives:

$$\frac{dT_b}{d\tau_\nu} = T_{\mathrm{src}}(\nu) - T_{\mathrm{bkg}}(\nu) \tag{2.18}$$

where $T_{\mathrm{src}}(\nu)$ is the temperature of the medium and $T_{\mathrm{bkg}}(\nu)$ is the temperature of the background radiation. This has solution:

$$T_b(\nu) = T_{\mathrm{bkg}}(\nu)\,\mathrm{e}^{-\tau_\nu} + T_{\mathrm{src}}(\nu)\left(1 - \mathrm{e}^{-\tau_\nu}\right) \quad [\mathrm{K}] \tag{2.19}$$

This is analogous to Equation 2.13, except now it relates the emission in terms of brightness temperatures.

2.2 The Detection Equation

Frequently modern astronomical telescopes employ a source and background subtraction to detect the excess emission above a background (e.g. the cosmic microwave background). In this way the excess emission detected by the telescope is found via Equation 2.19:

$$T_b(\nu) = T_{\mathrm{A}}^*(\nu) = T_{\mathrm{bkg}}(\nu)\,\mathrm{e}^{-\tau_\nu} + T_{\mathrm{src}}(\nu)\left(1 - \mathrm{e}^{-\tau_\nu}\right) - T_{\mathrm{bkg}}(\nu) \tag{2.20}$$

$$= \left(T_{\mathrm{src}}(\nu) - T_{\mathrm{bkg}}(\nu)\right)\left(1 - \mathrm{e}^{-\tau_\nu}\right) \quad [K] \tag{2.21}$$

Here $T_{\mathrm{A}}^*(\nu)$ is the signal measured by the detector at frequency ν, from a source at

temperature $T_{\rm src}$, above a background of temperature $T_{\rm bkg}$, through a medium with optical depth τ_ν. More details on the detection equation and the calibration of single dish molecular line emission, employing a source (ON) and background (OFF) subtraction, are discussed later in § 3.1.5.

2.3 Molecular Line Radiative Transfer

Molecular line radiative transfer is used to determine the relative populations of atoms and molecules in various excited states, given the physical conditions of the region. For simplicity, an approximation of a 'two level' system is used to determine the energy levels of interest. The following section outlines the two level system approximation.

2.3.1 Level Populations

In a molecular system, the number of molecules in any particular state is governed by the Boltzmann distribution:

$$\frac{n_{\rm u}}{n_0} = \frac{g_{\rm u}}{g_0} \exp\left(\frac{-(E_{\rm u} - E_0)}{kT_{\rm ex}}\right) \tag{2.22}$$

where $n_{\rm u}$ is the number density of molecules in an upper state and n_0 is the number density of molecules in the ground state. $E_{\rm u}$ and E_0 are the energies of the upper and ground states and $g_{\rm u}$ and g_0 are the upper and ground level degeneracies. Under LTE conditions the excitation temperature, $T_{\rm ex}$[1], will be equal to the kinetic temperature, $T_{\rm kin}$[2].

While the determination of the number of molecules in a single state is useful for applications in astrophysics, the total number of molecules in all states, n, is generally the desired property. This is found via a sum over all states, i, that is:

$$n = \sum_{i=0}^{\infty} n_i \tag{2.23}$$

If the energy levels are populated according to the Boltzmann distribution, the total number density of molecules in all states can be inferred. Re-writing the Boltzmann distribution for any state i by substituting $u \rightarrow i$ in Equation 2.22 gives:

[1]The excitation temperature, $T_{\rm ex}$, is the temperature which is required to produce a system with the observed level populations

[2]The kinetic temperature, $T_{\rm kin}$, is the temperature of the system defined by the kinetic energy of the particles.

$$
\begin{aligned}
n &= n_0 \sum_{i=0}^{\infty} \frac{g_i}{g_0} \exp\left(\frac{-(E_i - E_0)}{kT_{\rm ex}}\right) \\
&= \frac{n_0}{g_0} \exp\left(\frac{E_0}{kT_{\rm ex}}\right) \left[\sum_{i=0}^{\infty} g_i \exp\left(\frac{-E_i}{kT_{\rm ex}}\right)\right] \\
&= \frac{n_0}{g_0} \exp\left(\frac{E_0}{kT_{\rm ex}}\right) Q(T_{\rm ex}) \qquad (2.24)
\end{aligned}
$$

The partition function, $Q(T_{\rm ex})$, normalises the distribution and ensures that the sum of molecules in all energy levels produces the total number of molecules, n.

2.3.2 The Einstein Coefficients

In the following section, consider a two level system with a lower level, state 1, and an upper level, state 2. The subscript notation X_{21} is a shortened form for $X_{2\rightarrow1}$ and indicates the transition from the upper state 2, to the lower state 1. Similarly, X_{12} indicates the transition from the lower state 1, to the upper state 2.

The Einstein coefficients describe how radiation is emitted and absorbed within a molecular system. The Einstein coefficients for radiative processes are:

- **The Spontaneous Emission Rate A_{21}:** The probability of spontaneous emission from an upper state to a lower state with no outside influences (s^{-1}).
- **The Stimulated Emission Rate B_{21}:** The probability of an external photon stimulating a second emission from an upper state to a lower state ($\mathrm{sr\,m^{-2}\,Hz\,W^{-1}\,s^{-1}}$).
- **The Spontaneous Absorption Rate B_{12}:** The probability of absorbing an external photon resulting in a transition from a lower state to an upper state ($\mathrm{sr\,m^{-2}\,Hz\,W^{-1}\,s^{-1}}$).

The B coefficients are dependent on the energy density of the ambient photon fields. Einstein coefficients are unique to each molecular transition and are governed by the properties of the molecule. The A coefficients are expressed as:

$$A_{21} = \frac{16\pi\Delta\nu_{21}^3}{3\epsilon_0 hc^3}|\mu|^2 \quad [\mathrm{s}^{-1}] \qquad (2.25)$$

where $\Delta\nu_{21}$ is the frequency difference between the two states, ϵ_0 is the permittivity of free space ($8.85\times10^{-12}\,\mathrm{F\,m^{-1}}$) and $|\mu|^2$ is the mean magnetic dipole moment of the

molecule. Dipole moments are typically measured in Debye, or, Coulomb-meters in SI units (1 Debye $= 3.22 \times 10^{-30}\,\mathrm{C\,m}$).

These coefficients are not independent of each other. To demonstrate the relationship between the radiative coefficients (A and B) under the LTE approximation, consider n molecules in a radiation field, I_ν. The average energy density of photons is then $\bar{U} = 4\pi\bar{I}_\nu/c$. Einstein showed that for the system to be in a stationary state, the de-excitation transitions from upper to lower states are balanced by the excitation transitions from lower to upper states:

$$n_2 A_{21} + n_2 B_{21}\bar{U} = n_1 B_{12}\bar{U} \tag{2.26}$$

where n_i denotes the number of molecules in the i^{th} level with $n = \sum_i n_i$. Assuming the system is in thermal equilibrium or LTE, then the level populations are governed by the Boltzmann distribution:

$$\frac{n_2}{n_1} = \frac{g_2}{g_1}\exp\left(\frac{-\Delta E_{21}}{kT}\right) \tag{2.27}$$

where g_i denotes the statistical weight of the i^{th} state, ΔE_{21} is the energy difference between the two states and T is the temperature of the system. Rearranging Equation 2.26 and using Equation 2.27 yields the average radiation field:

$$\bar{U} = \frac{A_{21}}{\frac{g_1}{g_2}\exp\left(\frac{\Delta E_{21}}{kT}\right) B_{12} - B_{21}} \tag{2.28}$$

The radiation field for a system in LTE is also given by the Plank function, Equation 2.8, giving:

$$\bar{U} = \frac{4\pi}{c} B_\nu \tag{2.29}$$

$$= \frac{8\pi h\nu^3}{c^3}\frac{1}{\exp\left(\frac{\Delta E}{kT}\right) - 1} \tag{2.30}$$

Equating 2.28 and 2.30 can only jointly occur given two conditions:

$$A_{21} = \frac{8k\pi\nu^3}{c^3} B_{21} \tag{2.31}$$

$$g_1 B_{12} = g_2 B_{21} \tag{2.32}$$

Radiative processes are not the only form of interactions that molecules can have. Molecules can also be excited and de-excited via collisional processes. Like radiative processes, collisional processes can also be described by Einstein coefficients:

- **The Collisional De-Excitation Rate C_{21}:** The rate of collisions with another molecule resulting in a de-excitation transition from an upper state to a lower state (s^{-1}).
- **The Collisional Excitation Rate C_{12}:** The rate of collisions with another molecule resulting in an excitation transition from a lower state to an upper state (s^{-1}).

The C coefficients are proportional to the number density, n, of the material. In astrophysical situations, molecular hydrogen is the dominant molecular species and, as such, C coefficients are proportional to n_{H_2}. A critical density, n_c exists where the collisional de-excitation rate equals the spontaneous emission rate:

$$n_c = \frac{A_{21}}{\langle \sigma v \rangle} \approx A_{21} \times 10^{10} \quad [\mathrm{cm}^{-3}] \tag{2.33}$$

where σ is the interaction cross section ($\sigma \sim 10^{-15}\,\mathrm{cm}^2$), and v is the thermal velocity of the particles ($v = \sqrt{3\,k\,T/m} \sim 10^5\,\mathrm{cm\,s}^{-1}$) and $\langle \sigma v \rangle$ refers to their average values. The critical density is the cut-off point for radiative detections. For densities below n_c, collisional excitation will be too infrequent to produce a significant population inversion to allow for any detectable signal over the background radiation field. This also shows that higher frequency transitions will trace increasingly dense material as $A_{21} \propto \nu^3$ by Equation 2.25. The critical densities of the molecules used in this thesis are presented in Table 2.1.

2.4 Typical Molecular Species Used to Study Molecular Clouds

As discussed in § 1.2, the interstellar medium consists of $\sim 90\%$ hydrogen existing in both atomic and molecular form. Molecular hydrogen, H_2, is the dominant constituent of molecular gas and molecular clouds (MC). However, H_2 only emits ultraviolet radiation which is absorbed quickly by the surrounding environment. This means that H_2 cannot be measured directly. Fortunately, the second most abundant molecule, carbon monoxide, CO, is found in the same regions as H_2, with a typical CO:H_2 abundance ratio, relating one molecular species to another, the order of $\sim 10^{-5}$. In this way, it is

common practice to use CO as tracer of H_2. In fact, this is what is done in Figure 1.3, the CO (1-0) emission is measured and used to infer the H_2 distribution throughout the Galaxy.

To determine the H_2 distribution using CO as a surrogate tracer is not a perfect solution. CO emission rapidly becomes optically thick towards MCs. This means that CO observations cannot fully penetrate the cloud and observe the dense interiors. That is, CO observations do not trace the entire MC. To observe the dense regions inside the MCs, tracers with lower abundances are needed. For this reason ammonia, NH_3, (discussed in detail later in § 2.6) and carbon monosulphide, CS, are typically used. These tracers have higher critical densities, $n \sim 10^3 - 10^4\,\mathrm{cm}^{-3}$, so they trace the dense portions of MCs. Additionally, nitrogen bearing molecular species tend to survive longer in the gas phase (and can emit radiation) in the colder regions of clouds (Tafalla *et al.*, 2002) before suffering 'freezing-out' depletion onto dust grains like CO and CS (Tafalla *et al.*, 2002; Bergin *et al.*, 2006). Additional molecular species are used to trace specific physical conditions. The silicon monoxide molecule, SiO, is a known and proven signpost for shocked and disrupted gas (Schilke *et al.*, 1997; Martin-Pintado *et al.*, 2000; Gusdorf *et al.*, 2008a,b). Typically silicon has a low gas phase molecular abundance as it is contained within dust grains. However, in shocked and/or disrupted regions the gas-phase silicon abundance is enhanced through dust grain sputtering and dissociation, allowing silicon bearing molecules to form. This makes SiO an ideal tracer for post shocked and/or disrupted regions. Long carbon chain molecules, the cyanopolyynes HC_nN ($n = 3, 5, 7\ldots$) and methanol masers, CH_3OH indicate hot gas-phase chemistry and are typically found towards sites of stellar activity (van Dishoeck & Blake, 1998). Table 2.1 presents some of the molecular lines typically used in MC studies, and those primarily used in this thesis.

2.5 Physical Gas Parameters from Observations

Detecting the discrete radiation from different molecules allows the optical depth of the emission to be calculated. From the optical depth, a line of sight column density can be determined. The temperature of the source can also be estimated assuming an LTE approximation. The following sections outline the *general* analysis chain that is needed to obtain these parameters from molecular line observations.

Molecule Name	Symbol	Transition	Frequency [MHz]	Critical Density [cm^{-3}]
Carbon Monoxide	CO	(1-0)	115271.202	$\sim 7.2 \times 10^2$
		(2-1)	230538.000	$\sim 6.9 \times 10^3$
Ammonia	NH_3	(1,1)	23694.4709	$\sim 3.6 \times 10^3$
		(2,2)	23722.6336	$\sim 4.9 \times 10^3$
		(3,3)	23870.1269	$\sim 5.6 \times 10^3$
		(6,6)	25056.0250	$\sim 9.2 \times 10^3$
		(9,9)	27477.9430	$\sim 1.1 \times 10^4$
Carbon Monosulphide	CS	(1-0)	48990.957	$\sim 1.8 \times 10^4$
	$C^{34}S$		48206.946	$\sim 1.7 \times 10^4$
	^{13}CS		46247.580	$\sim 1.5 \times 10^4$
Silicon Monoxide	SiO	(1-0)	43423.864	$\sim 3.1 \times 10^4$

Table 2.1: A summary of some of the molecules typically used to study molecular clouds, and those primarily used in this thesis. The molecular name, molecular symbol, rotational transition, transition frequency, and approximate critical density of the transition are presented.

2.5.1 Optical Depth

The emission detected from any region in space can be expressed by the detection equation which is a function of optical depth. Typically, the optical depth effects on the emission are determined from multiple molecular transitions. The standard procedure is to detect tracers that are both optically thin, denoted by $\nu 1$, and optically thick, denoted by $\nu 2$, and, use an abundance ratio, R, to infer the optical depth, τ. This is, in theory, a very neat analysis method. Each of the molecular transitions will have detected emission in the form of Equation 2.21:

$$T_{\mathrm{A}}^{*}(\nu_1) = \left(T_{\mathrm{src}}(\nu_1) - T_{\mathrm{bkg}}(\nu_1)\right)\left(1 - \mathrm{e}^{-\tau_{\nu_1}}\right)$$
$$T_{\mathrm{A}}^{*}(\nu_2) = \left(T_{\mathrm{src}}(\nu_2) - T_{\mathrm{bkg}}(\nu_2)\right)\left(1 - \mathrm{e}^{-\tau_{\nu_2}}\right)$$

Using two molecular species with emission lines close in frequency ($\nu_1 \approx \nu_2$), so that the frequency dependent properties are similar and a ratio of the two detected intensities yields:

$$\frac{T_{\mathrm{A}}^{*}(\nu_1)}{T_{\mathrm{A}}^{*}(\nu_2)} = \frac{1 - \mathrm{e}^{-\tau_{\nu_1}}}{1 - \mathrm{e}^{-\tau_{\nu_2}}} = \frac{1 - \mathrm{e}^{-\tau/R}}{1 - \mathrm{e}^{-\tau}} \tag{2.34}$$

where the abundance ratio, R, between the two molecular species can be determined in a laboratory. Numerically solving Equation 2.34 gives the optical depth, τ. This method of determining the optical depth is applied in Chapter 4.

This method is by no means ideal. In practice, finding two simultaneously detectable molecules with similar frequencies, excitation temperatures and characteristics, and one them being optically thin, is challenging. Such molecular pairs do exist, for example molecular isotopologues[3], but other issues related to instrumentation need to be considered. Until recently, observations of multiple frequencies could not be performed simultaneously. Observations were often spread over several sessions with different atmospheric conditions. Additionally, as a result of the large frequency differences between molecular transitions, observations frequently need to be performed on separate telescopes. This introduces a series of additional corrections which need to be applied, such as, telescope efficiencies, filling factors, beam shapes and beam sizes. Unfortunately, few (if any) of these aforementioned parameters are precisely known. This makes applying all the necessary corrections difficult. However, it is possible to proceed by making some suitable approximations. A more robust determination of the optical depth is presented in § 2.6.3.

2.5.2 Column Density

Determining the column density of a molecular transition, begins with the definition of the absorption coefficient, α_ν, in terms of the collisional Einstein coefficients:

$$\alpha_\nu = \frac{h\nu}{k}\left(n_1 B_{12} - n_2 B_{21}\right)\phi(\nu) \tag{2.35}$$

where $\phi(\nu)$ is the normalised Gaussian line profile. Using the relationship between the Einstein coefficients from Equation 2.32 gives:

$$\alpha_\nu = \frac{c^2}{8\pi\nu^2} A_{21}\left(n_1\frac{g_2}{g_1} - n_2\right)\phi(\nu) \tag{2.36}$$

Integrating along the path length, ds, (Figure 2.1) yields the optical depth, τ, such that:

[3]Isotopologues are the molecular equivalent of atomic isotopes (e.g. ^{12}C and ^{13}C are carbon isotopes), that is, molecules that contain isotopes (e.g. ^{12}CO and ^{13}CO are carbon monoxide isotopologues)

$$\tau = \int \alpha_\nu \, ds = \int \frac{c^2}{8\pi\nu^2} \, A_{21} \, (n_1 \, \frac{g_2}{g_1} - n_2) \, \phi(\nu) \, ds$$
$$= \frac{c^2}{8\pi\nu^2} \, A_{21} \, N_2 \left[\exp\left(\frac{\Delta E_{21}}{kT} \right) - 1 \right] \phi(\nu) \tag{2.37}$$

Here, a substitution of the Boltzmann equation, Equation 2.27, for g_2/g_1 has been used and N_2 is the upper state column density, given by $N_2 = \int n_2 \, ds$.

In the absence of background radiation, multiplying the detection equation, Equation 2.21, by τ_ν/τ_ν gives:

$$T_{\rm A}^* = T_{\rm src}(\nu) \left(\frac{1 - {\rm e}^{-\tau_\nu}}{\tau_\nu} \right) \tau_\nu \tag{2.38}$$

The emission from a source at brightness temperature $T_{\rm src}$ is related to a black body brightness temperature by:

$$T_{\rm src}(\nu) \equiv \frac{h\nu}{k} \left[\exp\left(\frac{h\nu}{kT_{\rm src}} \right) \right]^{-1} \tag{2.39}$$

Combining Equation 2.37, Equation 2.38 and Equation2.39 gives:

$$T_{\rm A}^* = \frac{h\nu}{k} \left[\exp\left(\frac{h\nu}{kT_{\rm src}} \right) - 1 \right]^{-1} \left(\frac{1 - {\rm e}^{-\tau_\nu}}{\tau_\nu} \right) \left(\frac{c^2}{8\pi\nu^2} \, A_{21} \, N_2 \left[\exp\left(\frac{\Delta E_{21}}{kT_{\rm src}} \right) - 1 \right] \phi(\nu) \right)$$
$$= \frac{hc^2}{8k\pi\nu} \, A_{21} \, N_2 \left(\frac{1 - {\rm e}^{-\tau_\nu}}{\tau_\nu} \right) \phi(\nu) \tag{2.40}$$

Integrating over the full width of the line results in:

$$\int_{-\infty}^{\infty} T_{\rm A}^* \, d\nu = \frac{hc^2}{8k\pi\nu} \, A_{21} \, N_2 \left(\frac{1 - {\rm e}^{-\tau_\nu}}{\tau_\nu} \right) \int_{-\infty}^{\infty} \phi(\nu) \, d\nu \tag{2.41}$$

where $\displaystyle\int_{-\infty}^{\infty} \phi(\nu) \, d\nu = 1$. Rearranging Equation 2.41 gives a general equation to find the column density of molecules in an upper state:

$$N_2 = \frac{8k\pi\nu^2}{A_{21}hc^3} \int_{-\infty}^{\infty} T_{\rm A}^* \, dv \left(\frac{\tau_\nu}{1 - {\rm e}^{-\tau_\nu}} \right) \quad [{\rm cm}^{-2}] \tag{2.42}$$

A substitution $\displaystyle\int_{-\infty}^{\infty} T_{\rm A}^* \, d\nu = \frac{v}{c} \int_{-\infty}^{\infty} T_{\rm A}^* \, dv$ is made to use the integrated intensity of the spectral line in $\rm K\,km\,s^{-1}$ units. This method of determining the upper state column density is applied in Chapter 4. The reason for the switch between frequency (ν)

and velocity (v) is for convenience. Molecular line emission is emitted with discrete frequencies. Due to Galactic rotation, these frequencies are Doppler-shifted when they are detected at Earth. Modern telescope systems data reduction packages (discussed later in § 3.2) will display the results of observations in a three dimensional data-cube, where the third dimensional information is in Doppler-shifted $\mathrm{km\,s^{-1}}$ units.

2.5.3 Temperature from the LTE Approximation

As outlined in § 2.3.1, under the LTE approximation, the populations of molecules in particular states are governed by the Boltzmann distribution. Thus, by determining the ratio of molecular species in two different levels, the temperature of the system can be estimated. A rearrangement of the Boltzmann distribution, Equation 2.27, gives:

$$T_{\mathrm{rot}} = \frac{-\Delta E_{21}}{k} \left[\ln \left(\frac{N_{2,2}}{N_{2,1}} \frac{g_1}{g_2} \right) \right]^{-1} \quad [\mathrm{K}] \tag{2.43}$$

where T_{rot} is the rotational temperature, $N_{2,2}$ is the upper state column density of transition 2, $N_{2,1}$ is the upper state column density of transition 1. Under this construction, four different molecular transitions need to be observed. For example, using the CS (1-0), $C^{34}S$ (1-0), CS (2-1) and $C^{34}S$ (2-1) transitions, the temperature of the system can be determined. This set of transitions allows the CS (1-0) optical depth to be estimated, as described in § 2.5.1, then the CS (1-0) column density can be determined via the method described in § 2.5.2. Similarly, the CS (2-1) optical depth and CS (2-1) column density can be found. By putting these column densities into Equation 2.43 the rotational temperature of the system can be obtained.

Again, this situation is not ideal. It requires compounding assumptions and correction factors as outlined in § 2.5.1. The LTE approximation has become standard for molecular line observations as, for many situations, nothing better can be done. However, by using reasonable assumptions and understanding the telescope's properties, these sources of error can be minimised. A more elegant solution exists to eliminate many of these sources of error, namely, use the ammonia molecule.

2.6 The Ammonia Molecule

This section discusses the ammonia molecule, NH_3, and its typical molecular line spectrum. It outlines the properties which make it such a valuable molecule for astrophysical observations. Finally, the NH_3 specific methodology for obtaining the optical depth, column density and temperatures is discussed.

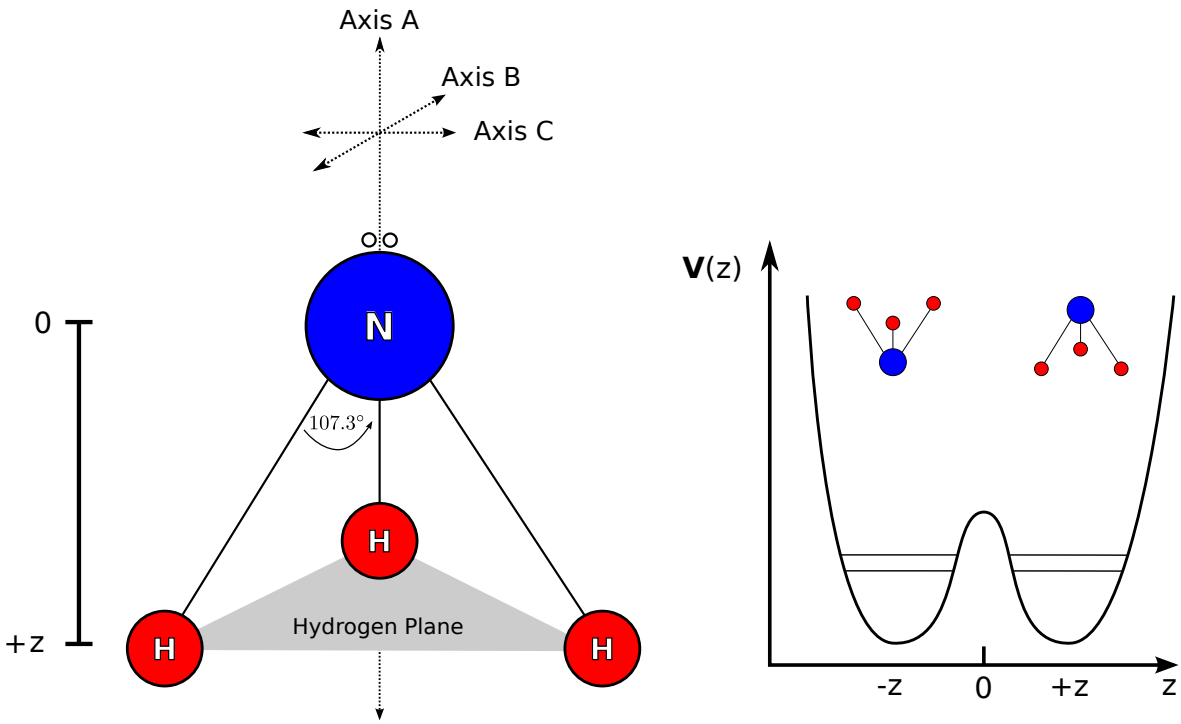

Figure 2.2: Left: A schematic of the ammonia molecule showing the arrangement of the atoms. The three principal axes of rotation are indicated. Axis A is the symmetry axis. The hydrogen plane is also indicated. The side scale bar indicates the distance, z, between the nitrogen atom and the hydrogen plane. **Right:** The double well potential the ammonia molecule 'tunnels' through in an inversion transition. The horizontal axis is the distance, z, between the nitrogen atom and the hydrogen plane. The vertical axis is the potential as a function of distance z. The central hump at z=0 is from the Coulomb force of the hydrogen plane.

2.6.1 Introduction to the NH_3 Molecule

The ammonia molecule, NH_3, is a trigonal pyramid molecule. It consists of one nitrogen atom bonded with three hydrogen atoms, which form an equilateral triangular plane. The nitrogen atom contains five valence shell electrons, requiring one electron from each hydrogen atom to complete its octet of electrons. This configuration leads to a free electron pair which remain unbonded and adds a small compression force to the hydrogen atoms. This slightly compresses the hydrogen bond angle to 107.3°. The basic structure of the ammonia molecule is shown in Figure 2.2.

NH_3 was the first poly-atomic molecule detected in interstellar space. Since its discovery by Cheung *et al.* (1968), it has become a powerful spectroscopic tool to probe the interstellar medium (ISM). NH_3 displays a large number of transitions, tracing a wide range of excitation conditions. This permits NH_3 to be detected in many regions, from infrared dark clouds (Ungerechts *et al.*, 1980), both low and high luminosity star forming regions (e.g. Ho & Barrett 1980; Ho *et al.* 1981) and external galaxies (Martin

& Ho, 1979).

Many NH_3 inversion transitions (see Figure 2.2 and § 2.6.2) are seen over a narrow bandwidth. This property is what makes NH_3 observations so advantageous. A single receiver at 23-25 GHz can detect multiple inversion transitions simultaneously. This allows the temperature to be unambiguously constrained. It is for this reason that NH_3 is sometimes referred to as a molecular thermometer.

NH_3 traces dense gas. It has a critical density $n \sim 3.6 \times 10^3\,\mathrm{cm}^{-3}$ (Table 2.1) and a wide range of excitation temperatures, T_{ex}. This T_{ex} range allows NH_3 to trace molecular material in cold, quiescent regions, as well as violent and extreme regions in space.

2.6.2 The Ammonia Spectrum

In classical mechanics, the kinetic energy of a three dimensional rotor is found from:

$$E_{\mathrm{rot}} = \frac{J_A^2}{2I_A} + \frac{J_B^2}{2I_B} + \frac{J_C^2}{2I_C} \tag{2.44}$$

where E_{rot} is the rotational energy, I_A, I_B and I_C are the moments of inertia about the principal axes of rotation (labelled A, B and C) and J_A, J_B and J_C are the corresponding projections of the total angular momentum vector $\boldsymbol{J}$. The structure of the molecule, shown in Figure 2.2, has an axis of symmetry (Axis A). In the absence of external torques this is the main axis of rotation. The NH_3 molecule is a symmetric-top. Therefore, the other axes of rotation (Axes B and C), which are mutually perpendicular to the symmetry axis, have the same moments of inertia. This simplifies the rotation such that $I_B = I_C$ and $J_B = J_C$. The total angular momentum then becomes:

$$E_{\mathrm{rot}} = \frac{J^2}{2I_B} + J_A^2\left(\frac{1}{2I_A} - \frac{1}{2I_B}\right) \tag{2.45}$$

The eigenvalues for J^2 and J_A^2 are quantised with $J^2 = J(J+1)\hbar^2$ and $J_A^2 = K^2\hbar^2$ where J and K are integers. The rotational energy levels are given by:

$$E_{\mathrm{rot}} = B_c h J(J+1) + (A_c - B_c)hK^2 \tag{2.46}$$

In this way A_c and B_c are the rotational constants about axes A and B in units of wavenumber, cm^{-1}. We also define J and K as quantum numbers that measure the magnitude of the total angular momentum, and its component along the symmetry axis, respectively. For any given J, there are $2J+1$ possible values for K, and all levels of $K > 0$ are doubly degenerate. It is conventional to restrict $K \geq 0$ as states with $\pm K$ have the same energy. Therefore, the total set of rotational levels is arranged

into columns or 'ladders' of fixed K value. The rotational levels of NH_3 are indicated in Figure 2.3. Within any given K-ladder, the state of lowest energy has $J = K$. Downward transitions from (J, K) to $(J-1, K)$ occur very rapidly, with typical time scales of 10 to 100 s.

The NH_3 molecule only has an electric dipole moment along the symmetry axis. Classically, rotation about this axis cannot produce dipole radiation. Hence, the transition probability is zero. The quantum mechanical dipole transitions with $\Delta K \neq 0$ are also quantum mechanically *forbidden*[4]. This sets up the following transition selection rules:

$$\Delta J = 0 \pm 1 \ ; \ \Delta K = 0 \ ; \ \text{Parity} : + \leftrightarrow - \tag{2.47}$$

States with $J \geq K$ have rapid downward transitions, as such, these states are denoted as 'non-metastable'. In comparison, molecules in states with $J = K$ are referred to as 'metastable'. Further downward transitions would require $(J, J = K) \rightarrow (J', K')$, where $J' < J$ & $K' < K$. While it is possible for such transitions to occur, the time scale associated is typically 10^9 s. Therefore, the molecule is more likely to stay in the $(J, J = K)$ state. These properties give rise to the 'rotational backbone' of NH_3, along the lower border of Figure 2.3.

The spin of the hydrogen atom can take two values, either up or down. Therefore, two distinct species of NH_3 exist, ortho- and para- NH_3. Ortho-NH_3 has $K = 3n$, where n is an integer, and all hydrogen spins are parallel. Para-NH_3 has $K \neq 3n$, and all hydrogen spins are not parallel. Ortho-NH_3 also has twice the statistical weight of para-NH_3. Under normal radiative and collisional conditions, spin orientations remain unchanged. Thus, transitions between the ortho- and para-NH_3 states are *forbidden*.

Inversion Transition

The potential energy distribution of the NH_3 molecule is described as a double well or a 'mexican-hat' potential. This potential is shown in Figure 2.2. The central barrier results from the Coulomb force of the hydrogen atoms. Typically the nitrogen molecule sits outside the hydrogen plane. Classically, it is prevented from passing through the hydrogen plane for low J values. However, due to its quantum wave nature, the particle's wavefunction can tunnel through the barrier after some time. This gives rise to two states, differentiated by parity, as presented in Equation 2.47. The two different states are pictured in Figure 2.2. In the left well, of 'negative' parity, the nitrogen

[4]Here *forbidden* refers to the quantum mechanical meaning of forbidden, which means "highly unlikely given that there is a more favoured transition".

Figure 2.3: The energy levels of NH_3. Each vertical column represents the individual K 'ladders' where vertical downward transitions occur rapidly. The allowed transitions for the $K = 1$ ladder are indicated by the vertical arrows. Similar arrows for the other K ladders are omitted. The rotational backbone of NH_3 is indicated by states in blue. Image adapted from Ho & Townes (1983)

sits below the hydrogen plane and in the right well, of 'positive' parity, the nitrogen sits above the hydrogen plane. This 'inversion' transition is technically a vibrational transition which would normally emit in the infra-red band. However, the energy is dampened during the tunnelling process. This results in microwave emission in the 12 mm (23 GHz) band, which is commonly used.

Quadrupole Splitting

The non-spherical charge distribution of the nitrogen atom sets up an electric quadrupole moment. This quadrupole moment interacts with the electric field of the electrons and produces quadrupole splitting of the inversion spectra. This allows the NH_3 molecule to be torqued in the presence of the electric field gradient. Consequently, the inversion state is split into states characterised by the following selection rules:

$$\Delta F = 0, \pm 1 \ ; \ \Delta J = 0, \pm 1 \ ; \ \Delta I = 0 \tag{2.48}$$

where $I = 1$ is the nuclear spin of the nitrogen and F is the total angular momentum including the nuclear spin. Each inversion is split into three components, giving rise to the characteristic five-fingered ammonia spectrum pictured in Figure 2.4. The central or main group of lines has $\Delta F = 0$, the two inner and outer satellite line groups have $\Delta F = \pm 1$. Both sets of satellite line groups are symmetric about the main group. The relative intensities of the main, inner and outer satellite groups are calculated via:

$$F \rightarrow F : \frac{A[(J(J+1) + F(F+1) - I(I+1)]^2(2F+1)}{F(F+1)} \tag{2.49}$$

$$F \rightarrow F+1 : -\frac{A(J+F+I+2)(J+F-I+1)(J-F+I)(J-F-I-1)}{F+1} \tag{2.50}$$

$$F \rightarrow F-1 : -\frac{A(J+F+I+1)(J+F-I)(J-F+I+1)(J-F-I)}{F} \tag{2.51}$$

The relative intensities have been calculated for the NH_3 (1,1), (2,2) and (3,3) inversion transitions and are displayed in Table 2.2. It is shown from Table 2.2 that for the NH_3 (1,1) inversion transition, roughly 50% of the signal is in the main group, and 50% of the signal is in the satellite groups. For the higher (J,K) inversion transitions, most of the signal is contained within the main line and the relative intensity of the hyperfine lines become weaker, e.g. NH_3 (2,2) has $\sim 80\%$ in the main line and $\sim 20\%$ in satellite lines, NH_3 (3,3) has $\sim 90\%$ in the main and only $\sim 10\%$ in satellite lines.

Magnetic Hyperfine Splitting

Both the nitrogen and hydrogen atoms have magnetic moments which interact. The coupling of the nuclear spin and angular momentum, as well as, the spin-spin interactions (between the hydrogen-nitrogen and hydrogen-hydrogen atoms), introduce further splitting on the order of 40 kHz into the spectrum. This has the net result of splitting the the NH_3 (1,1) spectrum into a total of 18 distinct hyperfine components. The resolution required to resolve all 18 hyperfine lines is beyond the limitations of the data used in this thesis, however, Figure 2.4 shows the full energy level diagram for the NH_3 (1,1) inversion transition. The data used in this thesis is capable of resolving the quadrupole splitting as indicated in Figure 2.4.

2.6.3 Physical Gas Parameters from Ammonia Observations

The properties of NH_3 mentioned in § 2.6.2 allow for an alternate approach to determine the physical parameters of optical depth, column density and temperature in a

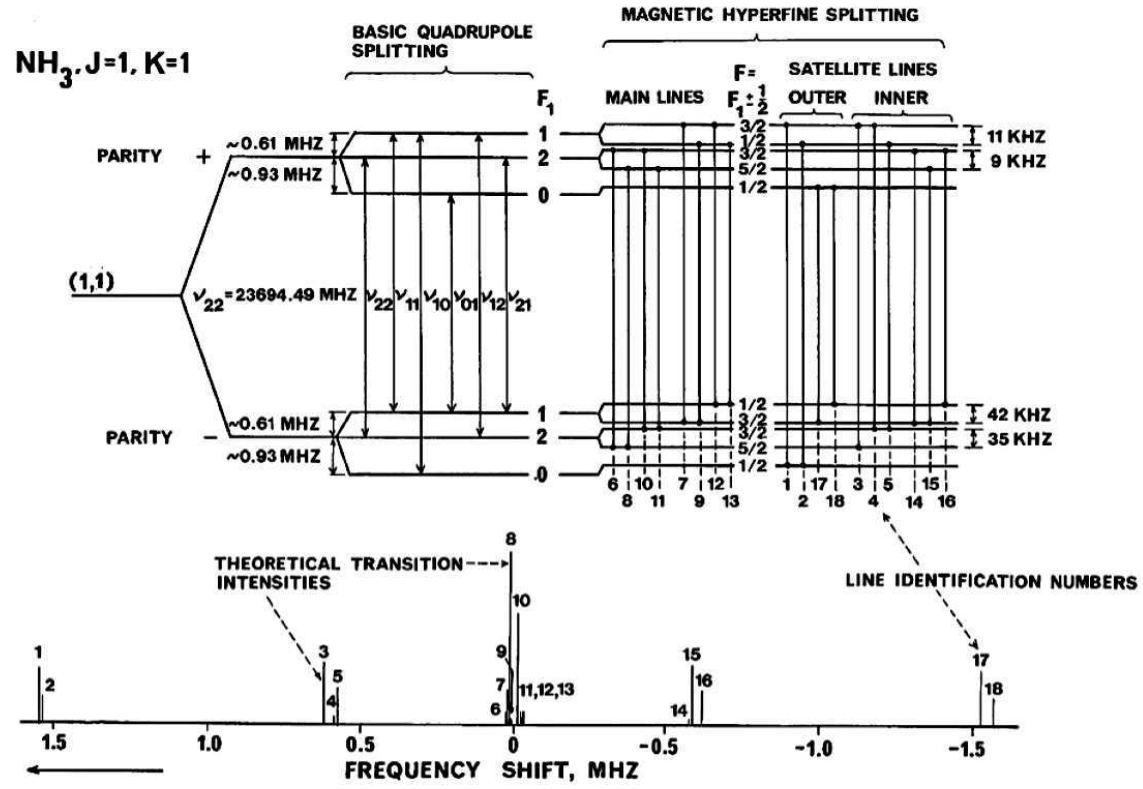

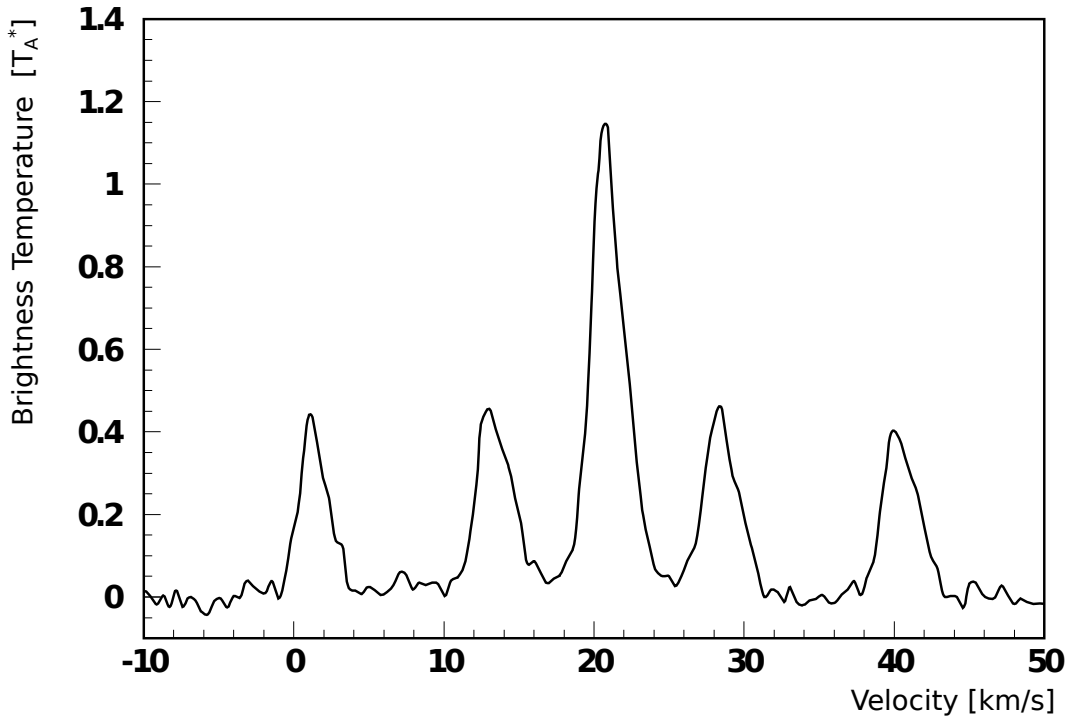

Figure 2.4: **Top:** A schematic showing the full energy level diagram and hyperfine structure for the NH_3 (1,1) inversion transition. Image from Rydbeck *et al.* (1977) **Bottom:** An example NH_3 (1,1) spectra from the Mopra telescope showing the distinct five-fingers of ammonia.

Inversion Transition	F Transition		Hyperfine Group	Relative Intensity
$(J,K)=(1,1)$		$F=0\rightarrow 0$	Main	0.0
	$\Delta F=0$	$F=1\rightarrow 1$	Main	0.0833
		$F=2\rightarrow 2$	Main	0.4166
	$\Delta F=+1$	$F=1\leftrightarrow 2$	Inner Satellite	0.1388
	$\Delta F=-1$	$F=1\leftrightarrow 0$	Outer Satellite	0.1111
$(J,K)=(2,2)$		$F=1\rightarrow 1$	Main	0.1500
	$\Delta F=0$	$F=2\rightarrow 2$	Main	0.2315
		$F=3\rightarrow 3$	Main	0.4148
	$\Delta F=+1$	$F=2\leftrightarrow 3$	Inner Satellite	0.0518
	$\Delta F=-1$	$F=2\leftrightarrow 1$	Outer Satellite	0.0500
$(J,K)=(3,3)$		$F=2\rightarrow 2$	Main	0.2117
	$\Delta F=0$	$F=3\rightarrow 3$	Main	0.2802
		$F=4\rightarrow 4$	Main	0.4019
	$\Delta F=+1$	$F=3\leftrightarrow 4$	Inner Satellite	0.0268
	$\Delta F=-1$	$F=3\leftrightarrow 2$	Outer Satellite	0.0264

Table 2.2: The relative intensities of the NH_3 inversion transitions. The quadrupole hyperfine emission is caused by the interaction of the electric quadrupole moment of the nitrogen atom and the electric field of the electrons. The relative intensity of the satellite group for the NH_3 (1,1), (2,2) and (3,3) inversion transitions is normalised such that the total emission from all lines is unity. The relative intensity of the satellite groups are for a single satellite group and need to be doubled to get the total contribution from both sets.

molecular cloud. Two specific properties of NH_3 are exploited:

- **The hyperfine emission:** The benefit of hyperfine emission is that the relative intensities of the hyperfine components can be directly calculated based on the quantum nature of the molecule. This removes any elemental abundance ratios from the optical depth calculations.

- **The frequency difference between the NH_3 (1,1) and NH_3 (2,2) inversion transitions:** With such a small frequency difference between the NH_3 (1,1) and NH_3 (2,2) inversion transitions, $\Delta\nu \approx 28\,\mathrm{MHz}$, a single telescope can simultaneously detect both transitions. This means all the telescope properties and weather conditions will affect both lines in very much the same way.

The following sections outline the NH_3 specific derivation methodology to obtain the optical depth, rotational temperature, kinetic temperature and column density. This methodology of determining gas parameters has been applied in § 3.4 and Chapter 5.

Optical Depth

To determine the optical depth, one must solve (analogous to Equation 2.34):

$$\frac{\Delta T_{\rm A}^*(J,K,m)}{\Delta T_{\rm A}^*(J,K,s)} = \frac{1-{\rm e}^{-\tau(J,K,m)}}{1-{\rm e}^{-\alpha\tau(J,K,m)}} \tag{2.52}$$

where $T_{\rm A}^*$ is the observed brightness temperature with m and s referring to the main and satellite hyperfine components. $\tau(J,K,m)$ is the optical depth of the main component. α is the ratio of the satellite intensity compared to the main component intensity and can be calculated directly from Table 2.2 ($\alpha = 0.28$ or 0.22 for the inner and outer satellites for the NH_3 (1,1) line respectively). Equation 2.52 can be numerically solved for $\tau(J,K,m)$.

The total optical depth of the transition may then be found by accounting for the fraction in the main component:

$$\tau(J,K,t) = \frac{\tau(J,K,m)}{f_{J,K,m}} \tag{2.53}$$

where $f_{J,K,m}$ is the fraction of intensity contained in the main line (Table 2.2). This method is applicable to any (J,K) inversion transition, however, it is much harder to observe the satellite line emission for high (J,K) inversion transitions (as indicated by the relative intensities of the satellite line groups in Table 2.2). Typically, it is far easier to calculate the optical depth of the NH_3 (1,1) transition and then infer the optical depth of the higher transitions via:

$$\tau(J,K,t) = -\frac{1}{f_{J,K,m}} \ln\left[1 - \frac{\Delta T_{\rm A}^*(J,K,m)}{\Delta T_{\rm A}^*(1,1,m)}\left(1-{\rm e}^{-\tau(1,1,m)}\right)\left(\frac{X_{1,1}}{X_{J,K}}\right)\right] \tag{2.54}$$

where $T_{\rm A}^*$ $(1,1,m)$ is the peak temperature of the main component and $f_{J,K,m}$ is the fraction of intensity contained in the main line of the (J,K) inversion transition. Under the assumption that both the (J,K) and (1,1) lines arise from the same gas, they will have the same excitation temperature. This means $X_{1,1}/X_{J,K} \approx 1$ as

$$X_{J,K} \sim \frac{1}{2}\frac{h\nu}{kT_{\rm ex}} \tag{2.55}$$

From herein $\tau(J,K,t)$ is written as $\tau_{J,K}^{\rm tot}$.

Column Density

The column density of the NH_3 (J, K) inversion transitions are found via Equation 2.42. For the NH_3 (1,1) inversion the column density is:

$$N_{1,1} = \frac{8k\pi\nu_{1,1}^2}{A_{1,1}hc^3} \int_{-\infty}^{\infty} T_{\rm A}^* \, dv \left(\frac{\tau_{1,1}^{\rm tot}}{1 - {\rm e}^{-\tau_{1,1}^{\rm tot}}} \right) \quad [{\rm cm}^{-2}] \tag{2.56}$$

and similarly for the NH_3 (2,2) transition:

$$N_{2,2} = \frac{8k\pi\nu_{2,2}^2}{A_{2,2}hc^3} \int_{-\infty}^{\infty} T_{\rm A}^* \, dv \left(\frac{\tau_{2,2}^{\rm tot}}{1 - {\rm e}^{-\tau_{2,2}^{\rm tot}}} \right) \quad [{\rm cm}^{-2}] \tag{2.57}$$

Rotational and Kinetic Temperature

The rotational temperature of the gas can be determined from Equation 2.43 with a detection of both NH_3 (1,1) and NH_3 (2,2). That is:

$$T_{\rm rot} = \frac{-\Delta E_{1,1-2,2}}{k} \left[\ln \left(\frac{N_{2,2}}{N_{1,1}} \frac{g_{1,1}}{g_{2,2}} \right) \right]^{-1} \quad [{\rm K}] \tag{2.58}$$

The energy difference between the NH_3 (2,2) and NH_3 (1,1) states is $\Delta E_{1,1-2,2} = 41\,{\rm K}$, and the degeneracy terms are $g = 2J + 1$. Thus, $g_{1,1} = 3$ and $g_{2,2} = 5$. Substituting in these values yields an equation for the rotational temperature:

$$T_{\rm rot} = -41 \left[\ln \left(\frac{3}{5} \frac{N_{2,2}}{N_{1,1}} \right) \right]^{-1} \quad [{\rm K}] \tag{2.59}$$

In general, the rotational temperature, $T_{\rm rot}$, is an underestimate of the kinetic temperature, $T_{\rm kin}$. For temperatures, $> 50\,{\rm K}$, one can estimate the kinetic temperature via the Einstein collisional coefficients (C) between the NH_3 (1,1), (2,2) and (2,1) states. Although this method is valid, the conversion between $T_{\rm rot}$ and $T_{\rm kin}$ is a non-linear equation and relies on the collision coefficients calculated at broad temperature intervals. Fortunately, an expression to estimate $T_{\rm kin}$ from $T_{\rm rot}$ has been developed by Tafalla *et al.* (2004):

$$T_{\rm kin} = T_{\rm rot} \left(1 - \frac{T_{\rm rot}}{42} \ln \left[1 + 1.1 \exp \left(\frac{-16}{T_{\rm rot}} \right) \right] \right)^{-1} \quad [{\rm K}] \tag{2.60}$$

This equation has been developed via Monte Carlo simulations and is believed to reproduce $T_{\rm kin}$ to better than 5% in the low temperature range (5 – 20 K). The advantage of this method is that it provides an accurate estimate for the kinetic temperature via easy-to-measure observable parameters.

Total Column Density

Equation 2.56 finds the column density of the molecules in the NH_3 (1,1) inversion state, not the total number of NH_3 molecules. Assuming all the NH_3 molecules are at the same temperature, the total column density of NH_3 molecules in all states can be determined via the Boltzmann equation and the partition function $Q(T)$ as in Equation 2.24. That is:

$$N^{\rm tot}[{\rm NH_3}] = \frac{N_{1,1}}{g_{1,1}} Q(T_{\rm kin}) \quad [{\rm cm^{-2}}] \tag{2.61}$$

Expanding the partition function gives the total column density:

$$N^{\rm tot}[{\rm NH_3}] = N_{1,1} \left[\frac{1}{3} \, {\rm e}^{E_{1,1-0,0}/T_{\rm kin}} + 1 + \frac{5}{3} \, {\rm e}^{E_{1,1-2,2}/T_{\rm kin}} + \frac{14}{3} \, {\rm e}^{E_{1,1-3,3}/T_{\rm kin}} + \ldots \right] \tag{2.62}$$

$$= N_{1,1} \left[\frac{1}{3} \, {\rm e}^{+23.26/T_{\rm kin}} + 1 + \frac{5}{3} \, {\rm e}^{-41.18/T_{\rm kin}} + \frac{14}{3} \, {\rm e}^{-100.25/T_{\rm kin}} + \ldots \right] \tag{2.63}$$

Total Molecular Hydrogen Mass and Density

As mentioned earlier in § 2.4, molecular hydrogen, H_2, is the dominant molecular species yet it cannot be measured directly. In order to determine the column density of molecular hydrogen, an abundance ratio, χ, is used to convert between the column density of a molecular species and molecular hydrogen. For the case of NH_3 emission:

$$N[{\rm H_2}] = \frac{N[{\rm NH_3}]}{\chi_{\rm NH_3}} \quad [{\rm cm^{-2}}] \tag{2.64}$$

In this thesis, the NH_3 to H_2 abundance ratio of $\chi_{\rm NH_3} = 2 \times 10^{-8}$ (Stahler & Palla, 2005) is used. Once the H_2 column density has been inferred, it can be converted into a physical mass by determining the physical area, A, of the emitting region. Usually a spherical core is assumed for the emission, which has area $A = \pi \, r^2$, and the total H_2 mass is:

$$M[{\rm H_2}] = 2 \, \pi \left(\frac{m_{\rm H}}{\rm kg} \right) \left(\frac{r}{\rm cm} \right)^2 \left(\frac{N[{\rm H_2}]}{\rm cm^{-2}} \right) \left(\frac{\rm M_\odot}{\rm kg} \right)^{-1} \quad [{\rm M_\odot}] \tag{2.65}$$

where $m_{\rm H}$ is the proton mass ($m_{\rm H} = 1.672 \times 10^{-27}\,{\rm kg}$) and r is the radius of the emitting core. Similarly, the total molecular H_2 number density can be determined by determining the volume, V, of the emitting region. Once again, this is usually assumed to be spherical, $V = \frac{4}{3}\pi r^3$, and the H_2 number density, $n_{\rm H_2}$, is:

$$n_{\mathrm{H_2}} = \left(\frac{M}{\mathrm{kg}}\right) \left[\frac{8\,\pi}{3} \left(\frac{m_{\mathrm{H}}}{\mathrm{kg}}\right) \left(\frac{r}{\mathrm{cm}}\right)^3\right]^{-1} \quad [\mathrm{cm}^{-3}] \tag{2.66}$$

CHAPTER III

12 mm Molecular Line Observations Toward the TeV γ-Ray Sources in the SNR W28 Field

This chapter (and chapters 4 and 5) summarise the results of millimetre wavelength molecular-line studies towards the W28 supernova remnant. The body of this chapter is presented as a refereed journal article. Additional details not suitable for journal publication are also presented, including an outline of the properties of the Mopra telescope and the calibration and reduction of Mopra data. This chapter also includes a brief summary of the other telescopes which have contributed data to this thesis.

3.1 The Mopra Telescope

The Mopra millimetre wave telescope is a 22 m single dish telescope. It is part of the Australia Telescope National Facility (ATNF) and operated by the Commonwealth Scientific and Industrial Research Organisation (CSIRO): Astronomy and Space Science division (CASS). The telescope resides 26 km outside the town of Coonabarabaran in northern New South Wales, Australia. Its exact latitude and longitude co-ordinates are 31° 16′ 04″ south, 149° 05′ 59″ east, at an elevation of 850 m above sea level.

3.1.1 Mopra Construction

Construction of the telescope was completed in late 1991 and was in operation within a week as a VLBI station (Tingay *et al.*, 1998). The system is of Cassegrain design, where the 22 m dish is a pseudo-parabolic reflector beneath a 4 m hyperbolic secondary reflector. Mopra is designed to maximise the gain for single feed receivers. A wireframe schematic and a photograph of Mopra can be seen in Figure 3.1. The dish, receiver cabin and supports are mounted on an A-frame, allowing the telescope to point from

NOTE:
This figure is included on page 52 of the print copy of the thesis held in the University of Adelaide Library.

Figure 3.1: Left: A wireframe schematic of the 22 m Mopra telescope showing the A-frame mount and cassegrain design. Image from Purcell (2006). **Right:** A photo of the Mopra telescope situated on the edge of the Warrumbungle Mountains in northern New South Wales, Australia. Image from the ATNF, `http://www.atnf.csiro.au/resources/imagebank/telescopes.html`

0° to 90° in elevation. The tracking system itself does not allow tracking through the zenith, resulting in a true elevation limit of 85°. The whole structure sits on a circular rail allowing rotation in azimuth from 0° to 360°.

3.1.2 The Mopra Spectrometer MOPS

In the late 1990s, a partnership between ATNF and the University of New South Wales was formed. Together they upgraded the dish and, in 2006, installed a new digital back-end, the Mopra Spectrometer (MOPS). MOPS is a broad band digital filter bank, consisting of four 2.2 GHz sub-bands which provide a total bandwidth of 8.3 GHz. MOPS allows two configurations, wideband mode and zoom mode. In wideband mode, MOPS provides continuous coverage over 8.3 GHz with 4 overlapping sub-bands. It provides 8096 channels in two linear polarisations (xx and yy). In zoom mode MOPS utilises up to 16 zoom bands, or 'windows' simultaneously. Each window is 137.5 MHz wide and has 4096 channels in each polarisation. A schematic showing the arrangement of the sub-bands and windows within the 8.3 GHz bandwidth can be seen in Figure 3.2

NOTE:
This figure is included on page 53 of the print copy of the thesis held in the University of Adelaide Library.

Figure 3.2: A schematic picturing the arrangement of the sub-bands and zoom bands within the two observing modes of MOPS. Image credit: ATNF.

Receiver	Wideband Mode		Zoom Mode	
	Bandwidth	Resolution	Bandwidth	Resolution
12 mm (22 GHz)	$112\,050\,\mathrm{km\,s^{-1}}$	$3.38\,\mathrm{km\,s^{-1}}$	$1\,863\,\mathrm{km\,s^{-1}}$	$0.41\,\mathrm{km\,s^{-1}}$
7 mm (44 GHz)	$56\,025\,\mathrm{km\,s^{-1}}$	$1.69\,\mathrm{km\,s^{-1}}$	$932\,\mathrm{km\,s^{-1}}$	$0.21\,\mathrm{km\,s^{-1}}$
3 mm (90 GHz)	$30\,378\,\mathrm{km\,s^{-1}}$	$0.915\,\mathrm{km\,s^{-1}}$	$505\,\mathrm{km\,s^{-1}}$	$0.11\,\mathrm{km\,s^{-1}}$

Table 3.1: Summary of the bandwidth and resolution properties of the three MOPS receivers in terms of the Doppler shifted V_{LSR} $\mathrm{km\,s^{-1}}$ units.

3.1.3 The Mopra Receivers

Mopra is equipped with three receivers[1]: a 3 mm receiver, covering the 76 – 117 GHz range; a 7 mm receiver, covering the 30 – 50 GHz range and a 12 mm receiver, covering the 16 – 27 GHz range. The three receivers are mounted on a single rotating and translating Dewar inside the receiver cabin. Switching between the 12 mm and 3 mm receivers requires only a rotation of the Dewar, while switching in and out of the 7 mm receiver requires a translation of the Dewar by approximately 10 cm, which can take several minutes. Properties for the different receivers are presented in Tables 3.1 and 3.2.

[1]Three millimetre wavelength receivers for single dish observations. An additional two receivers operating at centimetre wavelengths are reserved only for VLBI operation.

Band /Frequency	12 mm (16 – 27 GHz)	7 mm (30 – 50 GHz)	3 mm (76 – 117 GHz)	
Central Observing Frequency	24 GHz	42 GHz	90 GHz	115 GHz
Beamwidth (FWHM)	119″	82″	38″	30″
Average $T_{\rm SYS}$	∼70 K	∼80 K	∼200 K	∼600 K
Antenna Efficiency	∼0.6	∼0.6	∼0.5	∼0.4

Table 3.2: Summary of the parameters for the three MOPS receivers. The $T_{\rm SYS}$ is a measure of the total noise in the system (Equation 3.5).

3.1.4 Observing Modes

Mopra is capable of two different observing modes: position switching mode, which records a spectrum from a single position, and 'on-the-fly' mapping, which maps large portions of sky producing spectral line maps. The following paragraphs briefly outline each of these modes.

Position switching

Position switching observations involve alternately switching the telescope between a target source (ON) position and a reference (OFF) position. The OFF position spectrum is taken as a reference spectrum which, in off-line processing, is subtracted from the ON position. This subtraction is to remove any atmospheric and/or instrumental contributions, and produce a flat spectrum only containing emission from the source. Since the sky is dynamic and can vary on short time scales, the telescope performs several short observations ($\sim$ 2 min) which are averaged together to produce the final spectrum.

On-the-fly mapping

On-the-fly (OTF) mapping is used to make spectral line maps. In this mode, the telescope's beam is scanned along a line on the sky, dumping a spectrum every clock cycle (fixed at 2 sec). Each scan is slightly offset from the previous scan, by less than the beam full width at half maximum (FWHM). Following each scan, a single pointed observation is recorded at an OFF position several arc minutes away. This allows for sky continuum and atmospheric subtraction (ON – OFF) in off-line processing. The image is built up by combining multiple scans from different rows. Current scheduling limits the OTF mapping to be square regions of sky.

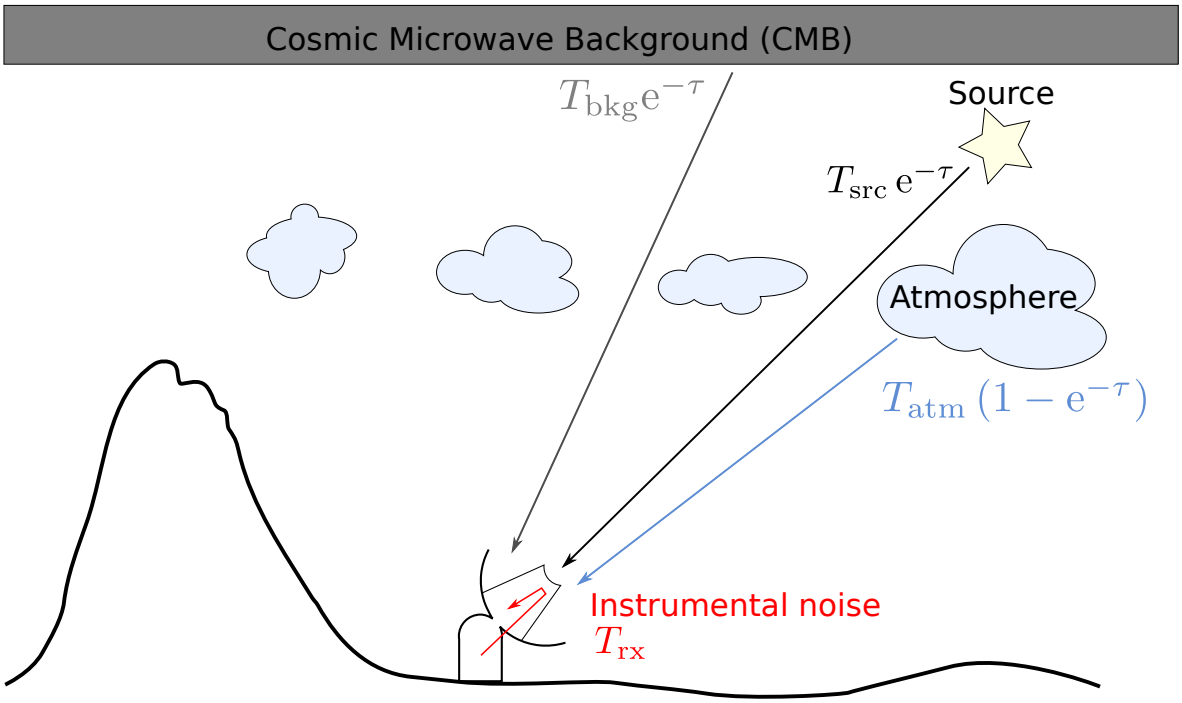

Figure 3.3: A graphical representation of the sources of radiation contributing to the total signal received by the telescope. The total measured power is a combination of: the CMB ($T_{\rm bg}$), the desired source ($T_{\rm src}$), the atmosphere ($T_{\rm atm}$) and the electronic noise in the receiver ($T_{\rm rx}$).

3.1.5 Calibration of Mopra Data

The dynamic atmosphere requires frequent bandpass calibration, especially at high frequencies. The following discussion applies to the ON/OFF observing modes used by the Mopra telescope. It assumes the detected emission is characterised by an effective source radiation temperature, T_b, related to a black body brightness temperature by Equation 2.39 repeated here:

$$T_b \equiv \frac{h\nu}{k}\left[\exp\left(\frac{h\nu}{kT_b}\right)-1\right]^{-1} \tag{3.1}$$

The raw signal received by the telescope is a combination of the source, atmospheric and background radiation, as well as instrumental noise from within the telescope itself. These sources of signal are pictured in Figure 3.3. The total power received when pointed ON source is characterised by:

$$P_{\rm ON} = C\left[T_{\rm src}\,e^{-\tau} + T_{\rm atm}(1-e^{-\tau}) + T_{\rm bg}\,e^{-\tau} + T_{\rm rx}\right] \tag{3.2}$$

When pointed OFF source:

$$P_{\rm OFF} = C\left[T_{\rm atm}(1-{\rm e}^{-\tau}) + T_{\rm bg}\,{\rm e}^{-\tau} + T_{\rm rx}\right] \tag{3.3}$$

where C is a constant to convert between brightness temperature and power, $T_{\rm atm}$ is the temperature of the atmosphere, $T_{\rm bg}$ is the temperature of the background radiation field and $T_{\rm rx}$ is the electronic noise temperature. The brightness temperature of the source is then:

$$T_{\rm src} = (P_{\rm ON} - P_{\rm OFF})\,\frac{{\rm e}^{\tau}}{C} \tag{3.4}$$

A convenient definition to use is the system temperature, $T_{\rm SYS}$, which defines the total noise in the system. Expressing the $T_{\rm SYS}$ as:

$$T_{\rm SYS} = P_{\rm OFF}\,\frac{{\rm e}^{\tau}}{C} = T_{\rm atm}({\rm e}^{\tau}-1) + T_{\rm bkg} + T_{\rm rx}\,{\rm e}^{\tau} \tag{3.5}$$

the brightness temperature of the source, Equation 3.4, becomes:

$$T_{\rm src} = \left(\frac{P_{\rm ON} - P_{\rm OFF}}{P_{\rm OFF}}\right) T_{\rm SYS} = T_{\rm A}^{*} \tag{3.6}$$

Introduced here is the antenna temperature, $T_{\rm A}^{*}$, which is the raw unit temperature recorded and output from MOPS. This antenna temperature is unique to the Mopra telescope. A general temperature scale is the main beam brightness temperature, $T_{\rm mb}$. The main beam brightness temperature is the calibrated temperature, after correcting for the main beam efficiency, of the telescope. This $T_{\rm mb}$ is the true source brightness temperature of a source which fills the main beam. Converting between $T_{\rm A}^{*}$ and $T_{\rm mb}$ is done by accounting for the antenna efficiency, $\eta_{\rm eff}$, such that $T_{\rm mb} = T_{\rm A}^{*}/\eta_{\rm eff}$. The main beam brightness temperature, $T_{\rm mb}$, is directly comparable with results from other (suitably corrected) telescopes. For the latest details on the characteristics of the Mopra beam and efficiencies see Urquhart *et al.* (2010).

3.2 Reducing Mopra Single Dish Data

The method of reducing Mopra single dish data depends on the type of observational data. Position switched data is reduced with the ATNF spectral line analysis package, `ASAP`, and OTF data is reduced with `Livedata` and `Gridzilla`. The following sections outline these data reduction packages and the steps required to reduce both position switched and on-the-fly mapping data.

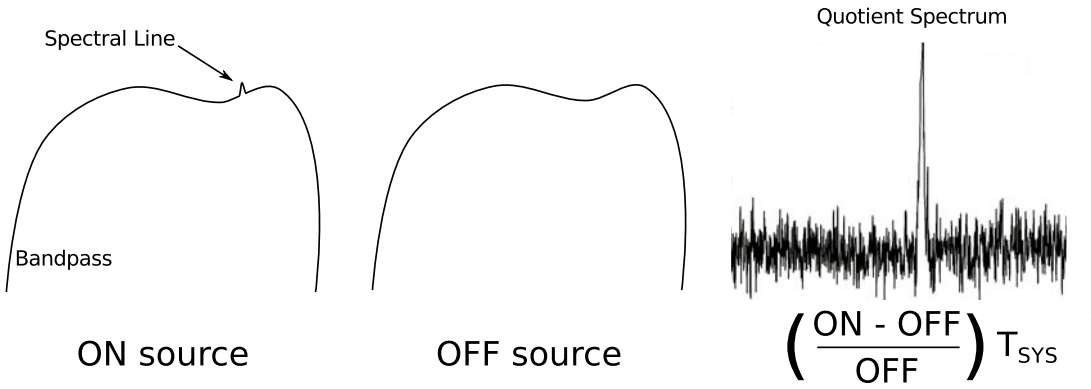

Figure 3.4: Graphical representation of the principles of ON/OFF observations. The ON source bandpass contains a spectral line while the OFF source bandpass does not. The quotient spectrum is formed as per Equation 3.6 to produce the final spectrum. This quotient spectrum is performed by both the `ASAP` and `Livedata` packages in off-line processing.

3.2.1 Reducing Position Switched Data

The ATNF spectral line analysis package, `ASAP`, is a command line based reduction package developed by the ATNF for the reduction of single dish data. The software can be run in the *ipython* interactive shell or in batch mode and is a combination of the *Python* and *C++* frameworks.

Ultimately, `ASAP` takes the raw telescope files, `.RPF`, and produces spectra. The general and most simplistic analysis chain required to reduce Mopra position switched data requires loading in the raw `.RPF` file, averaging the two polarisations, aligning the data in frequency and time, forming the quotient spectra (ON – OFF subtraction, Equation 3.6) and finally plotting the result. The result can be plotted as a function of the telescope channel number, frequency, or Doppler-shifted velocity (V_{LSR}). The method of forming the quotient spectra is shown graphically in Figure 3.4. All of these (and higher order) tasks are programmed into the software and simply need to be called in order to produce the output spectra.

3.2.2 Reducing On-The-Fly Mapping Data

The reduction of Mopra OTF mapping data is a multi-step process, requiring the use of several reduction packages. The first packages used are `Livedata` and `Gridzilla`. These packages are built on the *Glish* and *C++* frameworks, are GUI based (although can be run in batch mode) and are developed and maintained by Mark Calabretta at

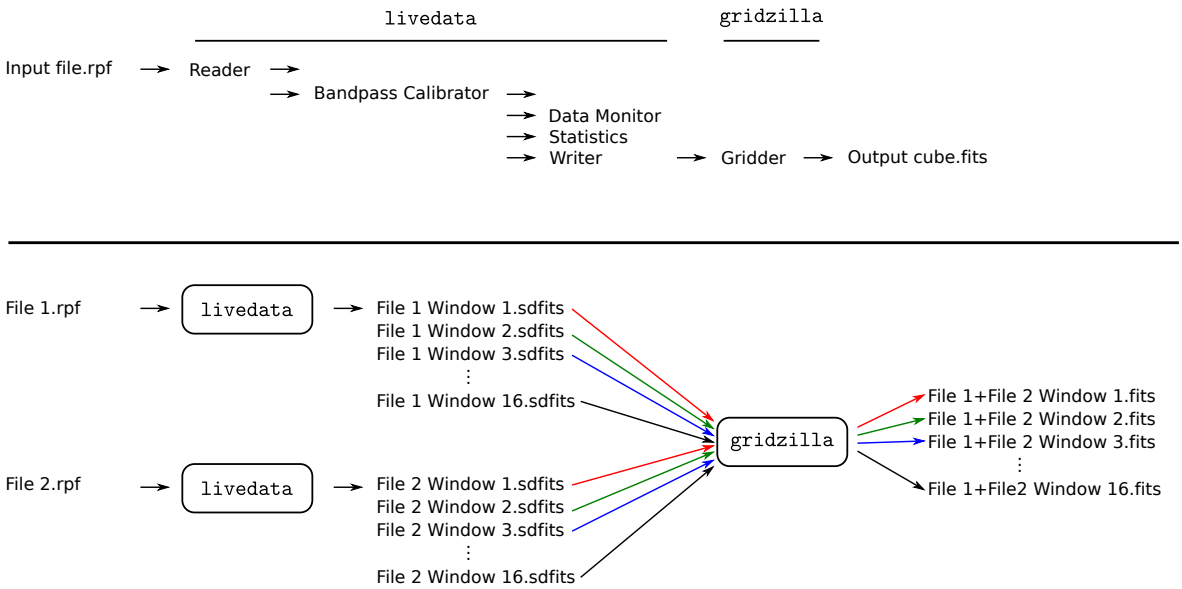

Figure 3.5: **Top:** The data flow pipeline for the `Livedata` and `Gridzilla` reduction of OTF Mopra data. Data flow is from left to right and any of the reduction clients may be skipped (except for the Reader). The final gridder stage is also provided as a stand alone package `Gridzilla`. **Bottom:** A flowchart indicating how two separate OTF observations, recorded in zoom mode, are reduced and combined. There is no limit to the number of different .RPF files that can be gridded together.

the ATNF[2]. Technically, both these packages are a part of the same analysis pipeline. However, the gridding component is released as a stand alone package (`Gridzilla`) so that it can be called with multiple pre-processed data-sets. The basic data flow for `Livedata` and `Gridzilla` is shown in Figure 3.5.

`Livedata` reads the raw .RPF files from the telescope and performs a bandpass calibration. To calibrate the bandpass, `Livedata` performs the ON – OFF subtraction (Equation 3.6). Once the bandpass has been calibrated, the data are then written into a pre-processed .SDFITS file. As the Mopra spectrometer, MOPS, has the ability to observe up to 16 'windows' when operating in zoom mode, the `Livedata` reduction process can convert a single .RPF file into 16 individual .SDFITS files ready to be gridded into a data cube. A data cube is the three dimensional data set which is produced by `Gridzilla`. The third dimensional information can be presented in multiple formats, including the raw telescope channel, frequency and Doppler-shifted V_{LSR} ($km\,s^{-1}$) units. `Gridzilla` can read many pre-processed .SDFITS files with the same spectral information. This allows `Gridzilla` to combine multiple maps together and writes a single output .FITS cube. Once again, if 16 'windows' were used by MOPS,

[2]See M. Calabretta ATNF home page:
`http://www.atnf.csiro.au/people/mcalabre/livedata.html`

`Gridzilla` will create 16 individual .FITS cubes.

3.2.3 Further Data Processing

`Miriad` is the standard ATNF reduction software package for use with the Australia Telescope Compact Array (ATCA). Although the software can reduce ATCA interferometer data from start to finish, the advantage of `Miriad` for single dish users is that it can also be used for image synthesis, analysis and publication. A brief outline of the `Miriad` tasks which are of particular interest to the work of this thesis follows:

- **fits:** The fits task is the gateway into and out of miriad. It reads in .FITS files and outputs them into the miriad format for further processing, and when processing is complete, will return a .FITS file to the user.
- **moment:** The moment task is probably the most used analysis task in this thesis. It provides five different ways of displaying a three dimensional (3D) data cube as a two dimensional (2D) image. The options are:
  - Moment -3: the velocity at the peak intensity
  - Moment -2: the peak intensity
  - Moment -1: the average intensity
  - Moment 0: the integrated intensity
  - Moment 1: the intensity weighted velocity
  - Moment 2: the velocity dispersion
- **regrid:** The regrid task is used to regrid images onto different scales, co-ordinate systems and co-ordinate projections. Most commonly this task was used to switch data between equatorial and Galactic co-ordinate systems.
- **maths:** The maths task allows for mathematical operations to be performed on image data.
- **cgdisp:** The cgdisp task is a plotting task, which can produce publication quality images of processed data, with overlaid contours or annotations.

For far greater detail on the use of these, and many more `Miriad` commands, see the `Miriad` users manual[3].

[3]The Online Miriad Users Guide:
`http://www.atnf.csiro.au/computing/software/miriad/userguide/userhtml.html`

3.3 Other Contributing Telescopes

Additional data collected by other astronomers are presented in this thesis. In this section, a very brief overview of the other telescopes which have contributed data is presented. The TeV γ-ray telescope system, H.E.S.S., is explained in detail later in § 6.2. A map of the Earth indicating the locations of all data contributing telescopes is presented in Figure 3.6.

- **NANTEN/NANTEN2**
  The NANTEN/NANTEN2 Observatory is a southern sky observatory. The original NANTEN telescope was located at Las Campanas, at an altitude of 2400 m, from 1994 to 2004. In 2004 it was refurbished and upgraded to the NANTEN2 telescope and moved to its current location at an altitude of 4800 m on Pampa la Bola in the Atacama Desert of northern Chile. The observatory is equipped with a 4 m diameter millimetre and sub-millimetre wave telescope that is used for southern sky observations of spectral lines in the 110 – 880 GHz range. This thesis makes use of 230 GHz CO (2-1) data towards the W28 SNR in § 3.4, § 4 and § 5.

- **Nobeyama**
  The Nobeyama Radio Observatory (NRO) consists of several instruments, including a 45 m diameter telescope. The observatory is located in Nobeyama, in the Japanese Alps, at an elevation of 1350 m. It has an observable frequency range of 20 – 230 GHz. The NRO is part of the National Astronomical Observatory of Japan (NAOJ). This thesis makes use of 115 GHz CO (1-0) data towards the W28 SNR in § 3.4 and § 4.

- **JCMT**
  The James Clerk Maxwell Telescope (JCMT) is an infrared telescope with a 15 m diameter and operational frequency range 215 – 680 GHz. It is located near the summit of Mauna Kea, Hawaii, at an altitude of 4092 m. It is part of the Mauna Kea Observatory and run by the Joint Astronomy Centre, a partnership between British, Canadian and Dutch astronomers. This thesis makes use of 345 GHz CO (3-2) data towards the W28 SNR in § 3.4 and § 4.

- **Xmm Newton**
  XMM-Newton is an orbiting X-ray observatory, launched in 1999 and placed in a very eccentric 48 hour elliptical orbit. The satellite is 10 m long and holds three X-ray telescopes. The combined collecting area is 4300 cm^{-2}. The X-ray

telescopes are sensitive to 0.2 – 12 keV photons. Observations are managed and archived at the European Space Astronomy Centre in Villafranca, Spain. This thesis makes use of 0.2 – 10 keV data towards the W28 SNR in § 4.

- **VLA**
  The Very Large Array (VLA) is a collection of 27 antennas, each with 25 m diameter, used as an interferometer. The telescopes operate in multiple frequency bands, sampling portions of the 0.07 – 50 GHz frequency range. The telescopes are arranged on a Y shaped rail allowing multiple telescope configurations. The VLA is located on the Plains of San Agustin, New Mexico, USA, at an elevation of 2124 m. It is a component of the National Radio Astronomy Observatory (NRAO). This thesis makes use of 333 MHz (90 cm) radio data in § 3.4 and 1720 MHz OH maser data towards the W28 SNR in § 3.4, § 4 and § 5.

- **Spitzer**
  The Spitzer Space Telescope is an infrared telescope launched in 2003 with a primary 85 cm diameter mirror. The satellite contains three instruments, IRAC, IRS and MIPS, allowing imaging and photometry from 3 – 180 μm, spectroscopy from 5 – 40 μm and spectrophotometry from 5 – 100 μm. Spitzer is run in partnership by NASA, JPL and Caltech. This thesis makes use of 24, 8 and 3.6 μm infrared emission towards the W28 SNR in § 3.4.

- **IRAM**
  The Institut de Radioastronomie Millimétrique (IRAM) operates two observatories for millimetre wavelength astronomy. The 30 m dish located on Pico Veleta at an elevation of 2850 m, in the Spanish Sierra Nevada, Andalucia, Spain, and an interferometer on the Plateau de Bure, at elevation 2550 m, in the French Alps. The 30 m telescope operates in the 70 – 350 GHz range. The observatories are supported by the IRAM offices and laboratories in Granada and Grenoble, respectively. This thesis makes use of 230 GHz CO (2-1) data towards the W28 SNR in § 3.4.

- **ARO**
  The Arizona Radio Observatory's 12 m radio telescope is located on Kitt Peak, 100 km from Tucson, Arizona, USA, at an elevation of 1894.5 m. The telescope currently operates in the 68 – 180 GHz range. This thesis makes use of 230 GHz CO (2-1) data towards the W28 SNR in § 3.4.

- **GBT**

  The Green Bank Telescope (GBT) is the largest fully steerable radio telescope in the world. It is touted as a 100m paraboloid telescope which operates in the 290 MHz – 90 GHz frequency band. However, the aperture of the GBT only utilises 90.4 m of the dish, and should more correctly be described by this diameter. The GBT is located at the NRAO site in Green Bank, West Virginia, USA. This thesis makes use of 1720 MHz OH data towards the W28 SNR in § 3.4, § 4 and § 5.

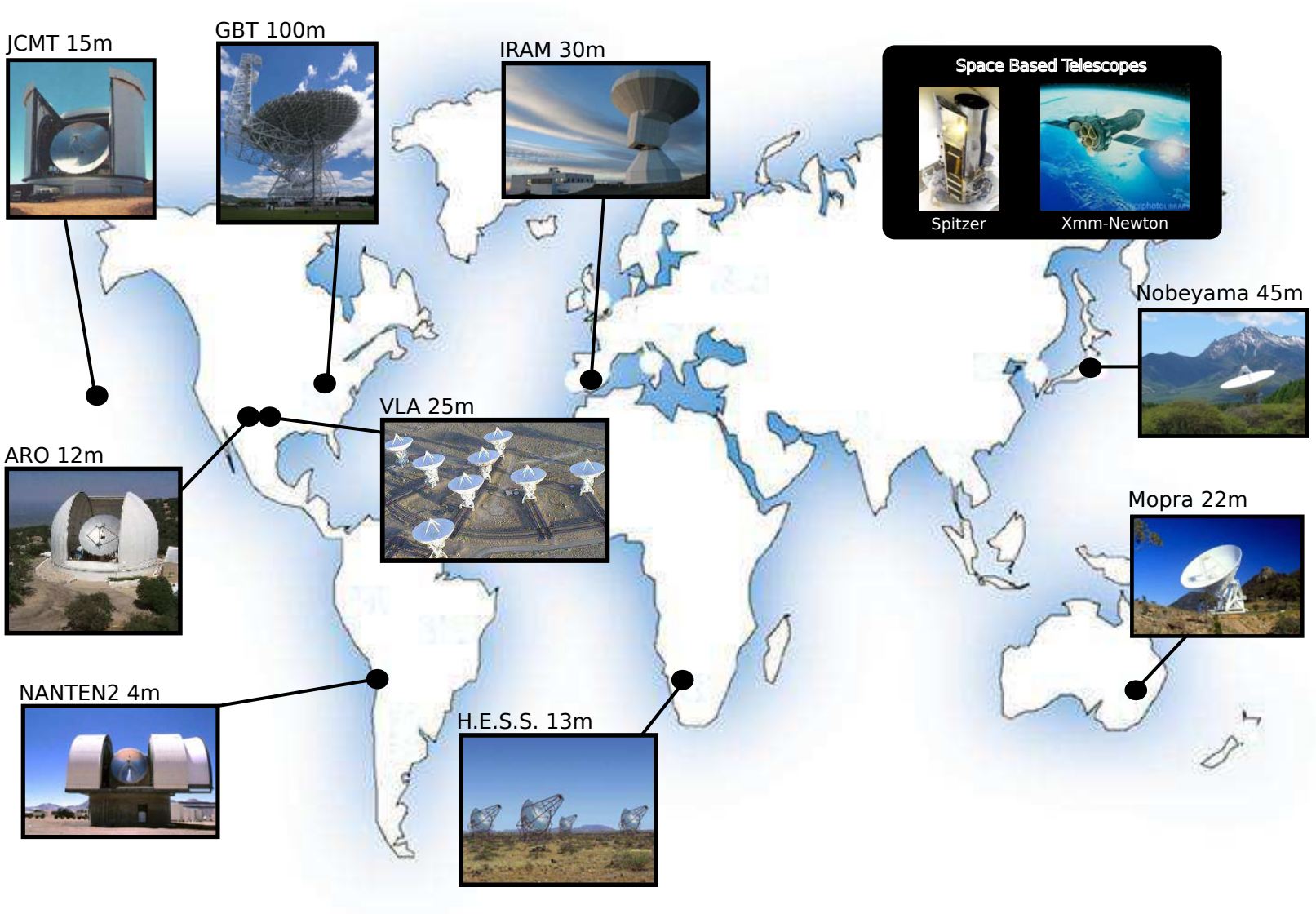

Figure 3.6: Map of the world indicating the locations of the various telescopes which have recorded data presented in this thesis.

3.4 Results of 12 mm Mopra Observations towards the W28 Supernova Remnant

This section summarises the results of a 12 mm molecular-line survey of the molecular clouds surrounding the W28 SNR. The work is presented in:

Nicholas B., Rowell G., Burton M.G., Walsh A., Fukui Y., Kawamura A., Longmore S. & Keto E., 2011, Monthly Notices of the Royal Astronomical Society (MNRAS), 411, 1367 (+ online appendices).

Abstract:
We present 12 mm Mopra observations of dense molecular gas towards the W28 supernova remnant (SNR) field. The focus is on the dense molecular gas towards the TeV gamma-ray sources detected by the HESS telescopes, which likely trace the cosmic rays from W28 and possibly other sources in the region. Using the NH_3 inversion transitions we reveal several dense cores inside the molecular clouds, the majority of which coincide with high-mass star formation and HII regions, including the energetic ultracompact HII region G5.89-0.39. A key exception to this is the cloud north-east of W28, which is well known to be disrupted as evidenced by clusters of 1720 MHz OH masers and broad CO line emission. Here we detect broad NH_3, up to the (9,9) transition, with linewidths up to 16 km s^{-1}. This broad NH_3 emission spatially matches well with the TeV source HESS J1801-233 and CO emission, and its velocity dispersion distribution suggests external disruption from the W28 SNR direction. Other lines are detected, such as HC_3N and HC_5N, H_2O masers, and many radio recombination lines, all of which are primarily found towards the southern high-mass star formation regions. These observations provide a new view on to the internal structures and dynamics of the dense molecular gas towards the W28 SNR field and, in tandem with future higher-resolution TeV gamma-ray observations, will offer the chance to probe the transport of cosmic rays into molecular clouds.

Statement of author contribution to the paper:
12mm molecular line survey of the dense molecular gas towards the W28 field Tev gamma-ray sources

Nicholas B., et al, 2011, MNRAS, 411, 1367

The analysis, presentation and write-up of the results of the 12mm molecular line survey presented in this paper has, by and large, been performed by Brent Nicholas. By signing this statement, all co-authors agree for this paper to be included in Brent's PhD. Thesis.
G. Rowell provided guidance, suggestions and editing of the final manuscript in his role of Brent's primary supervisor. M.G. Burton assisted with data acquisition at the telescope and provided comments and advice concerning the analysis, presentation and interpretation of results. A. Walsh provided access to the HOPS data and comments regarding the analysis, presentation and interpretation of the results. Y. Fukui & A. Kawamura provided access to the NANTEN data and provided comments and advice concerning the analysis, presentation and interpretation of results. S. Longmore & E. Keto conducted the radiative transfer modeling of Core 2 presented in Section 4.4, using the MOLLIE code.

Nicholas, B., Rowell, G., Burton, M.G., Walsh, A., Fukui, Y., Kawamura, A., Longmore, S. & Keto, E., (2011) 12mm line survey of the dense molecular gas towards the W28 field TeV gamma-ray sources.
Monthly Notices of the Royal Astronomical Society (MNRAS), v. 411 (2), pp. 1367-1385

CHAPTER IV

7 mm Molecular Line Observations Toward the TeV γ-Ray Sources in the SNR W28 Field

This Chapter summarises the continued work of a millimetre molecular line survey of the W28 SNR with Mopra. The results of this 7 mm line survey are presented in:

Nicholas B.P., Rowell G., Burton M.G., Walsh A.J., Fukui Y., Kawamura A. & Maxted N.I., 2011, Monthly Notices of the Royal Astronomical Society (MNRAS), *Accepted for publication. (24/08/2011).*

Abstract:
We present 7 mm Mopra observations of the dense molecular gas towards the W28 supernova remnant (SNR) field, following a previous 12 mm line survey of this region. These observations take advantage of the 7 mm beam size to probe the dense and disrupted gas in the region at ~ 1 arcmin scales. Our observations are focused towards the north-eastern (NE) HESS J1801-233 and southern HESS J1800-240 B TeV gamma-ray sources, with slightly less observations towards HESS J1800-240A & C. Using the CS (1-0) transition we reveal multiple regions of dense gas, $n_{\mathrm{H_2}} \sim 10^5\,\mathrm{cm}^{-3}$. We report the discovery of dense gas towards HESS J1800-240 C, at the site of a 1720 MHz OH maser. The NE molecular cloud is known to be disrupted, many 1720 MHz OH masers and broad CO line emission are detected at the rim of W28. Here we reveal this shock interaction region contains generally extended clumpy CS, as well as clumpy SiO and CH_3OH emission with broad line profiles. The FWHM of the molecular lines extend up to $18\,\mathrm{km\,s}^{-1}$ on the W28 side of the NE cloud. The detection of SiO towards maser clumps OH C, D, E & F provide further evidence of the shocked conditions in the NE cloud. Several other lines associated with star formation are also detected towards the

southern source, notably the energetic HII complex G5.89-0.39. The spatial match of dense gas with the TeV emission further supports the CR origin for the gamma-rays. We estimate the mass of several extended dense clouds within the field and predict the TeV flux from the dense cloud components. The predicted fluxes are on the order of 10^{-13}–10^{-14} ph cm^{-2} s^{-1}, which should be detectable and possibly resolved by a future TeV instrument, such as the Cherenkov Telescope Array.

Statement of author contribution to the paper:
A 7mm line survey of shocked and disrupted molecular gas towards the W28 field Tev gamma-ray sources.

Nicholas B., et al, 2011, MNRAS, accepted for publication August 24 2011.

The analysis presented in the write-up of the results of the 7mm molecular line survey presented in this paper has, by and large, been performed by Brent Nicholas. By signing this statement, all co-authors agree for this paper to be included in Brent's PhD Thesis.
G. Rowell provided guidance, suggestions and editing of the final manuscript in his role of Brent's primary supervisor. M.G. Burton provided comments and advice concerning the analysis, presentation and interpretation of results. A. Walsh provided comments regarding the analysis, presentation and interpretation of the results. Y. Fukui & A. Kawamura provided comments and advice concerning the analysis, presentation and interpretation of results. N. Maxted provided access to additional software and reduction routines, as well as providing comments and advice concerning the analysis, presentation and interpretation of results.

Nicholas, B., Rowell, G., Burton, M.G., Walsh, A., Fukui, Y., Kawamura, A. & Maxted, N.I. (2012) A 7 mm line survey of the shocked and disrupted molecular gas towards the W28 field TeV gamma-ray sources.
Monthly Notices of the Royal Astronomical Society (MNRAS), v. 419 (1), pp. 251-266

CHAPTER V

Deep 12 mm Molecular Line Observations Towards the North-East Cloud of W28

This Chapter concludes the millimetre molecular line survey towards W28. This work is a deep survey focussed on the north-eastern cloud of W28. The results of this work are presented in:

Nicholas B.P., Rowell G., Burton M.G., Walsh A.J., Fukui Y., Kawamura A. & Maxted N.I., *Manuscript in preparation.*

Abstract:

We present 12 mm Mopra observations of the dense molecular gas towards the north-east (NE) of the W28 supernova remnant (SNR). The NE cloud has a remarkable spatial matching to the TeV gamma-ray source HESS J1801-233 and is well known to be a SNR molecular cloud interaction region. These observations follow from our previous millimetre line surveys of this region and provide detailed NH_3 satellite spectra across the dense cloud core. Evidence of shock disruption is presented with broad line profiles causing satellite line blending of the NH_3 (1,1) inversion transition. Strong detections of the NH_3 (3,3), NH_3 (4,4) and NH_3 (6,6) inversion transitions towards these regions reveal the disruption and high temperature of the cloud. Velocity dispersion measurements point to the W28 SNR as the source of the disruption. The NH_3 spectra have been used to provide an indication of the gas parameters of the dense and disrupted cloud. Where NH_3 (1,1) satellite line blending occurs, the optically thin assumption is made provide a lower limit to the cloud mass. With these observations we provide an updated estimate for the mass of the NE cloud suggesting at least $6 \times 10^3\,M_\odot$ and as a likely lower limit $> 1.1 \times 10^4\,M_\odot$ is contained towards the NE cloud and HESS J1801-233.

Statement of author contribution to the manuscript:
Deep NH_3 survey of the disrupted molecular cloud towards the W28 TeV gamma-ray source HESS J1801-233.

Nicholas B., et al, 2011, (*manuscript in prep. for MNRAS)*

The analysis, presentation and write-up of the results of the 12mm molecular line survey presented in this manuscript has, by and large, been performed by Brent Nicholas. By signing this statement, all co-authors agree for this paper to be included in Brent's PhD. Thesis.
G. Rowell provided guidance, suggestions and editing of the final manuscript in his role of Brent's primary supervisor. M.G. Burton provided comments and advice concerning the analysis, presentation and interpretation of results. A.J. Walsh provided access to the HOPS data and comments regarding the analysis, presentation and interpretation of the results. Y. Fukui & A. Kawamura provided access to the NANTEN data and provided comments and advice concerning the analysis, presentation and interpretation of results. N.I. Maxted provided comments and advice concerning the analysis, presentation and interpretation of results.

Nicholas, B., Rowell, G., Burton, M.G., Walsh, A.J., Fukui, Y., Kawamura, A. & Maxted N., (2012) Deep NH3 survey of the disrupted molecular cloud towards the W28 TeV gamma-ray source HESS J1801-233

Monthly Notices of the Royal Astronomical Society (MNRAS), Manuscript in preparation

CHAPTER VI

TeV γ-Ray Studies of Microquasars Interacting with the ISM

This chapter is the summary of TeV γ-ray observations towards three microquasars which are interacting with the interstellar medium (ISM). It begins by outlining the details of VHE γ-ray detection techniques and provides an overview of the High Energy Stereoscopic System (H.E.S.S.). The Galactic objects known as microquasars are discussed, including their discovery and classification. The chapter concludes with the results of the H.E.S.S. observations towards Circinus X-1, where the jets are interacting with the ISM to inflate a radio nebula, Cygnus X-1, where the jets have blown out a bubble producing a termination shock, and 4U 1755-33, where 'fossil' jets extend into the ISM. The results of the H.E.S.S. observations are presented in the form of a conference proceedings.

6.1 The Ground-Based Imaging Atmospheric Cherenkov Technique

This section outlines the imaging atmospheric Cherenkov technique (IACT) for ground based TeV γ-ray detection. It also outlines some of the physical processes which result from γ-rays entering the Earth's atmosphere. The interactions of the secondary particles which originate through collisions with atmospheric nuclei are discussed. Henceforth, the ground-based γ-ray technique will simply be referred to as the IACT.

The IACT exploits the various types of interactions extraterrestrial particles have with the atmosphere. The general properties which result from these interactions, as well as how we are able to detect these interactions, and how we ultimately describe the γ-ray images are outlined in the following sections.

6.1.1 Extensive Air Showers

Whenever a high energy particle penetrates the atmosphere, it will eventually interact with atmospheric nuclei. These interactions will produce secondary particles and photons with high energies. The way in which the incident particle, the so called 'primary particle', interacts with the atmosphere is different depending on its nature, which can either be hadronic or electromagnetic. Regardless of the primary particle's nature, after it experiences its first interaction there will be secondary particles and photons produced. These secondary particles and photons will, in turn, interact with atmospheric nuclei and photons to create more particles. This process continues on, creating a cascade of particles called an air shower, or an extensive air shower (EAS). There are two major types of EAS, which are determined by the nature of the primary particle. If the primary particle is a photon or an electron, then the observed shower is considered an electromagnetic (EM) EAS. In comparison, if the incident particle is a hadron, then the observed EAS is considered hadronic.

6.1.2 Electromagnetic EAS

When a high energy electron or photon, a γ-ray, enters the atmosphere an electromagnetic EAS will develop. In the presence of atmospheric nuclei, a γ-ray will undergo pair production. Pair production (PP) is the creation of an elementary particle and its antiparticle from a photon, in this case, an electron, e^-, and a positron, e^+, are created. As these newly formed e^-/e^+ pairs are surrounded by atomic Coulomb fields, they will be accelerated and emit new photons via Bremsstrahlung. These newly formed photons are also of high energy, and can undergo pair production. This process of creating e^-/e^+ pairs which radiate Bremsstrahlung photons continues, creating a cascade of particles and photons, the air shower. The cycle will only cease when the energy of the particles falls below the critical energy, E_c, where the energy loss rate by competing ionisation processes is greater than the energy loss from Bremsstrahlung. Once this critical energy is reached, there can be no increase in particle numbers and thus the shower terminates.

There are many different models for the development of an EAS in the atmosphere but a simple model, which gives an understanding of EM air showers, is by Heitler (1954). In this simplified model, only pair production and Bremsstrahlung are considered. The model also assumes equal interaction lengths, λ (g cm^{-2}), for pair production, λ_{PP}, and Bremsstrahlung, λ_B, neglecting the factor of 9/7 which relates them. After one interaction length, the e^- and e^+ radiate a Bremsstrahlung photon carrying away half the particle's energy. These radiated photons will also undergo pair production

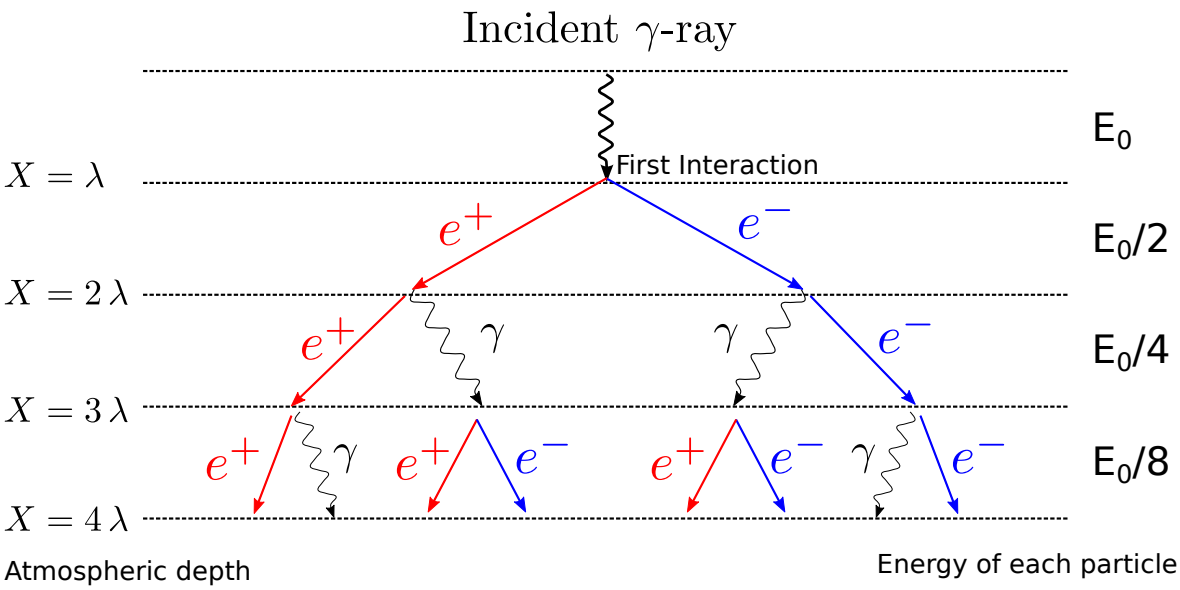

Figure 6.1: A simple model which illustrates the evolution of an EM air shower according to Heitler (1954). An incident γ-ray photon undergoes pair production into electron and positron pairs, e^-/e^+, which, in turn, radiate Bremsstrahlung photons, γ. Four interaction lengths, λ, are shown by the left-side scale and the energy of each particle, related to the energy of the primary particle, E_0, is shown by the right-side scale.

to produce additional e^-/e^+ pairs. This continuing process builds up the EAS. Figure 6.1 is a graphical representation of these assumptions.

This model shows that after n radiation lengths, at an atmospheric depth, X, there are 2^n particles, each with energy:

$$E(n) = E_0\, 2^{-n} \quad [\text{eV}] \tag{6.1}$$

There is a critical energy, E_c, at which this process stops. Therefore there is also a maximum number of particles, $N_{\max}$, that can be created. The maximum number of particles in the shower is:

$$N_{\max} = \frac{E_0}{E_c} \tag{6.2}$$

The maximum number of particles is also related to the depth at shower maximum, $X_{\max}$, by:

$$N_{\max} = 2^{X_{\max}/\lambda} \tag{6.3}$$

When $N_{\max}$ is reached, roughly 2/3 are particles (e^-/e^+) and 1/3 are photons.

Combining Equations 6.2 and 6.3 gives an expression for the depth at shower maximum, $X_{\max}$:

$$X_{\max} = \lambda \frac{\ln\left(\frac{E_0}{E_c}\right)}{\ln(2)} \quad [\mathrm{g\,cm^{-2}}] \tag{6.4}$$

This very simplified model represents the two most important features:

- The number of particles at shower maximum is proportional to E_0
- The atmospheric depth at shower maximum is logarithmically proportional to E_0

6.1.3 Hadronic EAS

Hadronic EAS result when the primary particle is a particle with mass (proton, α or heavier nuclei). If the primary high energy particle is hadronic, its interactions will cause nuclear fragmentation and will interact via the strong force. Hadronic EAS contain a greater variety of secondary particles. Along with the pair produced e^-/e^+ pairs and Bremsstrahlung photons, muons (μ^+, μ^-), pions (π^+, π^-, π^0) and nucleons from nuclear fragmentation, are also produced. Due to the creation of the pions, and their subsequent decay chains:

$$\begin{aligned} \pi^+ &\longrightarrow \mu^+ + \nu_\mu \\ \pi^- &\longrightarrow \mu^- + \bar{\nu_\mu} \\ \pi^0 &\longrightarrow 2\gamma \longrightarrow 2\,(e^+ + e^-) \end{aligned} \tag{6.5}$$

hadronic EAS consist of multiple components. Hadronic EAS have sub-electromagnetic components, initiated through the decay of the π^0; a meson component, through the decay of the $\pi^{+,-}$ and a nucleonic component, through the fragmentation of atmospheric nuclei. Shown in Figure 6.2 is the development of a hadronic induced EAS, which reveals the multiple sub-components. The secondary particles created in the nucleonic component receive large transverse momentum through inelastic scattering causing the particles to spread laterally. This is demonstrated in Figure 6.3 which shows a Monte Carlo simulation of an EM EAS, resulting from a 300 GeV γ-ray, compared to a hadronic EAS, resulting from a 1 TeV hadron (a proton).

Figure 6.2: An example of the development of a hadronic induced extensive air shower, showing the different sub-components. Hadronic EAS contain sub-electromagnetic components, a meson component and a nucleonic component. Image adapted from Funk (2002).

6.1.4 Differences Between Hadronic and Electromagnetic EAS

There are several differences between EM and hadronic induced EAS. A brief summary of some of the major differences follows.

- The interaction length, λ, for hadrons is larger than for photons. As such, hadrons are able to penetrate further into the atmosphere, and thus have higher $X_{\max}$. Since atmospheric depth, X, is measured from the top of the atmosphere, the higher the X value, the closer to the ground the shower will reach.

- Hadronic showers laterally spread out further than electromagnetic EAS due to the transverse momentum from inelastic scattering.

- The decay of $\pi^0 \rightarrow 2\gamma$ gives rise to sub-electromagnetic EAS within hadronic EAS.

- The number of different particle types and different kinds of interactions in hadronic showers, makes their shape irregular. They also have larger shower-to-shower fluctuations, compared to the relatively simple three particle EM system.

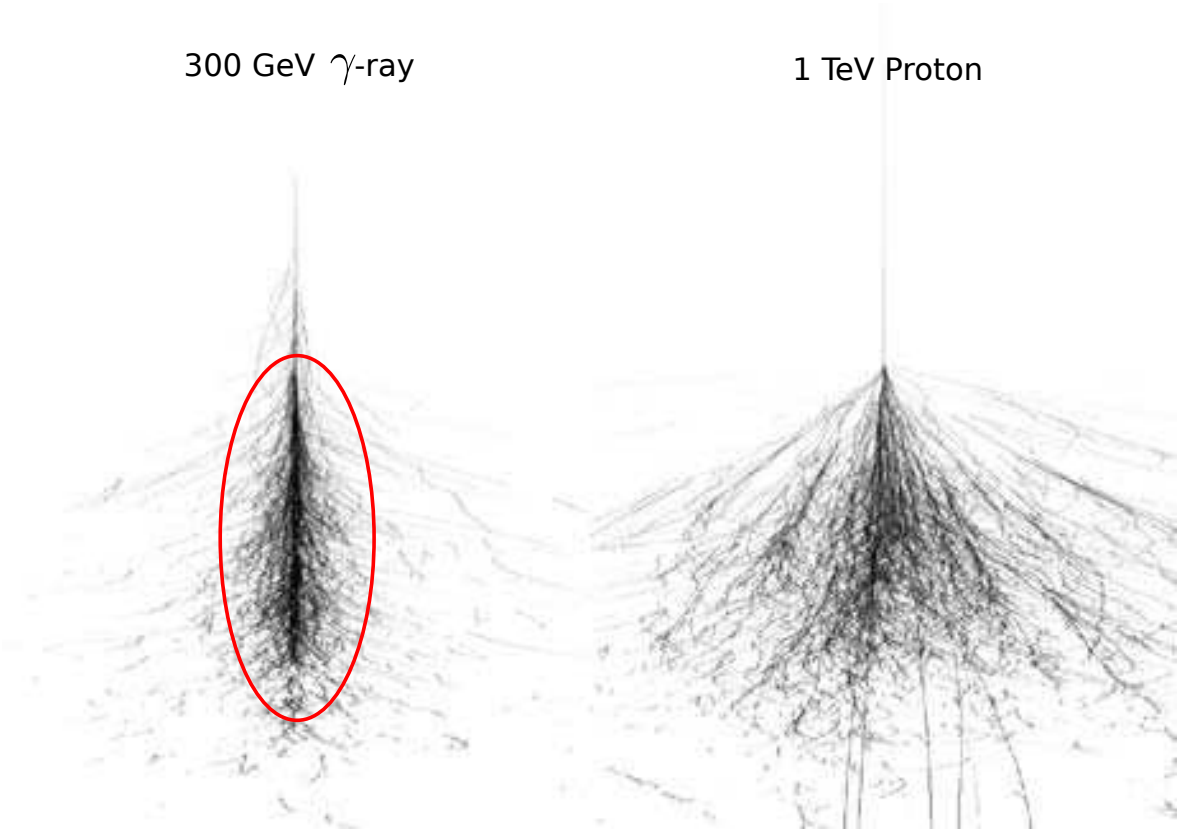

Figure 6.3: An example of the particle tracks of a 300 GeV γ-ray compared to a 1 TeV proton. For $E < 100$ TeV, γ-ray showers are approximately 2–3 times more efficient at producing EM EAS than CR showers of the same energy, hence the comparison between a 300 GeV γ-ray and a 1 TeV CR. The γ-ray shower is 'regular' and can be approximated as elliptically shaped, indicated by the red ellipse. The hadronic induced EAS is 'irregular' and has larger lateral spread due to the extra transverse momentum from the inelastic scattering. Image adapted from Völk & Bernlöhr (2009).

6.1.5 Cherenkov Radiation

Cherenkov radiation is emitted when a relativistic charged particle is moving faster than the phase velocity of light through a dielectric medium. It can be considered as the electromagnetic equivalent to a sonic boom which is produced when travelling faster than the speed of sound. The relativistic charged particles temporarily polarise (on a macroscopic scale) the molecules surrounding them. Once the high velocity particle has moved away, these polarised molecules oscillate back to restore equilibrium and emit EM radiation. For a particle travelling at a velocity, v, comparable (or below) the velocity of light in the medium, $v^* = c/n$, where n is the refractive index of the medium, the EM radiation will destructively interfere and hence, no radiation is detected. For the case of a particle travelling faster than the speed of light in the medium, that is:

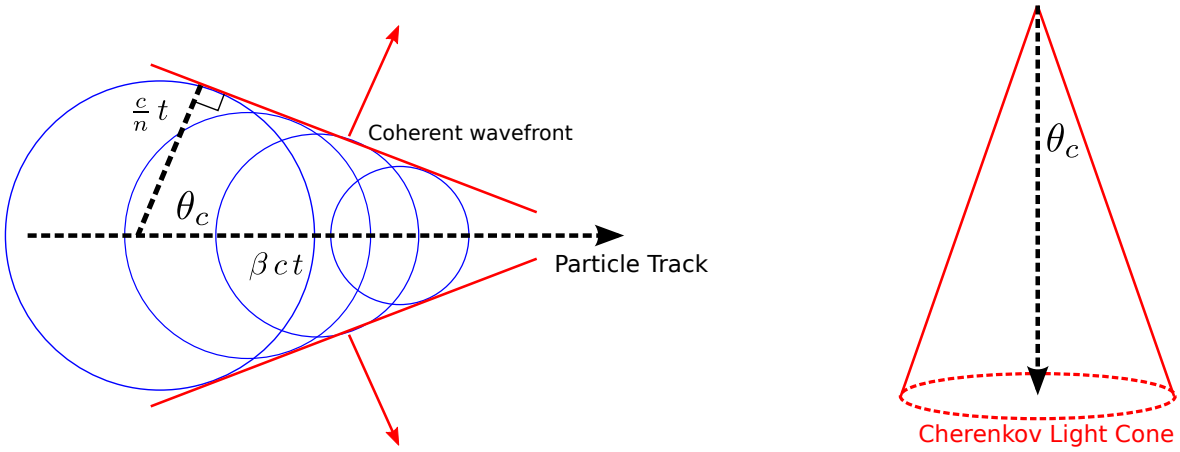

Figure 6.4: A schematic showing the geometry of Cherenkov radiation. The light is emitted along the particle track. **Left:** A Huygens' construction for each wavelet (blue circles) showing how for some critical angle, θ_c, these wavelets will constructively interfere to create a coherent wavefront (red lines). **Right:** The Cherenkov light cone which results from the Cherenkov emission at θ_c.

$$v > v^* \equiv v > \frac{c}{n} \tag{6.6}$$

the EM radiation will constructively interfere and Cherenkov radiation can be detected. Figure 6.4 is a schematic indicating the geometry of Cherenkov radiation, showing a Huygens' construction for each wavelet. In a time interval, t, the particle travels a distance $v\,t = \beta\,c\,t$, where $\beta = v/c$. The light emitted from each point along the particles track will travel a distance $c\,t/n$ in the same time. This means that radiation will be emitted at an angle θ_c from the particles track, given by:

$$\cos(\theta_c) = \frac{c\,t/n}{\beta\,c\,t} = \frac{1}{n\beta} \tag{6.7}$$

Since this angle is independent of time, t, the Cherenkov radiation is always emitted at the same angle, θ_c, along the entire particle track. The critical angle of Cherenkov emission, Equation 6.7, is proportional to the particle's velocity. This determines a maximum Cherenkov angle, $\theta_{c,\max}$ for particles travelling at velocity c. For an ultra-relativistic particle, $v \approx c$ or $\beta \approx 1$ then:

$$\theta_{c,\max} = \cos^{-1}\left(\frac{1}{n}\right) \tag{6.8}$$

Equation 6.6 determines a threshold velocity, v_{min}, below which a particle cannot emit Cherenkov radiation:

$$v_{\min} = \frac{c}{n} \tag{6.9}$$

Using this threshold velocity in the relativistic energy equation determines the minimum energy of a particle which is able to produce Cherenkov radiation:

$$E_{\min} = \gamma\, m\, c^2 \quad \text{where} \quad \gamma = \frac{c}{\sqrt{c^2 - v_{\min}^2}} \tag{6.10}$$

For electrons in the Earth's atmosphere, this minimum energy is several tens of MeV.

Based on the work of Frank & Tamm (1937) the number of Cherenkov photons, N, emitted per unit path length, x, in the wavelength range λ_1 to λ_2 is given by the well known expression (e.g. Bernlöhr 2000):

$$\frac{dN}{dx} = 2\,\pi\,\alpha\,z^2 \int_{\lambda_1}^{\lambda_2} \left(1 - \frac{1}{[\beta\, n(\lambda)]^2}\right) \frac{1}{\lambda^2}\, d\lambda \tag{6.11}$$

where α is the fine structure constant ($\alpha = 1/137$) and z is the charge number of the particle ($z = 1$ for an electron). Radiation is limited to frequency bands where the refractive index, $n(\lambda) > 1$. This window closes at the X-ray regions as $\mathrm{n}(\lambda) < 1$ and radiation is therefore forbidden as it violates Equation 6.8.

Air showers are initiated by very high energy particles, and as such, the secondary particles created in an EAS are also of high energy. Therefore, the secondary charged particles are also travelling at relativistic speeds and will produce Cherenkov radiation. It is this Cherenkov radiation which, when measured by Cherenkov telescopes, leads to an image of the EAS.

From Equation 6.11, the expected yield of Cherenkov photons, ph, can be determined. Knowing the expected number of Cherenkov photons that will be emitted in the shower, can lead to the technical aspects of detection, such as, the size of the mirror required for the telescope. For a primary particle with initial energy, E_0, in the range $E_0 \sim 0.1$–$10\,\mathrm{TeV}$, the Cherenkov photon density, near the shower axis, is of the order of 10–$1000\,\mathrm{ph\,m^{-2}\,ns^{-1}}$ ($\mathrm{ns} = 10^{-9}\,\mathrm{s}$). The night sky background (NSB) has a photon flux $\sim 10^{12}\,\mathrm{ph\,m^{-2}\,s^{-1}\,sr^{-1}}$ in the same wavelength range as Cherenkov radiation ($\lambda =$ 200–700 nm). The expected signal from both the Cherenkov radiation, S, and from the NSB, N, is given by:

$$S = C \left(\frac{\Phi_{\mathrm{Ch}}}{\mathrm{ph\,m^{-2}}}\right) \left(\frac{A}{\mathrm{m^2}}\right) \quad [\mathrm{ph}] \tag{6.12}$$

$$N = C \left(\frac{\Phi_{\mathrm{NSB}}}{\mathrm{ph\,m^{-2}}}\right) \left(\frac{A}{\mathrm{m^2}}\right) \left(\frac{\Omega}{\mathrm{sr}}\right) \left(\frac{\tau}{\mathrm{ns}}\right) \quad [\mathrm{ph}] \tag{6.13}$$

where C is a factor accounting for efficiencies in the mirror and photomultiplier tubes, Φ_{Ch} and Φ_{NSB} are the flux of Cherenkov and NSB photons, respectively, A is the area of the telescope's mirror, Ω is the solid angle of the telescope's field of view and τ is the integration time. Therefore, to detect Cherenkov radiation with a signal-to-noise ratio, $S/\sqrt{N}$, requires a mirror with collecting area given by:

$$A = \left(\frac{S/\sqrt{N}}{\Phi_{\mathrm{Ch}}}\right)^2 \frac{\Omega\,\tau\,\Phi_{\mathrm{NSB}}}{C} \quad [\mathrm{m^2}] \tag{6.14}$$

By Equation 6.14, a mirror with collecting area $\sim 100\,\mathrm{m^2}$ is required to detect a typical 5 ns Cherenkov pulse with a signal-to-noise ratio of 5, looking over a 5 degree (diameter) field of view ($5^\circ = 1.6 \times 10^{-3}\,\mathrm{sr}$), with typical efficiencies $C \sim 0.07$. These are the operational parameters for the H.E.S.S. telescope system which consists of four telescopes, each with area $108\,\mathrm{m^2}$. The H.E.S.S. project is is discussed in more detail in § 6.2.

6.1.6 Cherenkov Imaging

Cherenkov telescopes map the Cherenkov light from the EAS onto an imaging camera which is located in the focal plane of the reflecting surface. It is the Cherenkov light cone from each particle which is reflected and recorded in the camera. Light arriving from the same angle with respect to the optical axis is mapped to the same point in the image. Therefore the camera image is the angular distribution of Cherenkov light. A graphical view of the Cherenkov light mapping property, from the air to the camera, is displayed in Figure 6.5.

The secondary charged particles produced in an EAS will produce Cherenkov radiation along their particle tracks. As indicated in Figure 6.3, the secondary particle tracks in γ-ray EAS have an almost elliptical distribution in the atmosphere. The superposition of all the Cherenkov light cones in the atmosphere is also elliptical and the Cherenkov mapping indicted in Figure 6.5 reproduces this distribution as an ellipse in the camera.

Figure 6.5: A schematic that shows the geometrical mapping of Cherenkov light (green shaded region) into the camera. Beam 1 is at a small angle with respect to the optical axis of the reflector, while beam 3 is at a large angle. Consequently, beam 1 is mapped closer in the image whilst beam 3 is mapped further into the image. The inset shows the orientation of the image in the camera. Image adapted from Berge (2006).

6.1.7 PMTs and Cherenkov Cameras

A Cherenkov camera is used to collect the photons which are reflected from the telescopes primary mirror. The standard way to record light is to use a photomultiplier tube (PMT), which utilises the photoelectric effect to produce an electrical current. The photocathode releases electrons when a photon is incident on the surface of the PMT. These photoelectrons are then accelerated by an electric field through a series of dynodes, whose surfaces are designed to multiply the number of electrons. Secondary electrons are accelerated from one dynode to the next such that the total number of electrons is multiplied. Finally, all the electrons will arrive at the anode, producing an electronic pulse which is then recorded.

A Cherenkov camera is an array of PMTs arranged in a 2D shape (square or hexagonal) and each of the PMTs is a single pixel of the camera. For high image resolution,

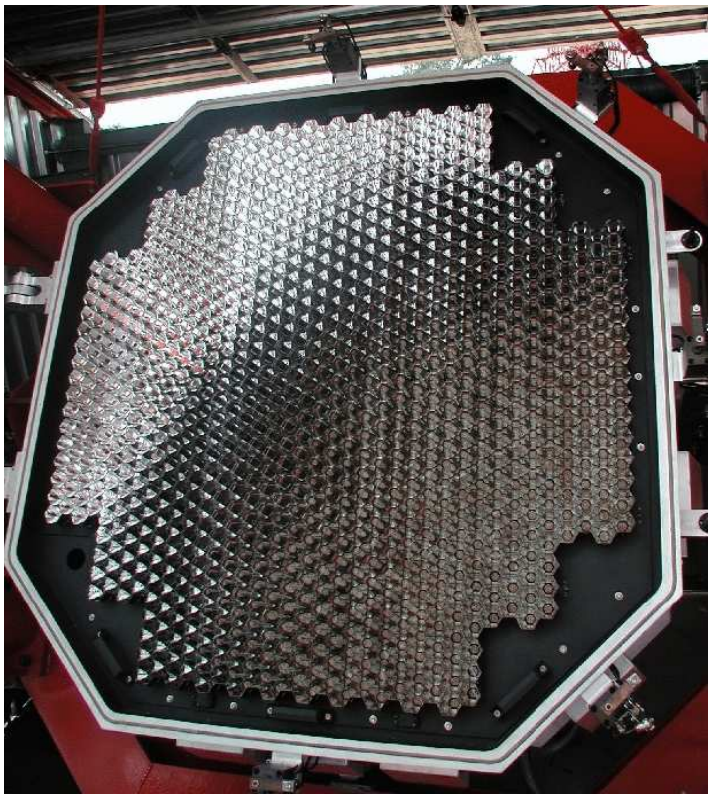

Figure 6.6: The hexagonal arrangement of the PMTs within a H.E.S.S. telescope camera. The camera itself is $\sim 1.5\,\mathrm{m}$ across, containing 960 individual PMTs.

there needs to be a large number of closely spaced PMTs. Shown in Figure 6.6 is the hexagonal shape the PMTs within a Cherenkov camera. More details on Cherenkov cameras, specifically towards the H.E.S.S. cameras, are provided in § 6.2.3. The images produced by Cherenkov cameras need to be 'cleaned' before they can be used effectively. The cleaning processes takes Cherenkov camera images and removes isolated pixels which are either PMT or NSB noise, leaving the image of the EAS only.

6.1.8 Image Parametrisation using Hillas Parameters

The parametrisation of Cherenkov light emission observed in the PMT camera as the moments of an ellipse was first proposed by Hillas (1985). The 'Hillas parameters' are used to reconstruct and determine the air shower direction and energy, as well as determining the primary particle's type. These parameters have become standard for γ-ray image parametrisation. They were first used by the Whipple telescope (Weekes *et al.*, 1989) and the High Energy Gamma Ray Astronomy (HEGRA) experiment (Konopelko *et al.*, 2002). A schematic of some of these parameters are shown in Figure 6.7. Below is a brief description of the indicated parameters. A mathematical description of the

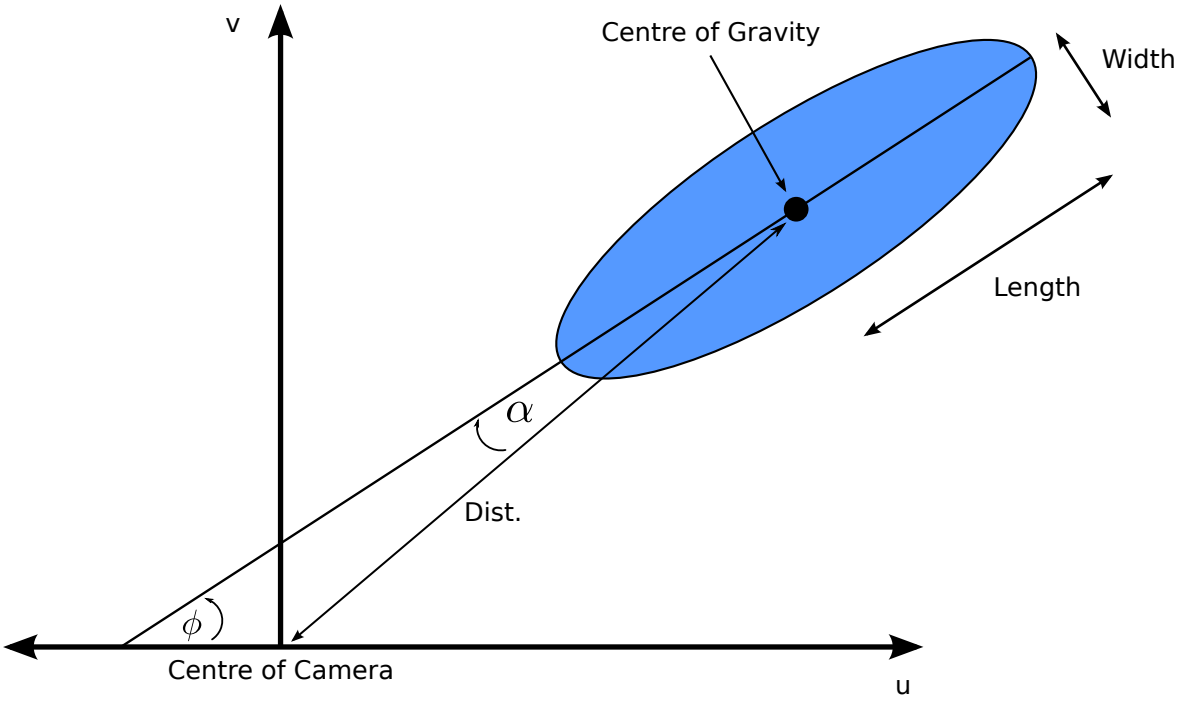

Figure 6.7: A simple graphical view of some of the Hillas parameters. The length, L, is the semi-major axis of the ellipse, the width, W, is the semi-minor axis of the ellipse, the centre of gravity, CoG, is the intensity weighted mean of the ellipse (for a uniform distribution of light this is the geometric centre), the dist. is the distance between the CoG and the centre of the camera and the image size is indicated by the area of the ellipse. The angle α is the orientation angle of the image within the camera and ϕ is the direction angle with respect to the camera. The u and v axis correspond to the camera plane.

following Hillas parameters can be seen in Appendix A.

- **Size:**
  The size parameter is a measure of the total number of photons detected from the shower. Each individual camera pixel records the number of photons it receives. The sum of all the photons received describes the image size.

- **Centre of Gravity:**
  The Hillas centre of gravity, CoG, is the intensity weighted mean position of the signal. For a uniform distribution of light, this is simply the geometric centre of the image.

- **Length and Width:**
  The length, L, and width, W, parameters are related to the major and semi-major axes of the ellipse. The Hillas length and width parameters provide an effective cut to separate between the CR and γ-ray images, explained later in § 6.3.

- **Dist.:**
  Dist is the distance between the CoG of the image and the centre of the camera.

6.2 The High Energy Stereoscopic System H.E.S.S.

The high energy stereoscopic system (H.E.S.S.) is an array of four 13 m diameter imaging atmospheric Cherenkov telescopes. H.E.S.S. is used to detect γ-ray showers in the VHE band, specifically at TeV (10^{12}eV) energies. It operates in the 0.1–30 TeV range. The name H.E.S.S. also honours Victor Francis Hess, whose discovery of cosmic-rays made him the co-recipient of the 1936 Nobel Prize in Physics. H.E.S.S. is a stereoscopic system, which means there is more than one telescope observing an air shower. Therefore the system is potentially able to collect data from four different viewing angles simultaneously. Another advantage of the multi-telescope system is that increasing the number of telescopes increases the effective detection area of the instrument.

H.E.S.S. is located in the Khomas Highland of Namibia, approximately 100 km from the capital Windhoek, near the Gamsberg Mountain. A map indicating the H.E.S.S. site is shown in Figure 6.8. This site is well known for its excellent conditions for astrophysical observations. The site's exact location is 23°16′18″ south, 16°30′00″ east, with an elevation of 1800 m above sea level. The advantage of this site is that it has many cloud-free nights, which are needed for the Cherenkov detection of EAS.

The elevation of the site affects the energy threshold of the system. For lower energy EAS, the $X_{\max}$ of the shower is higher in the atmosphere, where as higher energy EAS penetrate deeper into the atmosphere (§ 6.1.2). At a lower site altitude (closer to sea-level), the threshold energy[1] of the system increases. This is because the system will only detect the higher energy EAS which can penetrate further into the atmosphere (closer to sea-level). The lower energy EAS do not have as much penetrating power and will terminate higher in the atmosphere and the light never reaches the telescopes.

As the site is in the southern hemisphere, it provides excellent coverage of the Galactic plane towards the Galactic Centre.. The Galactic plane has proven to be a region with a large number of VHE γ-ray emitting sources, as shown in Figure 1.9. Phase I of the H.E.S.S. project was officially inaugurated on September 28, 2004 and continues to run today. Phase II of the project, the addition of a giant 30 m telescope, has begun construction. A site photo, showing the four telescopes and the control centre of H.E.S.S, as well as how the H.E.S.S. II site will look upon completion of the 30 m telescope, is shown in Figure 6.9.

[1] the threshold energy is the minimum energy EAS that the system can detect.

Figure 6.8: A map showing the location of the H.E.S.S. site (indicated by the cross $\times$) south west of Windhoek, the capital of Namibia, Africa.

6.2.1 Telescope Arrangement

Phase I of the project consists of the four 13 m diameter imaging air Cherenkov telescopes, arranged in a square of side length 120 m to provide the 'stereoscopic' view of EAS. The square is aligned to have diagonals running north-south and east-west. The telescope spacing is a compromise between the baseline length required to allow good stereoscopic imaging, and the triggering condition that two or more telescopes lie within the Cherenkov light pool, shown in Figure 6.10. Triggering means that shower data are only recorded if two or more telescopes 'view' the same shower. Phase II of the project is to add an additional large, 30 m, telescope in the centre of the array. This additional telescope, with an effective collecting area of 600 m^2, will increase the energy coverage, sensitivity and angular resolution of the system at lower energies (< 0.1 TeV).

6.2.2 Telescope Construction

The telescopes use altitude-azimuth (alt-az) mounts, allowing them to point in any direction in the sky. Each telescope is computer controlled to allow tracking of celestial objects across the sky, with a maximum slewing speed of approximately 100° per

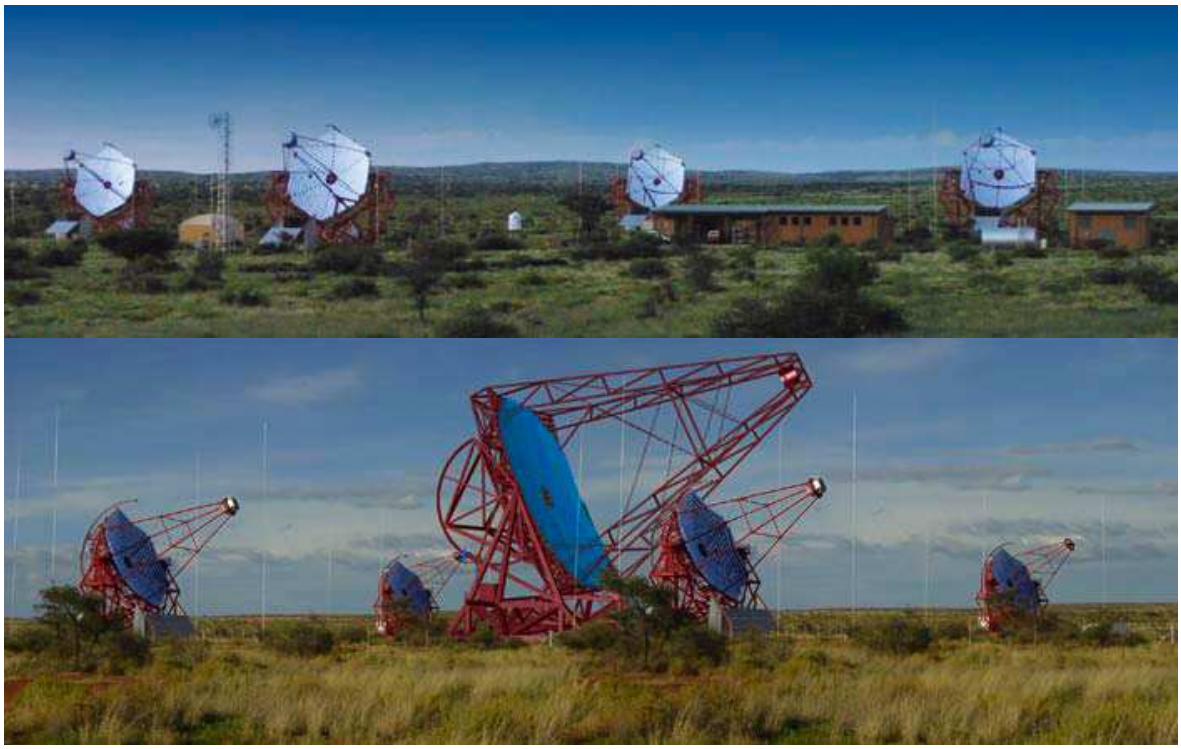

Figure 6.9: **Top:** A photo of the H.E.S.S site after completion of Phase I. The four 13 m imaging air Cherenkov telescopes and the control centre are shown. **Bottom:** An image showing how the H.E.S.S. site will look after the completion of Phase II. Image credits Völk & Bernlöhr (2009).

minute. The reflecting surface consists of 382 individual round mirrors, 60 cm in diameter, made of aluminised glass with a quartz coating. Each one of the 382 individual mirrors is able to be aligned by two remote controlled motors. The complete reflecting surface is 108 m^2 with a focal length, f, of 15 m. Four arms support the camera at the focal length of the reflecting surface. Each telescope weighs 60 tonnes, complete with mirrors, camera, drive systems and framework. A single H.E.S.S. telescope is shown in Figure 6.11.

6.2.3 Telescope Camera

The cameras are designed to capture and record the Cherenkov images of air showers. They were specifically designed to have a small pixel size in order to resolve image details, a large field of view for observations of extended sources and surveys, and a triggering scheme to identify Cherenkov light and reject the night sky background. Each telescope camera has a wide 5° (diameter) field of view at full operating angle and contains 960 individual PMTs as pixels. Each PMT is 0.16° in angular size and is equipped with a Winston cone to direct the light onto the active area of the PMT

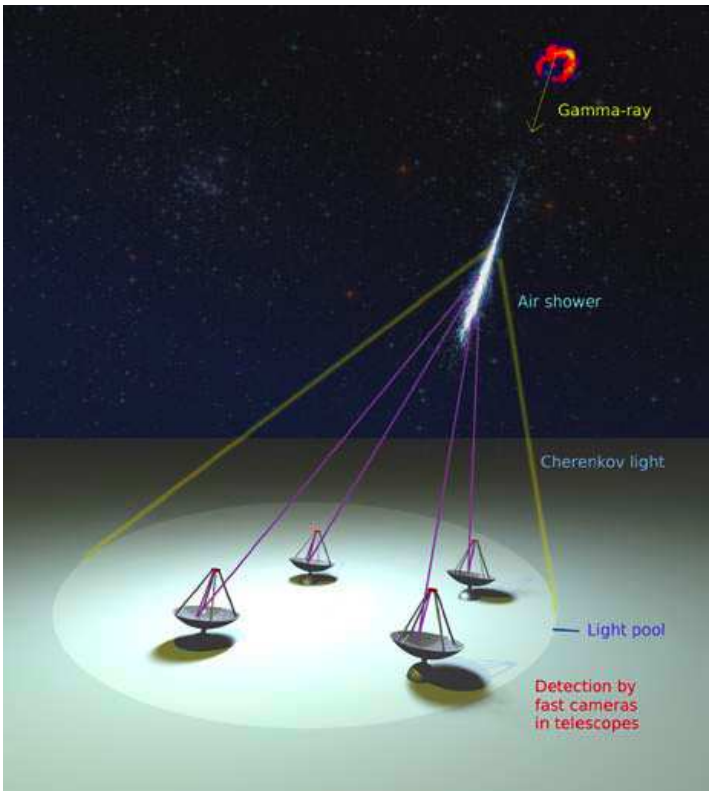

Figure 6.10: A schematic showing the arrangement of IACT telescopes, such as the H.E.S.S. telescopes, within the Cherenkov light pool. The telescopes will detect the γ-ray event if they lie within the Cherenkov light pool. Image credit Völk & Bernlöhr (2009).

and avoid photon losses. The PMTs are arranged in a hexagonal pattern with 120° rotational symmetry. The cameras are 1.6 m in diameter, 1.5 m long and weigh approximately 800 kg. A H.E.S.S. camera showing the hexagonal arrangement of the PMTs is shown in Figure 6.6 and Figure 6.11.

6.3 Reducing H.E.S.S. Stereoscopic Data

The first step in the data processing pipeline is to determine whether data were recorded under ideal conditions. The data are checked against selection criteria, such as weather conditions, hardware failure and telescope trigger rate. The next stage is the cleaning of the images to remove any PMT or night sky background (NSB) noise. Once the images have been cleaned they are parametrised by Hillas parameters (§ 6.1.8). A geometrical image reconstruction is carried out using the stereoscopic images. Since H.E.S.S. consists of four imaging air Cherenkov telescopes, it can have up to four different views of each EAS. Combining these images allows a γ-ray arrival direction to be reconstructed. To reconstruct the arrival direction images are taken in pairs and

Figure 6.11: Left: A photo of one of the H.E.S.S. telescopes showing the mounting, reflecting mirrors and camera. **Right:** A photo of the inside of a H.E.S.S. camera. The individual PMTs are arranged in a hexagonal manner. Images from Berge (2006).

each images intersection point is weighted by the quality of the image. More details on stereoscopic reconstruction can be found in Hofmann *et al.* (1999).

One of the simplest reconstruction methods used by H.E.S.S. is *'algorithm 1'*. For N telescopes, this results in $N(N-1)/2$ intersection points. Each point is weighted by the sine of the angle between the Hillas length vectors to anti-bias parallel pairs, and the inferred arrival direction is the average of all the intersection points. The *'algorithm 1'* reconstruction method is pictured in Figure 6.12.

6.3.1 Cosmic-Ray Background Rejection using Image Shape

Cosmic-rays will produce unwanted EAS which constantly trigger the telescope system. Typically, CR EAS outnumber the γ-ray EAS by one thousand to one. To reject the unwanted CR showers, the data undergo selection cuts to limit the data to mostly γ-ray signals. Although several cuts can be made, most commonly a cut on the Hillas 'width' of the image is used. The reason for this was briefly noted in § 6.1.4. Hadronic EAS have large lateral spread, so they will have a larger Hillas width parameter than EM EAS. For multi-telescope systems, the mean reduced scaled width (MRSW), $\bar{\omega}$, is defined as:

$$\bar{\omega} = \frac{1}{N_{\mathrm{tel}}} \sum_{i}^{N_{\mathrm{tel}}} \frac{\mathrm{width}_i - \langle \mathrm{width} \rangle_i}{\langle \sigma_i \rangle} \tag{6.15}$$

where width_i is the Hillas width from the γ-ray image, $\langle \mathrm{width}_i \rangle$ is the mean expected

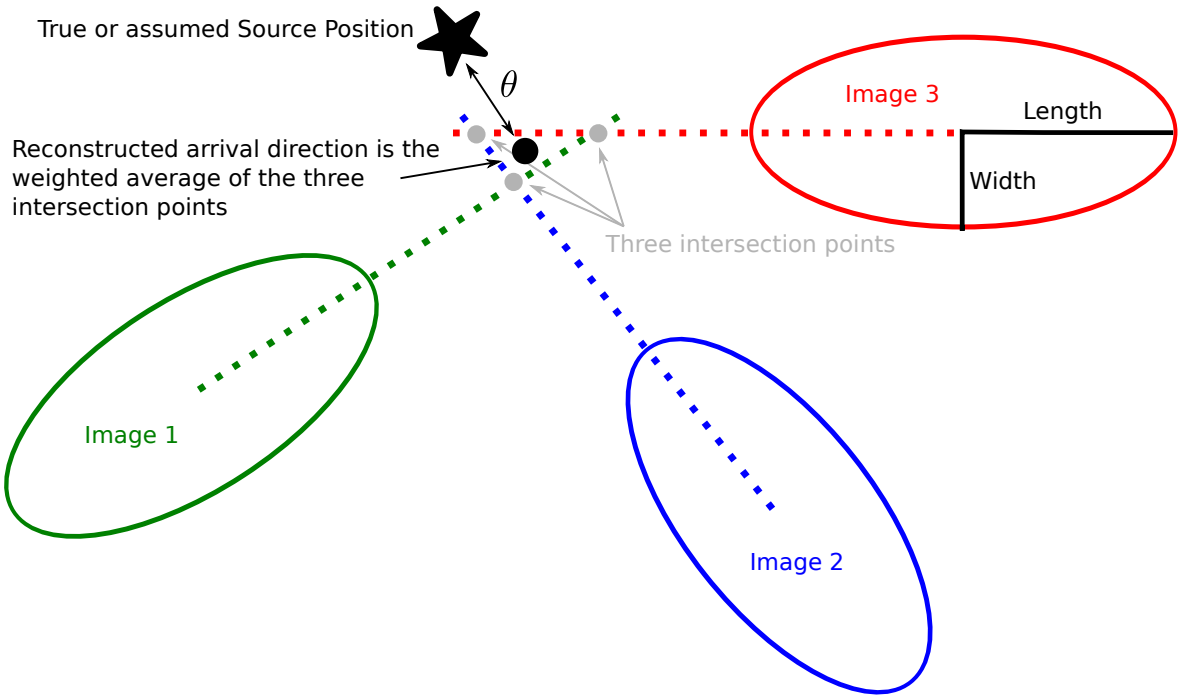

Figure 6.12: A schematic of the *'algorithm 1'* reconstruction with three Cherenkov images. The telescopes Cherenkov images have the major axis traced back to determine the reconstructed arrival direction. The parameter θ is the angular distance between the reconstructed event direction on the sky and the true (or assumed) source position on the sky.

width of a shower, generated from Monte Carlo simulations of true γ-ray EAS, with the same image size and $\langle\sigma_i\rangle$ is the RMS spread in $\langle\text{width}_i\rangle$ of the simulation. The same treatment can be applied to the Hillas length parameter to create a mean reduced scaled length (MRSL), $\bar{l}$. An illustration of the effectiveness of the MRSW cut to discriminate between γ-ray and CR induced EAS is displayed in Figure 6.13.

6.3.2 Total Cuts on Data

The MRSW parameter is not the only selection cut that data have to survive. There are several other types of image selection cuts which limit the available data. The so called *'hard cuts'* give better sensitivity at higher energies. For H.E.S.S. the *'hard cuts'* require that:

- Image **size** $>$ **200** photoelectrons.
- The **MRSW** in the range $\mathbf{-0.2 < \bar{\omega} < 0.7}$.
- The **MRSL** in the range $\mathbf{-0.2 < \bar{l} < 2.0}$.
- The point source $\boldsymbol{\theta} < \mathbf{0.1}^\circ$.

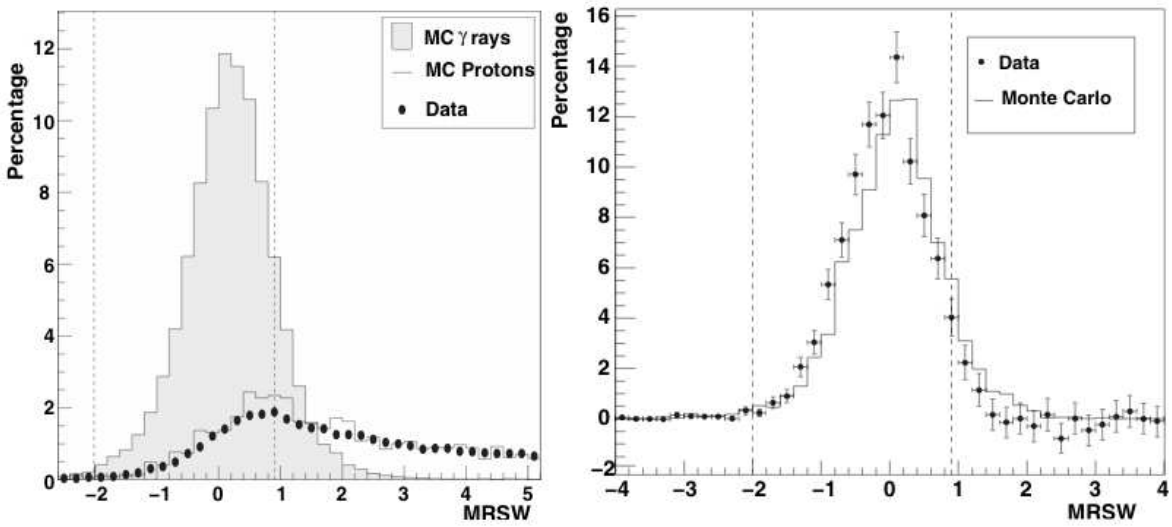

Figure 6.13: Distributions of the MRSW parameter. **Left:** The shaded and un-shaded regions represent γ-ray events and CR events from Monte Carlo simulations, respectively. The black data points are real CR data. **Right:** The Monte Carlo simulated γ-ray events compared to real data. In both panels the vertical dashed lines represent the bounds for the standard cut on the MRSW. The region bounded by the vertical lines will accept approximately 80% of the γ-ray events and only 1-2% of the CR events. Image from Aharonian *et al.* (2006b).

- The **Dist.** $< \mathbf{0.525}$ m.

where photoelectrons are the signal output from the PMTs. The θ parameter is the angular distance between the reconstructed and true (or assumed) arrival direction (see Figure 6.12). This sets the integration range for the production of skymaps (see § 6.3.3 for details on skymap production). The choice of $\theta < 0.1^\circ$ comes from the point spread function (PSF) of the telescope[2]. The distance parameter is the distance between the image's centre of gravity and the centre of the camera (see Figure 6.7). The dist. cut is used to ensure the entire γ-ray image is recorded in the camera. At high dist. values, the γ-ray image may lie on the edge of the camera, and part of the image may be truncated. This makes parametrising the image difficult and can lead to a poorly reconstructed arrival direction. More details on these and other, H.E.S.S. parameters can be found in Aharonian *et al.* (2006b).

6.3.3 Further Data Processing

Reduction of the H.E.S.S. stereoscopic data is performed in two stages. The initial pre-processing is done at the Max-Planck-Institut für Kernphysik (MPIK) in Heidelberg, Germany, then further post processing is completed by the end user locally. The pre-

[2]The H.E.S.S. telescope PSF is approximately Gaussian with a 68% containment radius of 0.1°

processing performs the event by event stereoscopic reconstruction and writes the data into a series of run files. From these run files additional post processing is required to produce γ-ray skymaps and spectra.

`Dstanalyse`

The `Dstanalyse` software is used for post processing. The software written in the *C* framework by Gavin Rowell, is used to apply data selection cuts and apply CR background rejection cut. Ultimately, `Dstanalyse` determines the 'excess counts', the number of γ-ray events above the background CR events. The background rejection process performs some form of an ON source and OFF source subtraction similar to that seen in § 3.1.5. Multiple background rejection methods (e.g. ring, reflected-ring, ring-segment, template) are available. Usually the template background rejection method (Rowell, 2003) is applied. The template method takes all events failing the image shape cuts (§ 6.3.2), but with reconstructed directions overlapping the region of interest. In this way, the template background provides the local CR background level in the direction of the region of interest.

A γ-ray skymap is a point-by point integration of the excess counts from within the field of view of the telescope (FoV). To produce a skymap, `Dstanalyse` bins the FoV into a two dimensional histogram and determines the excess counts of γ-ray events with a reconstructed arrival direction, in sky co-ordinates, within a radius, θ, of each bin. Once the excess counts are determined, the statistical significance of the emission is determined via the methods of Li & Ma (1983, Equation 17). The `Dstanalyse` method of producing a skymap is indicated in Figure 6.14. The results of the `Dstanalyse` skymap production are written in an ASCII format ready to be plotted to produce the final γ-ray skymaps and spectra. The actual plotting of the data is performed in `PAW`, and .FITS files are created using the FTOOLS[3] package.

`PAW`

The Physics Analysis Workstation[4], `PAW`, is based on the *CERN Program Library* and is the precursor to `ROOT`. It was conceived to assist particle-physicists with the analysis and presentation of data. The `Dstanalyse` program has been written to supply its output data in a format that can be read and plotted by `PAW`. Additional `PAW` routines

[3]See `http://heasarc.nasa.gov/ftools/ftools_menu.html` for more information of the High Energy Astrophysics Science Archive Research Centre (HEASARC) FTOOLS package.

[4]See `http://wwwasd.web.cern.ch/wwwasd/paw/` for more information on the `PAW` software package.

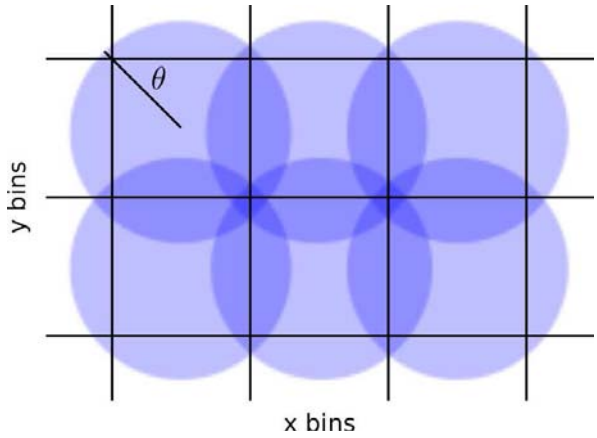

Figure 6.14: A schematic indicating how `Dstanalyse` produces a γ-ray skymap. The field of view of the telescope is binned into a two dimensional histogram and the excess counts from within a radius θ (blue shaded regions) from the 'test position' are integrated and stored in the bin. The significance of the excess counts is then determined for each bin via the methods of Li & Ma (1983, Equation 17). As can be seen from the overlapping circles (and darker shaded blue regions), the excess in each bin is not completely independent of the neighbouring bins.

have been constructed to plot skymaps of TeV emission, plot energy spectra and provide statistics on the results.

6.4 Microquasars

The following sections provide a background into the microquasar class of objects. Astrophysical jets, the classification of microquasars, and the first discovered microquasar, SS 433, are introduced. A review of the three X-ray binaries (possibly microquasars) detected with TeV γ-ray emission is also presented.

6.4.1 Astrophysical Jets

The discovery of astrophysical jets is credited to Curtis (1918) for the discovery of an optical jet from M87; a galaxy in the Virgo Cluster. The term 'jets' was refined by Bridle & Perley (1984), referring to collimated ejecta with opening angles $< 15°$. Since then jets have been discovered in many astrophysical systems within our Galaxy. It has been shown that young stars (Reipurth & Bertout, 1997), nuclei of planetary nebulae (López *et al.*, 1997) and accreting white dwarf stars (Motch, 1998; Cowley *et al.*, 1998) all have jets.

Although jets are a somewhat common phenomenon, the aforementioned sources only produce jets with non-relativistic velocities ($v \sim 10^2$–$10^4\,\mathrm{km\,s^{-1}}$), with thermal

methods attributed to the process. Microquasars, on the other hand, are able to produce jets with relativistic velocities ($v \geq 0.1\,c$).

When accreting matter falls onto the compact object of a microquasar, a large amount of energy needs to be released. Relativistic jets are nature's efficient manifestation of large scale energy transport. However, the mechanisms of jet formation and the propagation of matter along the jet remain enigmas. Further observations of jets are essential to answer fundamental questions of jet physics, such as, "How are jets collimated - to what extent are magnetic fields involved?" or "Are jets purely accretion powered or can jets extract energy from the rotation of a black hole?" A review of X-ray jet observations from Galactic black hole candidates, promoting many motivations for further study of jets, is presented by Kaaret *et al.* (2004).

6.4.2 Classification of Quasars and Microquasars

In astrophysics, a quasar (quasi-stellar radio source) refers to a very energetic, and distant, active galactic nucleus. Quasars were initially thought to be stars as they appeared point-like, unlike a galaxy which appears extended. It is now believed that quasars are the compact matter halos of super-massive black holes at the centre of young galaxies. Quasars are detectable across the entire EM spectrum, but can be essentially categorised by three components: a compact object, an accretion disk and a relativistic jet.

In the early 1990s, after two extremes of the EM spectrum were measured, radio and hard X-rays, a new class of objects was discovered to produce relativistic jets. A microquasar is a subset of Galactic X-ray binary objects which are radio loud. They are sometimes referred to as radio-jet-X-ray binaries to distinguish them from regular X-ray binary systems. These properties make them a smaller version of a quasar. Of course, quasars are extremely energetic, have super-massive black holes ($10^6\,\mathrm{M}_\odot$) and have relativistic jets extending millions of light years. Microquasars on the other hand, have stellar-mass black holes ($<10\,\mathrm{M}_\odot$) and have relativistic jets extending several light years. However, both systems are powered by black holes and potentially neutron stars. This means they are governed by the same physical processes, albeit on different physical- and time- scales. Therefore, variations which may take thousands of years in a quasar may happen in several minutes in a microquasar (Sams *et al.*, 1996; Rees, 1998). Microquasars are thus a very interesting class of objects and are especially useful in understanding the formation of jets and jet evolution, since the variability of an individual jet can be studied in detail.

According to van Paradjis (1995), there are approximately 200 X-ray binaries in

our Galaxy. Of these, ∼10% are radio loud resulting in approximately 20 microquasars in the Galaxy. Roughly two thirds of the microquasars are low mass X-ray binaries (LMXRB) which contain low mass A type stars similar to our Sun. The remaining are categorised as high mass X-ray binaries (HMXRB) which contain $> 10\,M_\odot$ O or B type stars.

6.4.3 The First of the Microquasar Class, SS 433

SS 433 was first catalogued in a survey of new Hα stars in the Milky Way as one of many emission line objects with strong Hα lines (Stephenson & Sanduleak, 1977). Radio emission (Clark *et al.*, 1975) and X-ray emission (Forman *et al.*, 1978) were detected independently. However, no optical counterpart was initially detected in either case. It was recognised by Clark & Murdin (1978) that all three emissions (Hα, radio and X-Ray) were coming from the vicinity of the SNR W50.

For more than a decade, SS 433 was the only known object of its class in our Galaxy (Margon, 1984). This is mostly due to the fact that SS 433 is unusual as it has broad emission lines and it is bright in visible wavelengths. SS 433 was particularly confusing as further study revealed broad emission lines at unfamiliar wavelengths (Mammano *et al.*, 1980). These were realised to be Doppler shifted Balmer and He I lines with simultaneous strong Doppler red and blue shifting (Liebert *et al.*, 1979; Margon *et al.*, 1979). Two of the first theoretical papers on the SS 433 system propose the most likely mechanism for the observed Doppler shifting; that there are two opposed collimated jets (Fabian & Rees, 1979; Milgrom, 1979).

The binary system SS 433 consists of a high mass star, of spectral classification A3-7 I with mass $12.3 \pm 3.3 M_\odot$ (Hillwig *et al.*, 2004), and a compact object with mass $4.3 \pm 0.8\,M_\odot$ (Hillwig & Gies, 2008). This mass estimate still leaves uncertainty whether the compact is a neutron star or a black hole. One possible way to determine the nature of the compact object is to determine the cause for the Doppler shifted emission lines, as different proposed jet mechanisms require particular types of compact object. For example, the proposed 'nozzle' method would favour a neutron star scenario (Begelman & Rees, 1984).

6.4.4 Potential Microquasars with Detected VHE γ-Ray Emission

Several systems containing compact objects have been identified as VHE γ-ray sources (e.g. Aharonian *et al.* 2005a,b; Albert *et al.* 2006, 2007). Currently, the majority of

these systems is thought to contain a neutron star as the compact object. Many of the recently discovered Galactic VHE γ-ray sources are connected with Pulsar Wind Nebulae (PWN), where the γ-rays are produced by the Inverse Compton (IC) scattering of low energy photons by relativistic electrons accelerated by the pulsar wind termination shock (Gaensler & Slane, 2006). The best example of a PWN is the Crab Nebula (Figure 1.2) which is a well measured standard source[5] for TeV gamma rays (Weekes *et al.*, 1989).

The following paragraphs contain a brief summary of the microquasars (and microquasar candidate PSR B1259-63) which have been detected emitting VHE γ-rays to date (except Cygnus X-1, discussed later):

- **Candidate PSR B1259-63:**
  PSR B1259-63 is a perfect example of a classical radio pulsar orbiting a massive star. This makes PSR B1259-63 a radio-loud X-ray binary. The absence of jets calls into question the classification of this object as a microquasar, hence the 'candidate' title. In this system, a millisecond pulsar is orbiting a B2 e type star in an eccentric orbit (Johnston *et al.*, 1992a,b) and is estimated to be at a distance 1.5 kpc (Johnston *et al.*, 1996). The high magnetic field of the pulsar seems to prevent accretion onto the pulsar, negating the formation of jets. The pulsar itself has a strong pulsar-wind which is interacting with the stellar wind to produce a termination shock. At this shock, high energy electrons IC scatter soft photons to multi-TeV energies. For detailed results and a discussion of the VHE emission see Aharonian *et al.* (2005a)

- **LS 5039:**
  LS 5039 is one of two GeV sources catalogued by EGRET (Hartman *et al.*, 1999) which are positionally coincident with a microquasar. The LS 5039 system contains a compact object of unknown nature, with mass $< 5\,M_\odot$ orbiting an O 6.5V((f)) type star (Clark *et al.*, 2001) at a distance of 2.5 kpc (Casares *et al.*, 2005). VHE γ-ray emission was detected (Aharonian *et al.*, 2005b), confirming that particle acceleration up to at least TeV energies is possible. In the absence of knowing the nature of the compact object, the mechanism for the observed VHE emission remains a mystery. Radio emission, detected in the form of jets, has been presented in Paredes *et al.* (2000), hinting that LS 5039 is an accretion powered system. However, the PWN scenario is proposed as the most likely mechanism for the observed VHE emission (Dubus *et al.*, 2008).

[5] Although recent observations may indicate some variability in the MeV γ-ray emission from the Crab Nebula (Abdo *et al.*, 2011).

- **LSI +61 303:**
  LSI +61 303 is the second of the two GeV sources catalogued by EGRET (Hartman *et al.*, 1999) which are positionally coincident with known microquasars. The system is at a distance of 2 kpc and consists of a B e type star (Frail & Hjellming, 1991) and an orbiting neutron star as the compact object (Hutchings & Crampton, 1981). The detection of precessing radio jets (Massi *et al.*, 2001) provides evidence that this is an accretion powered system. As LSI +61 303 is a northern-hemisphere source it was targeted for VHE observations by MAGIC. Periodic γ-ray emission was detected (Albert *et al.*, 2006), following that seen in the other EGRET source LS 5039 by H.E.S.S. (Aharonian *et al.*, 2005b). The γ-ray production mechanism is unclear. Both hadronic (e.g Romero *et al.* 2003) and leptonic (e.g. Atoyan & Aharonian 1999) emission scenarios have been proposed and discussed.

6.5 ISM Interacting Microquasars Targeted for TeV γ-Ray observations

The following paragraphs provide a summary and motivation for studying Circinus X-1, Cygnus X-1 and 4U 1755-33. In all three cases, these microquasars have been shown to be interacting with the ISM and, like the W28 SNR, fall into the core theme of this thesis. Additionally, these microquasars all display high energy phenomena, indicating TeV γ-ray emission is quite possible.

- **Circinus X-1:**
  Circinus X-1 (Cir X-1) is an unusual low mass X-ray binary system (LMXRB). The detected ultra-relativistic particle flows, similar to those produced by active galactic nuclei (AGN) (Fender *et al.*, 2004), coupled with its rapid variability suggested that the compact object was a black hole (Toor, 1977). The detection of type I X-ray bursts (Tennant *et al.*, 1986a,b) strongly suggest the compact object is an accreting neutron star. The neutron star, with mass estimated to be $2\,M_\odot$ (Boutloukos *et al.*, 2006), is orbiting the stellar companion, suggested to be a B5 A0 supergiant (Jonker *et al.*, 2007) with mass $3 < M < 10\,M_\odot$ (Johnston *et al.*, 1999; Jonker *et al.*, 2007), with an orbital period of 16.6 days (Jonker *et al.*, 2007). The distance to the system is not well known, with distance estimates placing it 4 – 10 kpc away (Goss & Mebold, 1977; Iaria *et al.*, 2005). The system is surrounded by a diffuse radio nebula $\sim 5'$ (Haynes *et al.*, 1986), powered by the interaction between the relativistic jets and the ISM (Stewart *et al.*, 1993; Tudose

et al., 2006). The jets have been recently detected as X-ray jets and the power in the jets has been placed in the 10^{35} – $10^{37}\,\mathrm{erg\,s^{-1}}$ range (Sell *et al.*, 2010), which over the jets total lifetime, $< 10^5\,\mathrm{yr}$, suggests that $> 10^{48}\,\mathrm{erg}$ has been deposited into the ISM. The small line of sight angle between the observer and the jet, less than 5° (depending on the assumed distance), suggests this system is a microblazar (Tudose *et al.*, 2006). Given the corollaries between AGN (blazars) and this microblazar, the Cir X-1 system is a strong candidate for VHE γ-ray emission.

- **Cygnus X-1:**
  Cygnus X-1 (Cyg X-1) is one of the few microquasars categorised as a high mass X-ray binary system (HMXRB). The system consists of a black hole, with estimated mass $21\,\mathrm{M_\odot}$, orbiting an O 9.7 Iab companion star, with estimated mass $40\,\mathrm{M_\odot}$ (Ziółkowski, 2005). The system is suspected to be in a circular orbit, with orbital period 5.6 days (e.g. Brocksopp *et al.* 1999 and references therein) and at a distance of 2 kpc (e.g. Ziółkowski 2005 and references therein). The Cyg X-1 system displays variable X-ray emission and displays the corresponding 'low/hard' and 'high/soft' spectral states depending on the accretion rate (Esin *et al.*, 1998). Through VLBA imaging, the existence of a highly collimated, 0.2° opening angle, and elongated radio jet, approximately 15 mas (milli arc seconds) in length, has been revealed (Stirling *et al.*, 2001). Daily monitoring of the X-ray flux from Cyg X-1 over the past decade confirms Cyg X-1 has remained in the 'hard'[6] state, powering the collimated jet. This jet is interacting with the ISM, blowing out a bubble, $\sim 5\,\mathrm{pc}$ diameter (Gallo *et al.*, 2005), and creating a termination shock which could provide favourable conditions for particle acceleration. The total power in the jet is the order of 10^{35} – $10^{37}\,\mathrm{erg\,s^{-1}}$, which over the jets lifetime, 0.02 – 0.32 Myr (Myr = $10^6\,\mathrm{yr}$), has deposited $\sim 7 \times 10^{48}\,\mathrm{erg}$ into the surrounding ISM (Gallo *et al.*, 2005). It has been suggested by Romero *et al.* (2002) that Cyg X-1 is also a microblazar and observations of Cyg X-1 in soft γ-rays (McConnell *et al.*, 2002; Cadolle Bel *et al.*, 2006) strongly suggest there is a higher energy non-thermal component. This has since been confirmed with recent *AGILE* MeV detections (Bulgarelli *et al.*, 2010; Sabatini *et al.*, 2010) as well as a $4\,\sigma$ GeV flare detected by the *MAGIC* telescope system (Albert *et al.*, 2007).

[6] In the 'hard' state the X-ray emission is categorised by a power-law with spectral index, Γ, in the $1.4 < \Gamma < 1.9$ range.

- **4U 1755-33:**
  4U 1755-33 is a peculiar LMXRB. It was a persistent X-ray source since its discovery in 1970 (Giacconi *et al.*, 1974), until in 1996 the X-ray emission essentially switched-off (Roberts *et al.*, 1996). The nature of the compact object is unknown, however, the orbital period is 4.4 days (White *et al.*, 1984). The soft X-ray spectrum with the presence of a hard tail (White *et al.*, 1984; White & Marshall, 1984; Pan *et al.*, 1995) is similar to those seen towards other black holes. The detection of 'fossil' X-ray jets (Angelini & White, 2003) with spectra similar to those of other accreting black holes is further proof supporting the black hole candidacy. However, a neutron star compact object cannot be ruled out (e.g Seon *et al.* 1995 and references therein). The 'fossil' X-ray jets are themselves a rare feature, X-ray jets[7] are exhibited in only three other X-ray binaries, XTE J1550-564 (Corbel *et al.*, 2002) and H 1743-322 (Corbel *et al.*, 2005) and Cir X-1 (Sell *et al.*, 2010). The ~ 7 arc minute 'fossil' jets extend in both directions from the source, and with the assumed distance to the system 4 – 9 kpc (McClintock *et al.*, 1978; Wachter & Smale, 1998), the jets are 3 – 8 pc in diameter (Angelini & White, 2003). Archival 21 cm and 6 cm radio data fail to detect any radio counterpart, although, these observations would not be sensitive to large scale (arc minute) structures (Kaaret *et al.*, 2004). A discussion of the origin of the X-ray emission, presented in (Kaaret *et al.*, 2004, 2006), rules out Bremsstrahlung and Inverse Compton for the origin and concludes synchrotron is the likely X-ray emission mechanism. In this case, electrons with energies ~ 60 TeV are required with a minimum total energy of 10^{44} erg. These VHE electrons could comfortably produce γ-ray emission at multi-TeV levels through Inverse Compton scattering.

[7] although there is evidence for X-ray lobes at the ends of the jets but not the jets themselves in SS 433.

6.6 H.E.S.S. Observations towards Circinus X-1, Cygnus X-1 & 4U 1755-33

The summary of the TeV γ-ray observations towards microquasars interacting with the ISM is presented in:

- Nicholas B., & Rowell G., 2008, American Institute of Physics (AIP) Conf. Proc., 1085, 245.

Abstract:
A number of microquasars exhibit parsec-scale jets, which in some cases are known to interact with the interstellar medium (ISM). A famous example is the SS-433 system. Here, we summarise H.E.S.S. observations of three further examples in this category with arc-minute scale jets and/or jet/ISM interaction features. The small line-of-sight angle in the Cir X-1 jet makes this source a potential 'microblazar'. An arc-minute bow-shock radio feature has been blown out by the Cyg X-1 jet, and the MAGIC telescope has also detected a VHE flare on 24 Sept. 2006 from Cyg X-1 (H.E.S.S. obs. were taken $\sim$1 month earlier). Persistent bi-lobal ($\sim$7 arcmin long) 'fossil' jets of 4U1755-33 have been seen in X-rays. This report summarises our observations, searching for pointlike VHE emission at the central sources and for extended emission from their jets and/or jet/ISM interaction regions.

CHAPTER VII

Final Remarks.

The work presented in this thesis has been a multi-wavelength study of high energy objects interacting with the ISM. The majority of the work has been aimed towards understanding the distribution of dense molecular material towards the supernova remnant W28. The method used to determine the properties of the dense gas in this complex and diverse environment was to conduct multi-wavelength molecular line surveys of the molecular clouds in the W28 field. Molecular line data were collected using the Mopra millimetre-wave telescope in multiple observation seasons, from 2008 – 2010.

In Chapter 3, the results of 12 mm molecular line observations towards the four TeV γ-ray sources were presented. Using the 23 GHz NH_3 inversion transitions, the broad scale ($\sim$ 1.5° square) distribution of the 'cool', quiescent, dense gas throughout the W28 field was revealed. The NH_3 molecule allows the optical depth, column density and temperature of the gas to be determined and estimates of the total mass and density for these dense clumps were presented. Two standout features revealed by these observations were the shocked north-eastern (NE) cloud (Core 2 / HESS J1801-233) and the HII complex G5.89-0.39 (Triple Core SE and Central / HESS J1800-240 B). The NH_3 observations revealed the dense portion of the shocked NE cloud. Broad line widths and detections of NH_3 (3,3) & (6,6) indicate this region is turbulent and disrupted. The broad line width of the NH_3 (3,3) line towards the NE cloud, and its high line strength compared to the NH_3 (2,2) and NH_3 (1,1) lines, suggested that a large amount of non-thermal energy has been deposited into the cloud. The velocity dispersion of the NH_3 lines revealed that the direction of the disruption was from the W28 side of the cloud, suggesting the W28 SNR shock is disrupting the cloud.

The 12 mm observations were followed up in a broad scale 7 mm line survey of the W28 TeV γ-ray sources, taking advantage of the smaller beam size to probe the dense gas at arc minute scales. In Chapter 4 the results of the 7 mm observations were presented. Using the CS (1-0) transition the broad scale 'cool to warm' dense gas in the W28 field was revealed. Observations of CS isotopologues also allow an estimation of the mass and density of the dense gas. Additionally, sites of shocks, outflows and disrupted gas were revealed with SiO emission. These shocked regions

were typically associated with star formation cores, although, a detection towards the NE cloud further confirms that the W28 SNR shock has disrupted the cloud. A detailed discussion of the X-ray, γ-ray and molecular gas morphology towards the NE cloud was presented, and theoretical CR propagation and cloud diffusion models were summarised and discussed. The γ-ray emission towards the NE cloud (HESS J1801-233) is most likely hadronic and the high energy CRs are able to penetrate some distance into the dense cloud core.

Additional deep 12 mm observations towards the NE cloud (HESS J1801-233) were performed to provide detailed NH_3 spectra, in multiple inversion transitions, across the entire dense cloud core. These results were presented in Chapter 5. A determination of the physical gas parameters on a pixel-by-pixel basis revealed a temperature and density gradient across the dense cloud core, peaking at the disrupted W28 side of the cloud. The repeated analysis of gas parameters and velocity dispersion distributions were all consistent with the earlier findings presented in Chapter 3.

A TeV γ-ray study of microquasars interacting with the ISM, searching for point-like and extended TeV γ-ray emission, has been presented. This study was conducted using data collected by the H.E.S.S. telescope system from 2004 – 2008. These results were presented in Chapter 6. Towards all three of the ISM interacting microquasars, no significant TeV γ-ray emission was seen in H.E.S.S. data. Upper-limits to the TeV flux were set and discussed.

7.1 Future Work

These observations set groundwork for future observations, specifically for future TeV γ-ray work. A major limiting factor with the γ-ray results is the relatively poor resolution, compared to that of the molecular line observations. Here, the distribution of the dense gas has been determined with 1 – 2 arc minute resolution, while the γ-rays can only be probed at 6 arc minute resolution. Of course with the use of interferometry, the molecular gas distribution can be probed in much higher (sub-arc minute) detail. However, at this stage, such detail would be unnecessary for comparisons with current TeV γ-ray emission. But there are good reasons for higher resolution studies of the molecular gas in the NE clouds to understand further the shocked NE cloud. Future TeV instrumentation, such as the Cherenkov Telescope Array (CTA), with improved angular resolution ($\sim 1-2$ arc minute) will be able to probe the γ-ray morphology and spectra on comparable spatial scales to that of the molecular gas. Together, high resolution TeV γ-ray observations and these molecular gas observations can help provide constraints on theoretical CR diffusion and propagation modelling.

Radiative transfer modelling of the NE cloud presented in Chapter 3 could be updated using spectral data from the deep NH_3 observations presented in Chapter 5.

The TeV γ-ray study was based on very limited data sets ($\sim$ 4 hr towards both Cyg X-1 and 4 U1755-33). Although more observation time would only improve the situation, based on the orbital dependance of emission (Cir X-1) and the detected γ-ray flare (Cyg X-1) it would appear that observations of these sources would have to be at the 'right time'. With this in mind, target of opportunity (ToO) observations would be the way to go, triggered by activity at other wavelengths (e.g. radio and X-ray).

APPENDIX A

Hillas Parameters: A mathematical description

A.1 Size

In an image of a γ-ray shower, each pixel corresponds to an individual photomultiplier tube in the camera. By counting the total number of photo-electrons in all the PMTs, each with signal s_i, gives the size, S, of the image:

$$S = \sum_i s_i \tag{A.1}$$

A.2 Centre of Gravity

The centre of gravity (CoG) determined from a weighted mean of the coordinates $\langle x \rangle$ and $\langle y \rangle$. These coordinates are determined by the number of photo-electrons in each individual PMT, weighted by its position in the camera. Suppose the i_{th} PMT is given the coordinates (x_i, y_i) and registers a signal s_i, then:

$$\langle x \rangle = \frac{\sum_i s_i x_i}{\sum_i s_i} \quad \text{and} \quad \langle y \rangle = \frac{\sum_i s_i y_i}{\sum_i s_i} \tag{A.2}$$

A.3 Length and Width

The parameters of length and width correspond to the major and minor axes of the ellipse respectively. To calculate the length and width, the weighted mean in x^2, y^2 and xy must be found, that is $\langle x^2 \rangle$, $\langle y^2 \rangle$ and $\langle xy \rangle$:

$$\langle x^2 \rangle = \frac{\sum_i s_i x_i^2}{\sum_i s_i}, \quad \langle y^2 \rangle = \frac{\sum_i s_i y_i^2}{\sum_i s_i}, \quad \langle xy \rangle = \frac{\sum_i s_i x_i y_i}{\sum_i s_i} \tag{A.3}$$

From these, the second order covariance matrix, C, is calculated from the individual variance, σ^2, in each x, y and xy:

$$C = \begin{pmatrix} \sigma_x^2 & \sigma_{xy} \\ \sigma_{xy} & \sigma_y^2 \end{pmatrix} \tag{A.4}$$

where:

$$\sigma_x^2 = \langle x^2 \rangle - \langle x \rangle^2, \quad \sigma_y^2 = \langle y^2 \rangle - \langle y \rangle^2, \quad \sigma_{xy} = \langle xy \rangle - \langle x \rangle \langle y \rangle$$

This leads to the parameters of length (L) and width (W):

$$L = \sqrt{\frac{1}{2}\mathrm{Tr}(C) + \sqrt{\frac{1}{4}\mathrm{Tr}(C)^2 - \det(C)}} \tag{A.5}$$

$$W = \sqrt{\frac{1}{2}\mathrm{Tr}(C) - \sqrt{\frac{1}{4}\mathrm{Tr}(C)^2 - \det(C)}} \tag{A.6}$$

where $\mathrm{Tr}(C)$ is the trace of the matrix C and $\det(C)$ is the determinant of the matrix C, given by $\mathrm{Tr}(C) = \sigma_x^2 + \sigma_y^2$ and $\det(C) = \sigma_x^2\,\sigma_y^2 - \sigma_{xy}^2$

Bibliography

Abdo A.A., Ackermann A., Ajello M., *et al.* (Fermi Collab.), 2010, ApJ, 718, 348.

Abdo A.A., Ackermann A., Ajello M., *et al.* (Fermi Collab.), 2011, Science, 331, 739.

Aharonian F., 1991, Ap&SS, 180, 305.

Aharonian F.A. & Atoyan A.M., 2000, A&A, 362, 937.

Aharonian F.A., 2004, Very high energy cosmic gamma radiation: a crutial window on the extreme Universe, River Edge, NJ, World Scientific Publishing.

Aharonian F., Akhperjanian A.G., Aye K.-M., *et al.* (H.E.S.S. Collab.), 2005a, A&A, 442, 1.

Aharonian F., Akhperjanian A.G., Aye K.-M., *et al.* (H.E.S.S. Collab.), 2005b, Science, 309, 746.

Aharonian F., Akhperjanian A.G., Bazer-Bachi A.R., *et al.* (H.E.S.S. Collab.), 2006a, A&A, 449, 223.

Aharonian F., Akhperjanian A.G., Bazer-Bachi A.R., *et al.* (H.E.S.S. Collab.), 2006b, A&A, 457, 899.

Aharonian F., Akhperjanian A.G., Bazer-Bachi A.R., *et al.* (H.E.S.S. Collab.), 2007, 467, 1075.

Aharonian F., Akhperjanian A.G., Bazer-Bachi A.R., *et al.* (H.E.S.S. Collab.), 2008b, A&A, 481, 401.

Albert J., Aliu E., Anderhub H., *et al.* (MAGIC Collab.), 2006, Science, 312, 1771.

Albert J., Aliu E., Anderhub H., *et al.* (MAGIC Collab.), 2007, ApJ, 665, L51.

Aliu E., Anderhub H., Antonelli L.A., 2008, Science, 322, 1221.

Angelini L., & White N.E., 2003, ApJ, 586, L71.

Atoyan A.M. & Aharonian F.A., 1999, MNRAS, 302, 253.

Axford W.I., Leer E. & Skadron G., 1977, Proc. 15th Int. Cosmic Ray Conf., 11, 132.

Barrett A.H., Ho P.T.P. & Myers P.C., 1977, ApJ, 211, L39.

Bell A.R, 1978, MNRAS, 182, 147.

Begelman M.C. & Rees M.J., 1984, MNRAS, 206, 209.

Benaglia P. & Romero G.E., 2003, A&A, 399, 1121.

Berge D., PhD Thesis, A Detailed study of the Gamma Ray Supernova remnant RX J1713.7-3946 with H.E.S.S., 2006, Ruperto-Carola University of Heidelberg.

Bergin E.A., Maret S., Floris F.S., *et al.*, 2006, ApJ, 645, 369.

Bernlöhr K., 2000, Astroparticle Physics, 12, 255.

Blandford R.D. & Ostriker J.P., 1978, ApJ, 22, L29.

Bloemen H., Wijnands R., Bennett K., *et al.*, 1994, A&A Letters, 281, L5.

Blumenthal G.R. & Gould R.J., 1970, Rev. Mod. Phys., 42:2, 237.

Bonnell I.A., Bate M.R. & Zinnecker H., 1998, MNRAS, 298, 93.

Boutloukos S., van der Klis M., Altamirano D., *et al.*, 2006, ApJ, 653, 1435.

Bulgarelli A., Pittori C., Lucarelli F., *et al.*, 2010, The Astronomer's Telegram, #2512.

Bridle A.H. & Perley R.A., 1984, Ann. Rev. Astron. Astrophys. 22, 319

Brocksopp C., Fender R.P., Larionov V., *et al.*, 1999, MNRAS, 309, 1063.

Brogan C.L., Gelfand J.D., Gaensler B.M., *et al.*, 2006, ApJ, 639, L25.

Cadolle Bel M., Sizun P., Goldwurm A., *et al.*, 2006, A&A, 446, 591.

Casares J., Ribó M., Ribas I., *et al.*, 2005, MNRAS, 364, 899.

Ceccarelli C., Loinard L., Castets A., *et al.*, 2000, A&A Letters, 357, L9.

Cernicharo J., 1991, in Lada C.J., Kylafis N.D., Eds, NATO ASIC Proc. 342: The Physics of Star Formation and Early Stellar Evolution, 287.

Cheung A.C., Rank D.M., Townes C.H., *et al.*, 1968, Phys. Rev. Lett. 21:15, 1701.

Clark D.H., Green A.J. & Caswell J.L., 1975, Australian Journal of Physics Astrophysical Supplement, 37, 75.

Clark D.H. & Murdin P., 1978, Nature, 276, 45.

Clark J.S., Reig P., Goodwin S.P, *et al.*, 2001, A&A, 376, 476.

Corbel S., Fender R.P., Tzioumis A.K., *et al.*, 2002, Science, 298, 196.

Corbel S., Kaaret P., Fender R.P., *et al.*, 2005, ApJ, 632, 504.

Cowley A.P, Schmidtke P.C, Crampton D. & Hutchings J.B., 1998, ApJ, 504, 854.

Crutcher R.M., 1991, ApJ, 520, 706.

Curtis H.D., 1918, Publications of Lick Observatory, 13, 9.

Dermer C.D., 1986, A&A, 157, 223.

Dubner G.M., Velázquez P.F., Goss W.M. & Holdaway M.A., 2000, AJ, 120, 1933.

Dubus G., Ceretti B. & Henri G., 2008, A&A, 477, 691.

Elitzur M., 1992, Astrophysical Masers, Kluwer Academic Publishers, The Netherlands.

Esin A.A., Narayan R., Cui W., *et al.*, 1998, ApJ, 505, 854.

Esposito J.A., Hunter S.D., Kanbach G. & Sreekumar P., 1996, ApJ, 461, 820.

Fabian A.C. & Rees M.J., 1979, MNRAS, 187, 13.

Fender R., Wu K., Johnston H., *et al.*, 2004, Nature, 427, 222.

Fermi E., 1949, Phys. Rev., 75:8, 1169.

Forman W., Jones C., Cominsky L., *et al.*, 1978, ApJ SS, 38, 357.

Frail D.A. & Hjellming R.M., 1991, AJ, 101:6, 2126.

Frank I. & Tamm I., 1937, Dokl. Akad. Nauk. S.S.S.R., 14, 109.

Fuente A., Neri R. & Caselli, P., 2005, A&A, 444, 481.

Fukui Y., *et al.*, (Nanten Collab.), 2008, AIP Conf. Proc., 1085, 104.

Funk S., Master's Thesis, Hadron Suppression using Wavelet Transformations for the H.E.S.S Telescope System, 2002, Humboldt-Universität zu Berlin.

Gabici S., Aharonian F.A. & Blasi P., 2007, Astrophys. Space Sci., 309, 365.

Gaensler B.M. & Slane P.O., 2006, Ann. Rev. Astron. Astrophys., 44, 17.

Gallo E., Fender R.P., Kaiser C., *et al.*, 2005, Nature, 436, 819.

Garay G. & Lizano S., 1999, PASP, 111, 1049.

Giacconi R., Murray S., Gursky H., *et al.*, 1974, ApJ SS, 27, 37.

Giuliani A., Tavani M., Bulgarelli A., *et al.*, (AGILE Collab.), 2010, A&A Letters, 516, L11.

Goldsmith P.F. & Langer W.F., 1999, ApJ, 517, 209.

Goss W.M. & Mebold U., 1977, MNRAS, 181, 255.

Goudis C., 1976, Ap&SS, 40, 91.

Gusdorf A., Cabrit S., Flower D.R. & Pineau Des Forêts G., 2008a, A&A, 482, 809.

Gusdorf A., Pineau des Forêts G., Cabrit S & Flower D.R., 2008b, A&A, 490, 695.

Hartman R.C., Bertsch D.L., Bloom S.C., *et al.*, 1999, ApJ SS, 123, 79.

Haynes R.F., Komesaroff M.M., Little A.G., *et al.*, Nature, 1986, 324, 233.

Heitler W., 1954, The Quantum Theorey of Radiation, 3rd ed. Clarendon Press.

Helfand D.J., Gotthelf E.V., Halpern J.P., *et al.*, 2007, ApJ, 665, 1297.

Hess V.F., 1912, Physik. Zeitschrift, 13, 1084.

Hillas A.M., 1985, Proceedings of the 19th ICRC, La Jolla.

Hillwig T.C., Gies D.R., Huang W., *et al.*, 2004, ApJ, 615, 422.

Hillwig T.C. & Gies D.R., 2008, ApJ, 676, L37.

Hinton J.A. & Hofmann W., 2009, Ann. Rev. Astron. Astrophys., 47, 523.

Ho P.T.P., Martin R.N. & Barrett A.H., 1981, ApJ, 246, 761.

Ho P.T.P & Barrett A.H., 1980, ApJ, 273, 38.

Ho P.T.P. & Townes C.H., 1983, Ann. Rev. Astron. Astrophys., 21, 239.

Hofmann W., Jung I., Konopelko A., *et al.*, 1999, Astroparticle Physics, 12, 135.

Hutchings J.B. & Crampton D., 1981, PASP, 93, 486.

Iaria R., Spanó M., Di Salvo T., *et al.*, 2005, ApJ, 619, 503.

Jansky K., 1933, Nature, 132, 66.

Johnston S., Lyne A.G., Manchester R.N., *et al.*, 1992a, MNRAS, 255, 401.

Johnston S., Manchester R.N., Lyne A.G., *et al.*, 1992b, ApJ, 387, L37.

Johnston S., Manchester R.N., Lyne A.G., *et al.*, 1996, MNRAS, 279, 1026.

Johnston H.M., Fender R. & Wu K., 1999, MNRAS, 308, 415.

Jonker P.G., Nelemans G. & Bassa C.G., 2007, MNRAS, 374, 999.

Kaaret P., Corbel S., Tomsick J.A., *et al.*, 2004, Nuclear Physics B (Proc. Suppl.), 132, 354.

Kaaret P., Corbel S., Tomsick J.A., *et al.*, 2006, ApJ, 641, 410.

Kaspi V.M., Lyne A.G., Manchester R.N., *et al.*, 1993, ApJ, 409, L57.

Konopelko A., Lucarelli F., Lampeitl H, & Hofmann W., 2002, J. Phys. G: Nucl. Part. Phys., 28, 2755.

Kurtz S., Cesaroni R., Churchwell E., Hofner P. & Walmsley C.M., 2000, Protostars and Planets IV, 299.

Lefloch B., Cernicharo J. & Pardo J.R., 2008, A&A, 489, 157.

Li T. & Ma Y., 1983, ApJ, 272, 317.

Liebert J., Angel J.R.P., Hege E.K., *et al.*, 1979, Nature, 279, 384.

Longair M., 1994, High Energy Astrophysics: Volume 2 (Second Edition), Cambridge University Press.

López J.A., Meaburn J., Bryce M. & Rodriguez L.F., 1997, Proc. IAUS 180, 225.

Lozinskaya T.A., 1981, Sov. Astron. Lett., 7:1, 17.

Mammano A., Ciatti F. & Vittone A., 1980, A&A, 85, 14.

Margon B., Ford H.C., Grandi S.A. & Stone R.P.S., 1979, ApJ, 233, L63.

Margon B., 1984, Ann. Rev. Astron. Astrophys., 22, 507.

Martin R.N. & Ho P.T.P., 1979, A&A Letters, 74, L7.

Martin-Pintado J., de Vincente P., Rodríguez-Fernández N.J., *et al.*, 2000, A&A Letters, 356, L5.

Massi M., Ribó M., Paredes J.M., *et al.*, 2001, A&A, 376, 217.

McClintock J.E., Canizares C.R. & Backman D.E., 1978, ApJ, 223, L75.

McConnell M.L., Zdziarski A.A., Bennett K., *et al.*, 2002, ApJ, 572, 984.

McKee C.F. & Tan J.C., 2003, ApJ, 585, 850.

Milgrom M., 1979, A&A, 76, 338.

Mizuno A. & Fukui Y., 2004, AIP Conf. Proc., 317, 59.

Moderski R., Sikora M., Coppi P.S. & Aharonian F., 2005, MNRAS, 363, 954 and erratum 364, 1488.

Mori M., 1997, ApJ, 478, 225.

Motch C., 1998, A&A Letters, 338, L13.

Motogi K., Sorai K., Habe A., *et al.*, 2011, PASJ, 63, 31.

Nakashima Y., Kawamura A., Yamamoto H., *et al.*, 2008, In Proc. 4$^{\rm th}$ Heidelberg Gamma-Ray Symp.

Pacholczyk A.G., 1970, Radio Astrophysics, W.H. Freeman and Company, San Francisco.

Pan H.C., Skinner G.K., Sunyaev R.A. & Borozdin K.N., 1995, MNRAS, 274, L15.

Paredes J.M., Marti, J., Ribó M. & Massi M., 2000, Science, 288, 2340.

Pittard J.M. & Dougherty S.M., 2006, MNRAS, 372, 801.

Pollock A.M.T., 1985, A&A, 150, 339.

Purcell C., PhD Thesis, What's in the brew? A study of the molecular environment of methanol masers and UCHII regions, 2006, University of New South Wales.

Rees M.J., 1998, Black Holes and Relativistic Stars. Ed. Robert M.W., Chicago, University of Chicago Press.

Reimer A., Pohl M. & Reimer O., 2006, ApJ, 664, 1118.

Reipurth B. & Bertout C., 1997, IAU Symposium No. 182. pg. 309.

Rho J. & Borkowski K.J., 2002, ApJ, 575, 201.

Rho J. & Petre R., 1998, ApJ, 503, L167.

Ripken J., Beilicke M., Heinzelmann G. & Horns D., 2008, Proc. 30$^{\text{th}}$ ICRC, Mexico, 2, 795.

Roberts M.S.E., Michelson P.F., Cominsky L.R., *et al.*, 1996, IAU Circ. 6302.

Rohlfs K., 1986, Tools of Radio Astronomy, Springer-Verlag Berlin Heidelberg.

Romero G.E., Kaufman Bernadó M.M. & Mirabel I.F., 2002, A&A Letters, 393, L61.

Romero G.E., Torres D.F., Kaufman Bernadó M.M. & Mirabel I.F., 2003, A&A Letters, 410, L1.

Rowell G.P., 2003, A&A, 410, 389.

Rydbeck O.H.E., Sume A., Hjalmarson Å., *et al.*, 1977, ApJ, 215, L35.

Sabatini S., Striani E., Verrecchia F., *et al.*, 2010, The Astronomer's Telegram, #2715.

Sams B.J., Eckart A. & Sunyaev R., 1996, Nature, 382, 47.

Schilke P., Walmsley C.M., Pineau Des Forêts G. & Flower D.R., 1997, A&A, 321, 293.

Sell P.H., Heinz S., Calvelo D.E., *et al.*, 2010, ApJ Letters, 719, L194.

Seon K., Min K., Yoshida K., *et al.*, 1995, ApJ, 454, 463.

Spitzer L., 1978, Physical Processes in the Interstellar Medium, Wiley, New York.

Stahler S.W. & Palla F., 2005, The Formation of Stars, Wiley, New York.

Stecker F.W., 1971, Cosmic Gamma Rays, NASA-SP249, Washington D.C.

Stephenson C.B. & Sanduleak N., 1977, ApJ SS, 33, 459.

Stewart R.T., Caswell J.L., Haynes R.F. & Nelson G.J., 1993, MNRAS, 261, 593.

Stirling A.M., Spencer R.E., de la Force C.J., *et al.*, 2001, MNRAS, 327, 1273.

Sturner S.J. & Dermer C.D., 1995, A&A Letters, 293, L17.

Strömgren B., 1939, ApJ, 89, 526.

Tafalla M., Myers P.C, Caselli P., *et al.*, 2002, ApJ, 569, 815.

Tafalla M., Myers P.C., Caselli P. & Walmsley C.M., 2004, A&A, 416, 191.

Tennant A.F., Fabian A.C. & Shafer R.A., 1986a, MNRAS, 219, 871.

Tennant A.F., Fabian A.C. & Shafer R.A.,1986b, MNRAS, 221, 27p.

Tingay S.J., Murphy D.W. & Edwards P.G., 1998, ApJ, 500, 673.

Toor A., 1977, ApJ, 215, L57.

Townes C.H. & Schalow A.L., 1955, Microwave Spectroscopy, McGraw-Hill Book Company, Maple Press Company, York, PA.

Tudose V., Fender R.P., Kaiser C.R., *et al.*, 2006, MNRAS, 372, 417.

Ueno M., Bamba A. & Koyama K., 2003, proc. 28$^{\rm th}$ ICRC, 2401.

Ungerechts H., Walmsley C.M. & Winnewisser G., 1980, A&A, 88, 259.

Ungerechts H., Walmsley C.M. & Winnewisser G., 1986, A&A, 157, 207.

Urquhart J.S., Hoare M.G., Purcell C.R., *et al.*, 2010, PASA, 27, 321.

van Dishoeck E.F. & Blake G.A., 1998, Ann. Rev. Astron. Astrophys., 36, 317.

van Paradijs J., 1995, in X-Ray Binaries, ed. Lewin W.H.G., van Paradijs J. & van den Heuvel E.P.J., Cambridge University Press, Cambridge, pg. 175.

Völk H.J. & Bernlöhr K., 2009, Experimental Astronomy, 25, 173.

Wachter S. & Smale A.P., 1998, ApJ, 496, L21.

Weekes T.C., Cawley M.F., Fegan D.J., *et al.*, 1989, ApJ, 342, 379.

Westerhout G., 1958, BAN, 14, 488.

White N.E. & Marshall F.E., 1984, ApJ, 281, 354.

White N.E., Parmar A.N., Sztajno M., *et al.*, 1984, ApJ, 283, L9.

Yusef-Zadeh, F., Shure, M., Wardle, M. & Kassim, N. 2000, ApJ, 540, 842.

Zhang I., & Cheng K.S., 1998, A&A, 335, 234.

Zinnecker H., 1982, New York Academy of Sciences Annals, 395, 226.

Ziółkowski J., 2005, MNRAS, 358, 851.